Semiconductor Mode-Locked Laser for High-Speed OTDM Transmission

vorgelegt von
Diplom-Physiker
Marcel Kroh
aus Berlin

von der Fakultät IV - Elektrotechnik und Informatik
der Technischen Universität Berlin
zur Erlangung des akademischen Grades

Doktor der Ingenieurwissenschaften
- Dr.-Ing. -

genehmigte Dissertation

Promotionsausschuss:

Vorsitzender:	Prof. Dr.-Ing. Dr. rer. nat. H. Boche
Berichter:	Prof. Dr.-Ing. K. Petermann
Berichter:	Prof. Dr. rer. nat. H.G. Weber

Tag der wissenschaftlichen Aussprache: 25. Januar 2006

Berlin 2006
D 83

Abstract

The aim of this work is to investigate semiconductor mode-locked lasers for their application as a transmitter pulse source in an optical time division multiplexing (OTDM) system with data rates up to 640 Gbit/s and with on-off keying (OOK) or differential phase shift keying (DPSK) modulation formats. Up to the present work there have not been any applications of the semiconductor mode-locked laser at data rates above 160 Gbit/s and in transmission experiments involving the modulation format DPSK.

The concept of modular pulse generation was implemented comprising the independent building blocks: pulse source, pulse compressor and pulse shaper. This modular pulse generator was able to generate pulse trains with a pulse widths below 0.4 ps and a pulse peak to pulse pedestal contrast exceeding 40 dB. The timing jitter σ_{rms} was lower than 100 fs for an integration interval from 100 Hz to 10 MHz. The generated pulse train was multiplexed up to a 640 Gbit/s single polarization pulse train suitable for OTDM applications. A pulse transmission of compressed pulses over a fiber link of 160 km was demonstrated.

The building blocks of the modular pulse generator can be used independently as a pulse source for a 10 or 40 GHz pulse train, as pulse compressor for the reduction of the pulse width from more than 3 ps to less than 0.5 ps and as a pulse shaper for the removal of a pulse pedestal in order to reach signal to background ratios exceeding 40 dB.

The application of the modular pulse generator was demonstrated in a transmitter of phase modulated data signals. Error free back-to-back measurements were reported for a 320 Gbit/s DSPK bit sequence in a single polarization and a single wavelength channel. An extension to 640 Gbit/s is possible, however only in combination with forward error correction schemes.

Zusammenfassung

Das Ziel dieser Arbeit ist die Untersuchung von modengekoppelten Halbleiterlasern für die Anwendung als Sender Pulsquelle in einem optischen Zeitmultiplex (OTDM) System mit Datenraten von bis zu 640 Gbit/s mit Amplitudenmodulation (OOK) oder differentieller Phasenmodulation (DPSK). Bis zu dieser Arbeit wurden Halbleiterlaser nicht für Datenraten über 160 Gbit/s und in Transmissionsexperimenten mit dem DPSK Modulationsformat eingesetzt.

Mit den Halbleiterlasern wurden Pulsfolgen mit einer Wiederholrate von 10 GHz oder 40 GHz mit geringem Phasen- und Amplitudenrauschen erzeugt. Dabei wurden Halbleiterlaser in externer Kavität und in monolithischer Kavität betrachtet. Verbesserte Rauscheigenschaften der erzeugten Pulsfolgen wurden auf Kosten der Pulsbreite der generierten Pulsfolge erreicht. Ein modulares Konzept bestehend aus den unabhängigen Einheiten Pulserzeugung, Pulsverkürzung und Pulsformung wurde aufgebaut, um eine Pulsquelle zur Erzeugung von Pulsen im Subpikosekundenbereich mit geringerem Phasenrauschen zu erhalten.

Die von dem modularen Pulsgenerator erzeugte Pulsfolge bestand aus Pulsen mit einer Pulsbreite von 0.4 ps und einen Signal-zu-Rausch-Kontrast von mehr als 40 dB. Das Phasenrauschen σ_{rms} konnte in Einseitenbandmessungen [Frequenzbereich 100 Hz, 10 MHz] auf unter 100 fs verringert werden.

Die erzeugte 10 bzw. 40 GHz Pulsfolge wurde zu einer Datenrate von 640 Gbit/s in einer Polarisationsebene und auf einer Wellenlänge gemultiplexed. Eine Verwendbarkeit der generierten Pulsfolge für eine Übertragung auf einer Faserstrecke von 160 km Länge wurde bestätigt.

Die Untereinheiten des modular aufgebauten Pulsgenerators können unabhängig voneinander eingesetzt werden, die Pulsquelle zur Erzeugung von Pulsfolgen mit einer Wiederholrate von 10 bzw. 40 GHz, die Pulskompression zur Verkürzung der Pulsbreite von mehr als 3 ps auf unter 0.5 ps und der Pulsformer zum Entfernen von Pulssockeln bzw. zur Erhöhung des Signal-zu-Rauschkontrasts auf über 40 dB.

Die Phasenstabilität der erzeugten rauscharmen Pulsfolgen blieb bei der Pulskompression und der Erhöhung des Signal-zu-Rauschkontrasts durch nichtlineare Fasereffekte erhalten. Die Verwendbarkeit der modularen Pulserzeugung für einen DPSK Transmitter wurde in einer back-to-back Messung eines 320 Gbit/s DPSK Datensignal nachgewiesen. Die erreichten Fehlerraten in der back-to-back Konfiguration erlauben auch eine Erhöhung der Datenrate auf 640 Gbit/s, sofern Verfahren zur "forward error correction" verwendet werden.

Contents

Chapter 1

Introduction

1.1 Application of optical pulses in Optical Communication Systems

The capacity of fiber optic networks is given by the number of wavelength division multiplexing (WDM) channels times the time division multiplexing (TDM) bit rate per channel. High TDM bit rates are attractive because it was more cost effective in the past to boost the transmission capacity by increasing the channel speed than by increasing the number of WDM channels. This cost efficiency only holds true up to the limit given by the available operation speed of the electrical TDM system, currently 40 Gbit/s. Higher TDM bit rates such as 160 Gbit/s cannot be reached by electrical signal processing at the moment and optical TDM (OTDM) technology is used to overcome this limitation in many laboratories. A recent example of OTDM application is a 3.2 Tbit/s transmission experiment comprising 10 WDM channels with 320 Gbit/s per channel [1]. In this experiment the spectral efficiency reached 0.8 bit/s/Hz.

There are two main reasons to study OTDM-systems. One reason is the investigation of high- speed transmission as a prerequisite for a later introduction of an ETDM- system, e.g. 160 Gbit/s, as soon as electrical signal processing is available at this data rate. The other reason is that all- photonic systems may become the preferred choice in the far future, because these systems offer the highest flexibility and transparency, which is needed for ultra-high capacity data transmission. OTDM-technology is the basis of these all- photonic systems. OTDM systems were successfully demonstrated up to 640 Gbit/s with single polarization [2] or even 1.28 Tbit/s [3] with alternating polarization transmission.

Fig. 1.1 shows schematically a 160 Gbit/s OTDM transmission system. At the transmitter side the essential component is the optical pulse source. The repetition frequency of the generated pulse train depends on the electronic base data rate. OTDM systems typically have a base data rate of 10 Gbit/s or 40 Gbit/s, which is the highest electronic data rate commercially available at present. The optical pulse train is coupled into several optical branches, in which modulators (MOD) are driven by electrical 10 or 40 Gbit/s data signals to generate 10 or 40 Gbit/s optical data signals. The sixteen (or four) optical data

signals are bit-interleaved to generate the multiplexed data rate of 160 Gbit/s. In laboratory experiments, only one modulator is used and combined with the pulse source to a 10/40 Gbit/s transmitter. The 10/40 Gbit/s data signal is then multiplexed by a fiber delay line multiplexer to 160 Gbit/s.

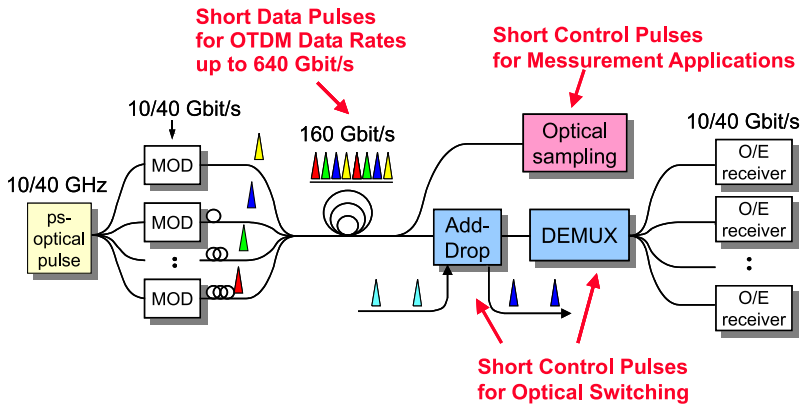

Figure 1.1: Setup of an OTDM transmission system and possible applications of short pulses

Error free 160 Gbit/s transmission over long fiber spans requires compensation for chromatic dispersion and polarization mode dispersion (PMD). Furthermore nonlinearities can disturb the system performance. Therefore measurement techniques like optical sampling help to monitor the pulse quality.

In a simple point-to-point transmission an optical demultiplexer (DEMUX) separates the base data rate channels again for subsequent detection in an O/E receiver and electrical signal processing. In a more advanced OTDM- system all optical Add-Drop nodes allow the fast switching of single base rate data channels.

Several applications of optical pulses are indicated in Fig. 1.1. Additionally to the application as transmitter pulse source, optical pulses can also be applied as control pulses in optical switches, e.g. in add-drop switches, in optical sampling gates and in demultiplexers of OTDM data signals. In this work the focus is on the application of the pulse source in a transmitter.

Optical data signals are generated as non-return to zero (NRZ) or return to zero (RZ) data signals. OTDM system use RZ format evidently. The NRZ data format has the advantage to reduce the optical bandwidth requirements and the bandwidth of the RF circuitry to generate and modulate the data train. On the other hand the RZ data format facilitates a transmission over longer transmission distances [4],[5]. Another parameter is the modulation format, such as amplitude modulation also known as ON-OFF-keying (OOK) and phase modulation, e.g. differential phase shift keying (DPSK). Both can be used with the RZ format.

1.2 Requirements on optical pulses for application as OTDM transmitter

An optical pulse source appropriate for an OTDM transmitter has to satisfy several criteria which can be considered in the temporal domain (Fig. 1.2) or in the frequency domain (Fig. 1.3 on p.5).

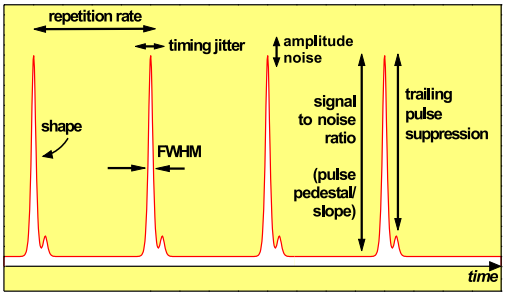

Figure 1.2: Requirements on optical pulses considered within the time regime.

- The optical pulses have a pulse width (FWHM) $\Delta t \leq 0.3\ B^{-1}$ where B is the aggregate bit rate as discussed in [6, 7]. It ensures a sufficient separation of adjacent pulses, necessary to prevent coherent superposition of pulse slopes and the resulting disturbing effects.

- The optical pulses have preferably a sech^2 pulse shape and an optical spectrum with the spectral width (FWHM) $\Delta\nu$ close to the transformation limit, leading to a time-bandwidth product close to the theoretical minimum of $\Delta\nu \cdot \Delta t = 0.3148$. The spectral width (FWHM) is often considered in the wavelength domain with $\Delta\lambda$. The sech^2 pulse shape is especially attractive as the time-bandwidth product is smaller than for Gauss pulses while pulse slopes are steeper than e.g. for Lorentz shaped pulses. Both properties allow pulse applications with higher spectral efficiency. For high pulse peak powers the formation of solitons with sech^2 shape is observed.

- The optical pulse source generates a pulse train with a well-controlled repetition frequency at 10 GHz or 40 GHz and a long term stability to avoid frequency drifts. For instance for a 10 GHz application the exact repetition frequency is defined by the standard transmission module (STM64) to 9.95328 GHz [8]. Forward error correction (FEC) schemes with a data overhead are often introduced to ease the requirements on the tolerable bit error rate from 10^{-9} to 10^{-3}. The required data rate increases by the overhead of about 7 to 11% depending on the exact correction scheme used. Therefore the repetition frequency varies between 9.95328 GHz and 11 GHz or 39.81312 GHz to 44 GHz.

- The pulse train has a high signal to noise ratio (SNR). For the achievement of a maximum transmission length and a maximum data rate a high signal to noise ratio is required for error free detection of "0" and "1" levels in the receiver unit. In the vicinity of the pulses the signal to noise ratio can be overlayed by pulse slopes and by pulse pedestals.

- The pulse train has a sufficient suppression of trailing pulses. It is defined as Trailing Pulse Suppression (TPS), the ratio between the pulse peak power and the trailing pulse power, or in a more general description, the ratio between pulse peak power and the pedestal maximum (Pedestal Suppression). The TPS is in particular important, if the time delay of the trailing pulse is near the bit period 1/B of the aggregate data rate B. A trailing pulse at this temporal position causes a deterioration of the "0" bit level and thus reduces the margins for the decision level for error free detection. Trailing pulses can become a predominant problem compared to the SNR.

- The pulse train has a low timing jitter, at least less than the pulse width or the bit slot (depending on the experimental situation). Especially for the time division multiplexing the exact pulse position in the time slot for each bit is a prerequisite for multiplexing to higher data rates and for error free switching, demultiplexing and detection of received data pulses. For a data transmission at 640 Gbit/s a timing jitter of less than 65 fs is necessary (Sec. A.1).

- The pulse train has a low amplitude noise (AN). Increased AN reduces the receiver sensitivity and limits the system margins.

- The pulse source is tunable in wavelength. Especially the operation within the amplification wavelength band of EDFAs (1530 nm - 1565 nm) is an attractive property.

Another possibility to monitor the quality of a pulse train is the evaluation of the optical spectrum of the pulse train (Fig. 1.3).

The optical spectrum of a pulse train shows a clear 10 GHz or 40 GHz mode comb structure, in the following also called mode-comb spectrum. In the wavelength domain near 1550 nm the mode spacing is equal to 0.08 nm and 0.32 nm for 10 and 40 GHz, respectively. Additional spectral components indicate disturbing frequency components, e.g. due to noise. Fig. 1.3 shows the resolved optical mode comb spectrum of a generated 10 GHz pulse train. The resolution of the spectra was limited by the optical spectrum analyzer to 0.01 nm. For optical pulses of sech^2 shape in temporal regime also an sech^2 shape in the frequency or wavelength regime is expected [9]. For error free operation of transmission systems optical modes with a small line width and a large mode comb height are required (see Fig. 1.3). The underground is composed of disturbing frequencies and white noise. A detailed analysis of the origins of line width broadening in lasers can be found in [10].

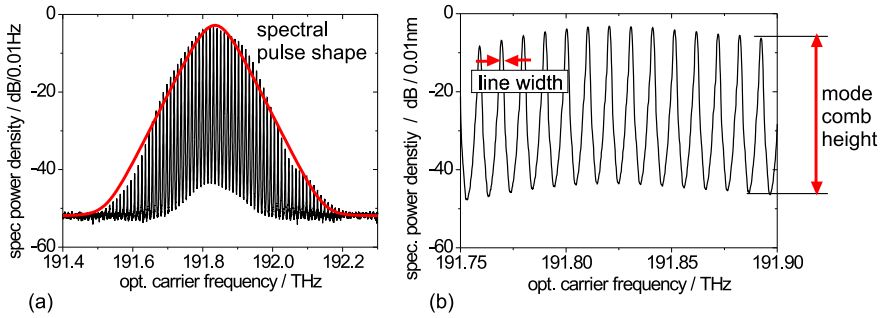

Figure 1.3: The optical mode-comb spectra of a external cavity mode-locked laser operating at its fundamental frequency of 10 GHz. (a) the spectrum with the red line representing the fit of a sech^2 envelope, (b) part of the spectrum showing the mode comb height and the line width measured with a resolution bandwidth of 1.25 GHz (0.01 nm). The carrier frequency $\nu = 191.85$ THz corresponds to a wavelength of $\lambda = 1562.87$ nm.

1.3 Objectives and Content of this work

The aim of this work is to investigate semiconductor mode-locked lasers for their application as a transmitter pulse source in an OTDM-system with data rates up to 640 Gbit/s and with OOK or DPSK modulation format. Up to the present work [11], there have not been any applications of the semiconductor mode-locked laser at data rates above 160 Gbit/s and in transmission experiments involving the modulation format DPSK.

The pulse generation with semiconductor lasers shows a trade-off between temporal width and low phase noise. This trade-off limits the pulse generation with semiconductor mode-locked lasers to an OTDM-data rate of 160 Gbit/s, if no additional measures are implemented. An approach to circumvent this limitation is a modular pulse generation, separated into the independent building blocks: pulse source, pulse compressor and pulse shaper. In the pulse source the focus is set on pulse generation with a low phase noise. Thereafter, an external fiber based pulse compressor and a pulse shaper (2R-regenerator) are used to bring the pulse width and the pulse shape (pedestal suppression) to the required values. The condition for these external building blocks are the conservation of the low noise characteristics of the optimized pulse source and the conservation of the phase coherence for applications in DPSK transmission systems.

Following the review of the pulse requirements in this chapter, chapter 2 discusses the most important measurement methods, which are used in the frame of this work. Chapter 3 reviews the prerequisites for a short pulse generation and compares some important pulse sources, which are contemporarily used in laboratories for pulse train generation. The advantages and the disadvantages of each method are highlighted in order to give an overview for the appropriate choice of the pulse source and to motivate the continued research on the vari-

ous concepts. The set-up of semiconductor lasers is discussed in more detail in Chapter 4. Different layouts of semiconductor mode-locked laser diodes were investigated in the frame of this work. In chapter 5 the basic properties of external cavity mode-locked laser (EC-MLL) and monolithic mode-locked laser (M-MLL) are described and compared. The possibilities to operate the semiconductor laser sources with a low timing jitter is considered in the section 5.4. It turns out, that the predominant need of a low phase noise pulse generation cannot be reached simultaneously with a short pulse generation. This trade-off leads to the stepwise pulse generation with low noise and subsequent implementation of a pulse compression and a pedestal removal. For the pulse compression the fiber based methods of soliton formation and supercontinuum generation are investigated in detail. In chapter 6 the pulse compression is evaluated with respect to the pulse requirements needed. The investigations include the possibility to ease the power requirements for a pulse compression at the future base rate of 40 GHz. At the end of this chapter the limitations of the fiber based pulse compression are considered. The pulse compression is often accompanied with a loss in the pulse to pedestal contrast. Therefore possibilities of pulse contrast improvements by the application of a loop mirror or with wavelength conversion are considered in chapter 7.

Chapter 8 describes the application of the generated pulse trains by means of selected examples. Semiconductor pulse sources were used to generate 10 and 40 GHz pulse trains with a phase noise performance comparable to commercially available pulse sources such as fiber ring laser and solid state mode-locked laser. The pulse generation is combined with a pulse shaping, comprising the pulse compression and a pulse pedestal reduction, and can be used to generate pulse trains of 400 fs pulses with a pulse to pedestal contrast exceeding 40 dB. The maintenance of the phase stability during pulse compression and pulse shaping is demonstrated using a solid state mode-locked laser in a 640 Gbit/s back-to-back measurement. Semiconductor EC MLL are used in error free back-to-back measurements for repetition frequencies of up to 320 Gbit/s using the differential phase shift keying modulation format. In combination with forward error correction (FEC) a further doubling of the data rate to 640 Gbit/s is possible, although the limitation of this laser type becomes perceptible.

Chapter 2

Pulse Characterization

In this chapter the pulse characterization is considered. The measurements of the temporal pulse width (FWHM) Δt, the spectral width of the pulse (FWHM) $\Delta\nu$, the pulse repetition frequency f_{rep} and the noise of a pulse train, namely the amplitude noise and the phase noise are considered. An overview over the properties of the measurement devices as used in the frame of this work is given in Tab. 2.1.

Device	Measured Parameter	Operation Range	Sensitivity P_{avg}, E_{pulse}	Resolution
AC	Δt_{ac}	1.1-1.6 μm	$< 10^{-6}$ W^2 ($P_{avg} \cdot P_{peak}$)	0.01 ps
FROG	Δt_{ac}, λ	1.3-1.6 μm 0-40 GHz	<0.5 pJ/pulse	0.05 nm 0.02 ps
OSA	λ	0.6-1.7 μm	-87 dBm	0.01 nm
ESA	f_{rep}	1 Hz-40 GHz	-140 dBm	1 Hz

Table 2.1: AC: autocorrelator [12], FROG: frequency resolved optical gating [13], OSA / ESA: optical / electrical spectrum analyzer [14, 15]. P_{avg}: Average power of a pulse train, Δt_{ac}: convoluted temporal pulse width.

The measurement of the pulse characteristics often reaches the limit of the measurement devices and evaluation of the measurement set-up rather than the properties of the measured signal has to be avoided. In the following, the measurement methods and their limitations are discussed with focus on the pulse characterization made later in this work.

2.1 Pulse width measurements

An optical pulse with a pulse width of $\Delta t = 1$ ps requires a detector bandwidth of several 100 GHz for exact recovery of the pulse shape. A low detector

bandwidth leads to the detection of a broadened pulse envelope restricting the resolution of the detector. For pulse width measurements, devices are available such as electrical sampling oscilloscopes, streak cameras, optical sampling oscilloscopes and autocorrelators.

The bandwidth of fast sampling oscilloscopes is limited due to the required conversion from optical to electrical signals. Highest commercially available bandwidths of photodiodes at 1.5 μm are currently specified to 50 GHz [16]. Optical pulses of a width (FWHM) of 1 ps, measured with such photodiodes and an electrical sampling oscilloscope show a trace with a pulse width of $\leq$ 10 ps. Another problem arises from the accuracy of the time axis. Typical values for time variations are slightly below a root mean square (rms) standard deviation of $\sigma_{RMS} = 180\ fs$. It limits the resolution of the exact pulse position.

The temporal resolution of streak cameras is limited to 200 fs. Therefore a measurement of a 1 ps pulse would deliver only 5 measurement points. For shorter pulses, e.g. 400 fs pulses for 640 Gbit/s OTDM applications, the situation would be even worse.

An alternative to the bandwidth limitation of photo detectors is the application of the pulse sampling based on an optical sampling system. The technique is discussed in detail elsewhere [17]. Optical sampling measurement systems have reached a bandwidth of several 100 GHz and were used to monitor 640 Gbit/s OTDM pulse trains [18]. For this work an optical sampling set-up based on a Kerr Gate [19] with a bandwidth of about 400 GHz was available and the measurement of pulse trains with a repetition frequency of up to 320 Gbit/s was possible as shown in Fig. 8.2. The measured curves were displayed on a sampling oscilloscope with the limitation in the exact timing position as mentioned before.

Another possibility to measure the pulse width is the commonly used intensity autocorrelation.

2.1.1 Autocorrelation measurements

The idea of autocorrelation measurements is the measurement of a short pulse by itself. A commonly used autocorrelation set-up is based on a Michelson interferometric layout as depicted in Fig. 2.1. In cross-correlation set-ups one interferometer arm is replaced by a second entrance to allow the measurement of light pulses of different origin. For cross- correlation measurements see Sec. 2.3.2.

In the autocorrelator the pulse train and a delayed replica of the pulse train coincide in a nonlinear crystal for second harmonic generation (SHG). For efficient second harmonic generation the propagation of incoming signal and the generated second harmonic signal have to be phase matched in the nonlinear crystal [20]. For the measurement one of the retro reflectors is moved on a shaker with a frequency of several Hz. The measurement result will be the autocorrelations function $G(\tau)$

$$G(\tau) = \frac{\int I(t) \cdot I(t-\tau)dt}{|\int I^2 dt|} \tag{2.1}$$

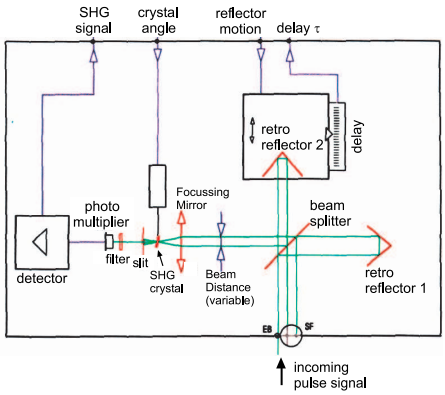

Figure 2.1: Set-up for an autocorrelation measurement [12].

with I the pulse intensity, t the time and τ the relative time delay of both pulses to each other.

G(τ) contains no information of the temporal orientation of leading and trailing edge of the pulse nor about trailing or previous pulse pedestals. The auto-correlation is independent of timing jitter because of the simultaneous influence on both pulse replicas in case of an autocorrelation. The measurement does not contain any phase information.

In order to obtain a phase matching between the incoming light and the SHG light the nonlinear crystal has to be turned into an angular position, in which both light waves propagate with the same velocity. The required crystal orientation depends on the wavelength. For broad spectra of some 10 nm, i.e. in connection with short pulses, the optimization or the angular position is limited.

A background free measurement is performed by the separation of the second harmonic from both light beam replicas by spatial filtering. Only the new generated second harmonic signal passes the slit introduced in the light path. A sufficient SHG intensity is required to avoid disturbing measurement floors by a high photo multiplier amplification or by the photo detector noise floor. Therefore the measurement of optical pulse signals, e.g. semiconductor laser pulses, is in most cases combined with a previous amplification by an EDFA. The installed preamplifiers allow a linear or logarithmic amplification.

For the measurement of the pulse width a linear amplification is useful, while a measurement of the pulse contrast is obtained with more dynamic range using the logarithmic preamplifier. The interferometer set-up used for most measurements in the frame of this work had two independent entrances for cross correlation. Therefor the retro reflector 1 in Fig. 2.1 was replaced by a second pulse signal entrance. In order to perform an autocorrelation measurement both inputs were connected with an equal length of fiber by a 50:50 coupler.

Due to the convolution of the measured pulse with itself, the measured autocorrelation traces are always symmetric. For the evaluation of the differences between the rising and falling slope cross correlation measurements can be used.

Pulse shape	Intensity I($\tilde{t}$)	G($\tilde{\tau}$)	$\triangle$t/$\triangle$t$_{ac}$	K=$\triangle\nu\triangle$t
Gauss	$e^{-\tilde{t}^2}$	$e^{(\frac{-\tilde{\tau}^2}{2})}$	0.7071	0.4413
Sech	$sech^2(\tilde{t})$	$3\frac{\tilde{\tau}\coth(\tilde{\tau})-1}{\sinh^2(\tilde{\tau})}$	0.6482	0.3148
Lorentz	$\frac{1}{1+\tilde{t}^2}$	$\frac{1}{1+(\frac{\tilde{\tau}}{2})^2}$	0.5000	0.2206
Symmetric Exp	$e^{-2\lvert\tilde{t}\rvert}$	$(1+2\tilde{\tau})e^{(-2\lvert\tilde{\tau}\rvert)}$	0.4130	0.1420

Table 2.2: Pulse shape functions for autocorrelation measurements [21]
I($\tilde{t}$): Intensity profile, G($\tilde{\tau}$): corresponding autocorrelation function. The parameters $\tilde{t} = \frac{t}{T_0}$ and $\tilde{\tau} = \frac{\tau}{T_0}$ are normalized times, where T_0 is a time characteristic for the width of the pulses. $\triangle$t: temporal FWHM of the pulse; $\triangle$t$_{ac}$: FWHM of the autocorrelation signal, K = $\triangle\nu\triangle$t: time-bandwidth-product, $\triangle\nu$: spectral FWHM of the pulse.

The FWHM of the pulse can be concluded from G(τ) [21] by comparison with the autocorrelation traces of known input pulse shapes. Common functions for approximation and deconvolution of measured pulse shapes are shown in Tab. 2.2.

2.1.2 FROG measurements

An introduction to frequency resolved optical gating (FROG-) measurements is given in [22]. The FROG measurement set-up used here is based on the intensity SHG autocorrelation measurement, extended by a detection of the optical spectra for each time delay (Fig. 2.2).

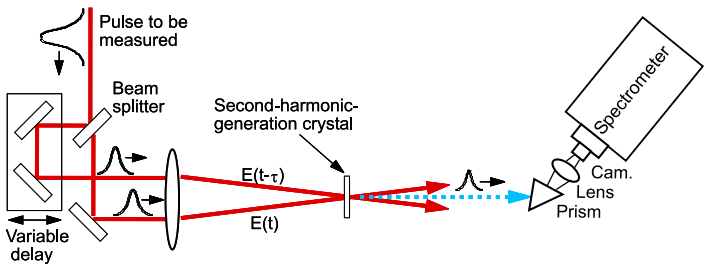

Figure 2.2: Set-up of a SHG Frequency Resolved Optical Gating (FROG) device [22].

A typical FROG spectrogram is shown with a color grading for the intensity either with linear color grading or logarithmic color grading, which better resolves evanescent pulse slopes. Fig. 2.3 shows the result of a FROG measurement of a pulse train generated by an external cavity mode-locked laser (EC-MLL). A retrieve algorithm generates theoretically a two dimensional spectrogram using assumptions for the parameters pulse phase and intensity for both, the frequency domain and the time domain. The calculated spectrogram is

compared with the measured FROG spectrogram and an approximation for a minimum deviation is made. The exact shape of the pulse intensity, temporal and spectral phase, chirp and wavelength dependent group delay over the pulse can be deduced from this approximation. Details of the measurement procedure are described in [22] and [23].

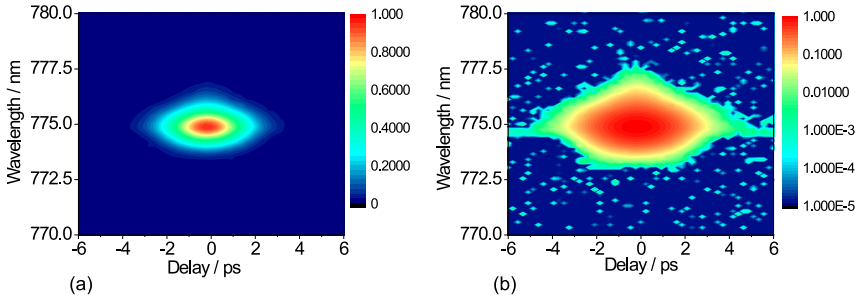

Figure 2.3: Example of a two dimensional spectrogram of a FROG measurement of pulses generated by external cavity mode-locked laser (EC-MLL) with linear (a) and logarithmic (b) colorgrading. Note: Here the second harmonic of the laser wavelength of 1550 nm is measured.

A good agreement of the calculated spectrogram and the measured FROG trace is reached with an appropriate set of start parameters. The consistency of the derived pulse shape and spectra with separate measurements by an optical spectrum analyzer and an autocorrelator confirm a retrieved FROG measurement.

Due to the symmetry of the SHG FROG measurement no temporal orientation can simply be given for the autocorrelation and the derived phase and chirp curve. At least one more measurement with a pulse having a known change of the chirp is necessary, e.g. by insertion of a certain length of SSMF. The calculation of the chirp value is relative to an arbitrary chosen reference frequency ω_0, usually the intensity maximum of the frequency domain.

The chirp C(τ) is calculated by

$$C(\tau) \quad = \quad \frac{-\frac{d\phi(\tau)}{d\tau}}{2\pi} \tag{2.2}$$

In the wavelength domain the spectral intensity $P(\lambda)$ and the spectral phase $\varphi = \varphi(\lambda)$ is retrieved from the FROG graph. A further information is given about the relative time delay $t_{group}(\omega)$, at which the different wavelength components of the measured pulse arrive in the FROG measurement device. As complement to the chirp C(τ) in the time domain, there is a corresponding quantity $\frac{d\varphi}{d\omega}$ in the frequency domain, which is called group delay t_{group} [22]

$$t_{group}(\omega) = \frac{d\varphi}{d\omega} \Leftrightarrow t_{group}(\lambda) = \frac{d\varphi}{d\lambda} \cdot \frac{-\lambda^2}{2\pi \cdot c} \ . \tag{2.3}$$

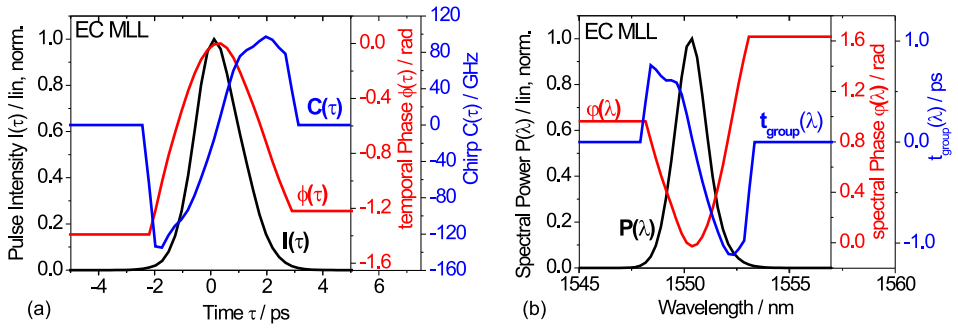

Figure 2.4: Extracted data from the FROG spectrogram shown in Fig. 2.3 in time and frequency/wavelength domain using the retrieval algorithm. In the time domain (a) the pulse intensity I(τ), the temporal phase $\phi(\tau)$ and the chirp C(τ) is determined. In the frequency or wavelength domain (b) the spectral power P(λ), the spectral phase $\varphi(\lambda)$ and the difference in the group delay $t_{group}(\lambda)$ is shown.

Pulse intensity I(τ) and spectral power P(λ) are shown in Fig. 2.4 on a normalized scale. The temporal phase $\phi(\tau)$, the chirp C(τ), the spectral phase $\varphi(\lambda)$ and the group delay $t_{group}(\lambda)$ are relative quantities. The zero reference is usually placed at the maxima of the pulse intensity and spectral power, respectively.

2.2 Measurement of the frequency spectrum

Optical pulse sources used for OTDM applications have a repetition frequency of typically 10 or 40 GHz. The carrier frequency of the pulses on the other hand is about 193.5 THz, which corresponds to a wavelength of 1550 nm. A 1.0 ps pulse covers around 200 oscillations of the E-field within its FWHM width. For measurements of the optical carrier frequency or the pulse repetition frequency an optical or an electrical spectrum analyzer are used, respectively.

Measurement with optical spectrum analyzer

The optical spectrum analyzer provides information about the frequency mode spectrum of the generated pulse trains as shown in the example in Fig. 1.3. In the frame of this work spectrum analyzers with a minimum resolution of 0.01 nm (1.25 GHz) were available. To date, the best resolution of < 0.24 pm (< 30 MHz) is provided by an optical spectrum analyzer of the company APEX [24]. In difference to grating based spectrum analyzers here an interferometric method is used. It could be used e.g. for an exact evaluation of spectral components of sub-harmonic components and the noise floor. For a 10 GHz signal the optical mode spacing is 0.08 nm, a spectral width of 1.0 nm contains 12 modes.

Measurement with electrical spectrum analyzer

The pulse train repetition frequency is measured by an electrical spectrum analyzer (ESA). The optical signal needs to be converted into an RF signal by a photodiode. The principal set-up of the measurement is shown in Fig. 2.5 (a). The incoming RF signal is multiplied with the sweep signal of a reference oscillator. At the mixer output a lower intermediate frequency is generated (frequency conversion) for further evaluation. The measurement accuracy is limited by the internal reference oscillators (cf. Fig. 2.7).

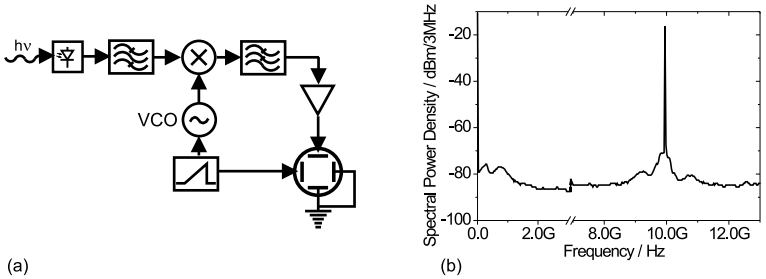

Figure 2.5: (a) Measurement principle of an eletrical spectrum analyzer [25], (b) typical frequency spectrum of a 10 GHz pulse source.

The information obtained from this spectrum is the position and power of the repetition frequency. Furthermore the distribution of noise components around the carrier, which are composed from amplitude noise and phase noise can be measured.

At the zero frequency the 1/f noise of the measurement device becomes apparent. Amplitude noise (low frequency components) can be found in a frequency range of some 10-100 MHz and around the carrier frequency of 10 GHz due to frequency mixing as displayed in Fig. 2.5 (b).

2.3 Noise measurements

Noise is composed of amplitude noise and phase noise (Fig. 2.6). The variation of a pulse peak level from the average value is considered as amplitude noise (AN). The variation of the temporal pulse position from its predetermined position in the bit slot is caused by phase noise (PN).

The total noise is composed of random fluctuations and deterministic noise. Random fluctuations are caused by the quantum nature of the emission and by spontaneous amplification processes. Deterministic fluctuations can have different origins such as an improper looking of harmonic modes in laser sources: e.g. every second pulse is higher (or lower) than its successor. Q switching and pulsation of pulse sources are further examples. Pattern effects due to the saturation of active elements for amplification or absorption of data words

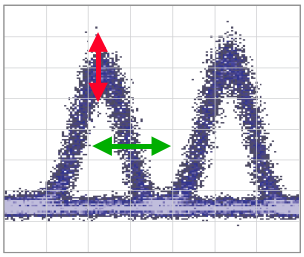

Figure 2.6: Amplitude noise (red arrow) and phase noise (green arrow) indicated in a measured data pulse eye. The width of pulse traces is partly broadened due to the finite stability of the time reference (x-axis).

using the on-off-keying (OOK) modulation format can cause contributions to systematic noise too. This problem increases with the data word length used.

Another problem is the conversion of amplitude noise into phase noise and vice versa, which can occur already during the pulse generation or in a subsequent pulse shaping and pulse transmission. This conversion is especially observed for semiconductor materials due to the strong relation between refractive index and amplification, described by the line width enhancement factor, also known as α-factor. As soon as fiber nonlinearities are used for optical pulse manipulation and transmission this conversion becomes also apparent in fiber links. A well-known example is the Gordon- Haus- Jitter [26].

The frequency resolved contributions of phase noise are of different importance for transmission systems. Low and mid-range frequency components up to ~ 1 MHz can be tolerated by application of feedback loops and clock recovery set-ups. Higher phase noise frequencies are more critical for error free operation of OTDM systems because clock recovery circuits do not have the bandwidth to generate synchronized reference signals. A fast realignment of control pulses or switching windows for demultiplexer and receiver units becomes difficult.

2.3.1 Amplitude noise measurement

The amplitude noise can be measured with a sampling oscilloscope and a value for the amplitude noise (AN) is derived from

$$AN = \frac{\sigma_{RMS}(V_{amplitude})}{V_{amplitude}} \tag{2.4}$$

with $\sigma_{RMS}(V_{amplitude})$ being the standard deviation of the maximum photo detector voltage, which is measured in the pulse peak (cf. Fig. 2.6) and with $V_{amplitude}$ being the average amplitude of the photo detector voltage [27]. This method is used in the frame of the following work.

An alternative, not used in the frame of this work, is the evaluation of the RF frequency spectrum of the pulse train in the frequency range from 0 Hz to $f_{rep}/2$.

2.3.2 Phase noise measurement

The discussion of methods for phase noise measurements is subject of a wide number of publications [27, 28, 29, 30, 31]. In the frame of this work only some methods are used and detailed considerations are made hereafter.

Sampling oscilloscope measurement

The most simple method to measure the phase noise of a pulse train is to use a sampling oscilloscope. The pulse trace is measured multiple times and the standard distribution of the temporal pulse slope position is evaluated. Such a phase noise measurement has a limited accuracy due to the phase noise contribution of the time base of the electrical sampling oscilloscope. Typically pulse-to-clock (pc) timing jitter values reach values of $\sigma_{RMS\ PC} \approx 180\ fs$. The noise evaluation of a pulse train with a timing jitter below or around this value is impossible or yields results with an increased measurement uncertainty. The duration of the measurement, i.e. the number of evaluated traces, influences the measured timing jitter values. Another drawback is the lack of information about the frequency distribution of the phase noise.
The same limitations are apparent for optical sampling measurements, which use the sampling oscilloscope as final monitoring unit.

Single Side Band (SSB) phase noise measurement

Another method often used to estimate the timing jitter is the measurement of the single sideband (SSB) phase noise with an electrical spectrum analyzer (see Fig. 2.7 (a)). This measurement provides also information about the frequency distribution of the phase noise.

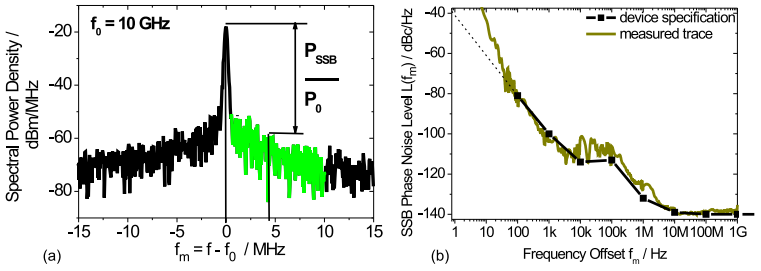

Figure 2.7: (a) Single Side Band (SSB) phase noise evaluation (in principle), (b) comparison of lowest measured phase noise curves with the specifications of the electrical spectrum analyzer [32].

The SSB phase noise level L(f_m) is the ratio of the power P_{SSB} at the frequency offset (f_m) to the power P_0 at the carrier frequency f_0. L(f_m) is

related to 1 Hz bandwidth

$$L(f_m) = \frac{P_{SSB}(f_m)|_{1Hz}}{P_0} \tag{2.5}$$

The SSB phase noise level L(f_m) can be measured around the carrier frequency f_0 or around the n^{th} harmonic n·f_0 of the carrier frequency of a pulse signal with $f_m = f - n \cdot f_0$. From the phase noise level L(f_m) of the n^{th} harmonic, L(f_m)$_n$, the rms timing jitter σ_{rms} can be calculated according to [33]

$$\sigma_{rms} = \frac{1}{2\pi n f_0} \sqrt{2 \int_{n \cdot f_0}^{(n+\frac{1}{2}) \cdot f_0} L(f_m)_n \; df_m}. \tag{2.6}$$

The measurement accuracy of the SSB phase noise level L(f_m) is limited by the intrinsic phase noise of the electrical spectrum analyzer (ESA) used. The manufacturer of the ESA provides device specifications for L(f_m) values (black dots in Fig. 2.7 (b)) which represent the minimum noise level to be measured by the device. The measured line in Fig. 2.7 (b) depicts results of a SSB measurement using the RF synthesizer which is used as RF source for the mode-locked lasers considered in this work.

As mentioned before, the total noise spectrum is composed of amplitude noise and phase noise. Amplitude noise (low frequency components) can be found around the carrier due to frequency mixing as displayed in Fig. 2.5 (a). It is possible to estimate the contribution of amplitude noise by performing measurements of L(f_m) at higher harmonics n. If the single side band measurement reveals pure phase noise the timing jitter σ_{rms} is independent of the measured harmonic n of the periodic signal. According to eqn. (2.6) $L(f_m)_n$ has therefore to be proportional to the order of the evaluated harmonic n^2. Based on the calculation with eqn. (2.6) for higher harmonics a characteristic increase in the phase noise level has to be observed leading to an difference of the phase noise level of $\Delta_{(n)} = L(f_m)_{n \neq 1} - L(f_m)_{n = 1}$ with $\Delta_{(n=2)} = 6\ dB, \Delta_{(n=3)} = 9.5\ dB, \Delta_{(n=4)} = 12\ dB$.

Fig. 2.8 shows the SSB phase noise curves of the fundamental repetition frequency and its higher harmonics for an EC-MLL operated at $f_{rep} = 5.5\ GHz$. The timing jitter calculated with eqn. (2.6) varied between $\sigma_{rms} = 350$ fs and 380 fs for the 7 harmonics measured.

As described in [27] the phase noise level L(f_m)$_n$ is expected to increase proportional to n^2. On the other hand a noise level L(f_m)$_n$ independent on n indicates the presence of amplitude noise. Fig. 2.8 shows that L(f_m)$_n$ for this laser represents mainly phase noise up to the frequency offset of 10 MHz. For frequency offsets higher than 10 MHz L(f_m)$_n$ is about constant which indicates the presence of amplitude noise. Near a frequency offset of 1 GHz, the noise floor of the electrical spectrum analyzer limits the measurements for harmonics with frequencies > 26 GHz. Therefore the harmonics with N = 5 and n = 6 show an increased noise level for high frequency offsets of 1 GHz.

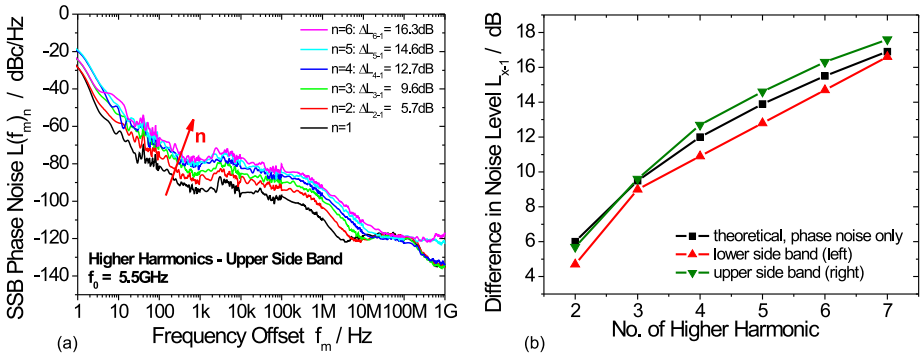

Figure 2.8: (a) SSB Noise curves of higher harmonics and (b) difference of the phase noise levels $L(f_m)_n - L(f_m)_{n=1}$ (averaged over frequency offsets f_m in [100 Hz - 10 MHz]) between n^{th} and 1^{st} harmonic.

For the calculation of the timing jitter according to eqn. 2.6, the SSB phase noise level $L(f_m)_{n=1}$ has to be integrated over the frequency offset interval, ideally from the carrier frequency f_0 up to the Nyquist frequency $f_0+f_0/2$ [30]. For a 10 GHz pulse train this interval starts from $f_m = 0$ up to 5 GHz. In most cases this is technically not possible. The ITU standard [34, 35] recommends an evaluation between 20 kHz and 80 MHz for a 10 GHz pulse train. However, this recommendation does not consider the experimental situation in many cases and has not found a consequent use in the literature yet. In the present work, the integration range from $f_m = 100$ Hz to 10 MHz is used. Measurements below 100 Hz are falsified by the carrier signal itself due to the resolution bandwidth and the stability of the internal frequency reference of the measurement device (cf. Fig. 2.7 (b)). On the other hand the upper limit of 10 MHz is used in order to exclude the eventual appearance of the amplitude noise components as described above, but also by the noise floor of the spectrum analyzer (cf. Fig 3.2 (b)).

The jitter values obtained in this work are used to compare various pulse sources. The deviation of these jitter values from the exact values can only be estimated. Two estimates were performed. Using the cross correlation measurements described below it is estimated that the neglect of frequencies > 10 MHz in the integration range causes an error of less than 30 %. On the other hand the error due to the neglect of the frequencies below 100 Hz is estimated using an electrical sampling oscilloscope (see section 5.1). The experiments show, that the estimated timing jitter for frequencies below 100 Hz is less than the timing jitter of the oscilloscope, which is 180 fs.

Cross correlation measurements

The cross correlation measurement method allows a timing jitter evaluation in the time domain. The measurement follows the method described in [36]. As an example autocorrelation measurements were made for a pulse train leaving a semiconductor mode-locked laser operated with the repetition frequency of 5.5 GHz. This measurement was done for passive and hybrid mode-locking.

The pulse train is split by a 3 dB coupler into a short fiber branch (length 0) and a long fiber branch of length l. First, the pulse width Δt is measured by an autocorrelator at the output of the short fiber branch ($\Delta t_{AC}(0)$) and at the output of the long fiber branch ($\Delta t_{AC}(l)$). It is used to determine the pulse broadening due to the fiber dispersion. Second, the pulse width $\Delta t_{XC}(l)$ is measured by a cross-correlation measurement using the output of the short and long fiber branch.

Here the measured pulse broadening is a combination of dispersion of one pulse train in the long fiber branch and the timing jitter between both pulse trains with on pulse train delayed with respect to the other.

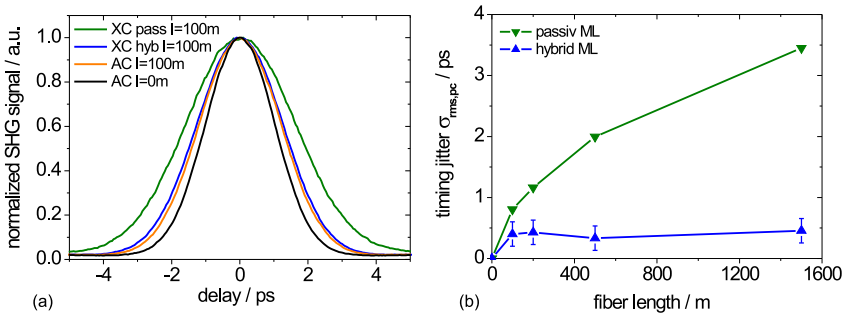

Figure 2.9: (a) measurement of pulse widths in cross-correlation (XC) and autocorrelation (AC). (b) growth of calculated timing jitter values in dependence of the pulse distance in cross correlation measurement for the both cases of passive and hybrid mode-locking.

According to [36] the pulse-to-pulse timing jitter $\sigma_{rms,pp}$ can be calculated now from the measured pulse width in consideration of the dispersion effect by

$$\sigma^2_{rms,pp} = \frac{1}{2.3548}[\Delta t_{XC}(l)^2 - \frac{\Delta t_{AC}(0)^2 + \Delta t_{AC}(l)^2}{2}] \tag{2.7}$$

were a gaussian shaped pulse was assumed. The relation between peak-to-clock and peak-to-peak rms timing jitter is $\sigma_{rms,pc} = \sigma_{rms,pp}/\sqrt{2}$.

The formula 2.7 is strictly valid only for a gauss pulse [36]. $\sigma_{rms,pp}$ depends on the length of the fiber delay between the two cross correlated signals. Especially in the case of passive mode-locking no force keeps the pulses in their bit slots which results in an increasing pulse to pulse mismatch. Fig. 2.9 (a) shows examples of measured correlation traces for a given length l. Fig. 2.9 (b) shows

results of timing jitter $\sigma_{rms,pc}$ evaluation for passive and hybrid mode locking of a semiconductor EC-MLL.

It is possible to identify the phase noise contribution of high frequency components with the pulse broadening in cross correlation measurements at fiber delay lengths of about 100 m. In case of hybrid mode-locking, a further increase of the delay length (> 100 m) between both cross correlated pulse trains caused minor deviations in the calculated timing jitter. Assuming a refractive index of n = 1.45, the time for pulse propagation through a fiber of the length of 100 m is about 484 ns, which is equal to a cross correlation between the 1^{st} and the 4840^{th} pulse of a 10 GHz pulse train or between the 1^{st} and the 2662^{th} pulse of a 5.5 GHz pulse train as used in Fig. 2.9. Cross correlation measurements with a delay of 484 ns evaluate the frequency components with $f_{noise} \geq$ 2.0 MHz. For hybrid mode-locking an almost constant timing jitter of about 0.4 ps is already reached within the error bars for a delay length of 100 m. In case of passive mode locking, there is a continued accumulation of phase deviations between distant pulses. Here, the timing jitter is caused by the missing synchronization reference.

Following [36] the cross-correlation measurements can be used to give an estimate for the SSB-noise measurements. A cross-correlation with a delay time T contains all timing fluctuations faster than 1/T. The delay T is related to the fiber length by $T = L/\frac{c}{n}$. Therefore, a delay length of L = 100 m contains all timing fluctuations faster than 2 MHz, and a delay of L = 1500 m contains all timing fluctuations faster than 140 kHz. The results in Fig. 2.9 (b) show that the jitter for the hybrid mode-locked laser is about 0.4 ps for all timing fluctuations faster than 2 MHz and faster than 140 kHz. Within the error bars these results are in agreement with the SSB-phase noise measurements in the same frequency range. An estimation on the error made by the limited integration interval of the SSB phase noise measurements is made as follows. The integration of a SSB phase noise curve in Fig. 2.8 yields a jitter value of $\sigma_{SSB,2}$ = 350 fs in the integration range of 100 Hz to 10 MHz and $\sigma_{SSB,1} = 230\ fs$ in the integration range between 100 Hz and 140 kHz. The jitter value $\sigma_{SSB,\infty}$ in the integration range from 100 Hz to all higher frequencies is estimated by $\sigma^2_{SSB,\infty} = \sigma^2_{SSB,1} + \sigma^2_{rms,pc}$. With $\sigma_{rms,pc}$ = 400 fs a jitter of $\sigma_{SSB,\infty}$ = 460 fs is obtained. It means, that the neglect of the integration range above 10 MHz caused an error of about 30 %, which is an estimation for the maximum error caused by the neglect of this frequency range.

Chapter 3

Pulse Sources for OTDM-systems

The most important optical pulse sources for OTDM systems and their properties are summarized in Tab. 3.1. The external cavity mode-locked laser (EC-MLL) and the monolithic mode-locked laser (M-MLL) are investigated in this work and will be described in detail in chapters 4 and 5. For comparison, pulse generation by a solid state mode-locked laser, by an erbium doped fiber ring laser (EFRL) and by cw light modulation with an electro absorptions modulators (EAM) are discussed in this chapter.

Source	pulse width	tuning		Pout
		wavelength	f_{rep}	
EC-MLL	1 - 3.5 ps	C-Band	1 - 20 GHz	$\leq$ 1 mW
M-MLL	1.6 - 5.0 ps	$\pm$ 2.5 nm	40$\pm$0.5 GHz	$\sim$ 1 mW
Solid State MLL	1.6 - 2.1 ps	non	10$\pm$0.01 GHz	10 mW
EFRL	1.0 - 3.0 ps	C-Band	40$\pm$1.0 GHz	10 mW
EAM	$>$ 3 ps	C-Band	$\leq$ 40 GHz	$\leq$ 0.25 mW

Table 3.1: Comparison of pulse sources used for optical signal generation and processing. All pulse sources cover the C-Band from 1530 nm to 1565 nm and their assembly can be optimized for a specific wavelength and repetition frequency. Once both parameters are chosen, their tunability vary from source to source. The values listed here are according to the measurements carried out for a pulse source comparison.

3.1 Constructive Interference of Optical Modes

The laser operation is limited to a frequency region, where the laser threshold condition is satisfied. The width of the spectral frequency band $\Delta\nu$ covers typically several longitudinal resonator modes N. The spectral mode structure of the emitted light is determined - among other parameters - by the length L

of the laser resonator and the group velocity v_{gr}. The optical resonator modes oscillate at different frequencies with a frequency spacing $\Delta\nu_0 = \frac{v_{gr}}{2 \cdot L}$ between neighboring modes.

The electrical field is given by

$$E(t) = \sum_{n=1}^{N} E_n exp\{2\pi j[(\nu_0 + n \cdot \Delta\nu_0)t] + \phi_n\} \tag{3.1}$$

with E_n the amplitude of the mode n, ϕ_n the phase of the n^{th}-mode and t the actual time. If the phases of the optical modes are statistically distributed and the amplitudes of all modes are equal to E_0, cw light emission with a power of $P = N \cdot E_0^2$ is expected.

For the formation of a periodic optical signal a constructive interference of optical modes is necessary. Therefore ϕ_n has to become equal for all modes after each time interval given by the oscillation period in the resonator. For a mode-locked laser the output power is a periodic function. The maximum power P of a generated pulse train reaches $P = N^2 \cdot E_0^2$, while the average power remains almost the same as for cw light emission [37]. The time-bandwidth product K=$\triangle\nu\triangle$t limits the minimum pulse width in the spectral and temporal domain and depends on the particular shape of a pulse. A selection of K values for the most common pulse shapes is given in Tab. 2.2. The number of oscillating modes N and the pulse width Δt are given by

$$N \approx \Delta\nu \frac{2L}{v_{gr}} = \frac{\Delta\nu}{\Delta\nu_0} \tag{3.2}$$

$$\Delta t \geq \frac{K}{N} \frac{2L}{v_{gr}} = \frac{K}{\Delta\nu} \tag{3.3}$$

With K = 0.3148 for the time-bandwidth product of transformation limited $sech^2$ pulses, it is possible to derive an estimation on the number of modes necessary for a particular pulse width. In case of 400 fs pulses with a repetition frequency of 10 GHz the coupling of N $\sim$ 100 optical modes is necessary. For a repetition frequency of 40 GHz only 25 modes are necessary. Despite the wider mode spacing the required spectral bandwidth remains unchanged. In consequence, the determining parameter is the spectral width of the wavelength region that complies the lasing threshold condition.

3.2 Mode-locked Laser

Constructive interference of several longitudinal optical modes is obtained by a saturable absorber in the laser resonator, which is saturated only by high optical powers. Constructive interference of several optical modes is necessary for a sufficient saturation of the absorber. Optical modes oscillating with a different phase will reach the unsaturated absorber and experience an attenuation. Only optical modes, which (re-)start to oscillate with the same phase (mode-locked laser operation) will pass the absorber. A prerequisite for mode-locking is a lower saturation intensity for the saturable absorber than for the gain medium

$I_{s\ abs} < I_{s\ gain}$. This condition supports pulse amplification within the laser resonator until an absorber bleaching is reached.

For the mode-locked laser operation three time constants have to be considered: τ_a the absorber recovery time, τ_n the recovery time of the gain medium and τ_c the cavity round trip time. The conditions for a stable mode-locking are discussed in [38]. The most favorable situation in mode-locked laser is given by

$$\tau_a < \tau_n < \tau_c \tag{3.4}$$

The recovery time of the absorber has to be shorter than that of the gain section in order to maintain the condition for a stable mode-locking by a higher saturation intensity $I_{s\ abs}$. It prevents a multiple pulse emission such as Q-switching within one cavity round trip period. The second relation is not satisfied in semiconductor mode-locked lasers with recovery times of the order of 100 ps. In this case the situation is described by $\tau_a < \tau_c \leq \tau_n$ and leads to a pulse emission with a lower peak power [38]. Higher gain currents can reduce the recovery time τ_n but it is limited to carrier transportation time scales of the order of x·10 ps.

Mode-locked operation can be distinguished by the type of modulation. It is possible to operate the free running laser, what is referred to as passive mode-locking. Alternatively a combined active and passive mode-locking, also known as hybrid mode-locking, can be performed by e.g. absorber or gain modulation. Hybrid mode-locking is attractive because it combines the short pulse width of passive mode-locking with the synchronization provided by an external reference [39, 40].

For active modulation a sinusoidal or δ-peak signal is used. A modulation frequency equivalent to the cavity round trip frequency is considered as fundamental mode-locking. Active modulation at a multiple or an integer fraction of the cavity round trip frequency is considered as harmonic or subharmonic mode-locking.

3.2.1 Mode-locked Semiconductor Laser

Mode-locking of laser diodes is a method often used to generate short pulses. Ref. [41] gives a review on mode-locked semiconductor lasers. Transform limited pulses can be generated having a width of less than 1 ps at a repetition frequency of several tens of GHz. Fundamental mode-locking is possible and promises low jitter values. A discussion on this technique follows in section 5.4 in more detail.

A mode-locked semiconductor laser emits a train of pulses with a repetition frequency f_{rep} equal to the the cavity round-trip frequency and therefore the frequency spacing $\Delta\nu_0 = \frac{v_{gr}}{2L}$. The facets of semiconductor laser diodes can form a laser cavity due to the refractive index of the semiconductor material of e.g. $n_{sc} = 3.22$ compared to surrounding air with $n_{air} = 1$. Therefore the operation of laser diodes with a typical length of about 300-500 μm corresponds to a repetition frequency of 150 to 90 GHz. As the desired pulse repetition is at 10 GHz or 40 GHz, these very high repetition frequencies can not be utilized for OTDM applications at present. Therefore, the cavity lengths of the laser diodes are extended either monolithically or by an external resonator. The saturable

absorber in the mode-locked laser can be generated by ion implantation or by a reversed biased section in a multi-section laser. These arrangements are discussed in the following.

Fig. 3.1 shows several arrangements of mode-locked semiconductor lasers. Fig. 3.1 (a) depicts a two-section laser diode consisting of a gain and a saturable-absorber (SA) section. The saturable absorber is provided by a short reversed biased section. Fig. 3.1 (b) shows an external-cavity mode locked laser. The saturable absorber may be generated either by ion-implantation in a single-section laser diode or by using a reversed biased section of a two-section laser diode (as shown in Fig. 3.1 (a)). In the frame of this work, the external-cavity laser is investigated for both kinds of saturable absorbers. Both laser types are discussed in section 4 and 5.

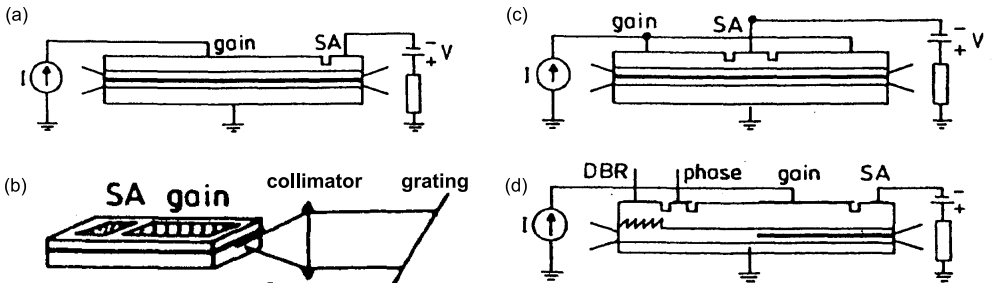

Figure 3.1: Configurations of different semiconductor mode-locked lasers (not to scale) [41]. (a) Laser diode consisting of a gain and a absorber section only, (b) laser diode with an external cavity extension, (c) colliding pulse setup and (d) monolithic cavity extension with phase section and DBR.

Figs. 3.1 (c) and 3.1 (d) show two examples of mode-locked lasers with monolithically extended cavities. More details on the investigation of the laser type shown in Fig. 3.1 (d), will be presented in sec. 5.3. Several other arrangements are also possible. A disadvantage of the monolithically integrated pulse source is the low tunability in repetition frequency and wavelength of about $\Delta f \approx 500\ MHz$ and $\Delta\lambda \approx 5\ nm$. These properties are determined by the optical path length of the diodes and the DBR grating, respectively. With a change of the operation currents in the laser sections such as the phase shift section (the passive section) minor differences in the pulse round trip time form the target repetition frequency can be corrected. Nevertheless the variations in the cavity length have to be kept in a small region, which requires exact cleaving of the laser-chips and is not reached by simple means. In the colliding pulse setup in Fig. 3.1 (c) the saturable absorber has to be centered exactly in the middle of the cavity [41]. Advantages of semiconductor mode-locked lasers are the compact set-up, the low driving current and the possibility of monolithic integration together with the possibility of low cost mass production.

3.2.2 Solid State Mode Locked laser

This type of laser consists of a solid state gain material and a separate absorber, in this example a SESAM (Semiconductor saturable absorber mirror, Fig. 3.2). The main difference to the semiconductor laser is the separately provided gain

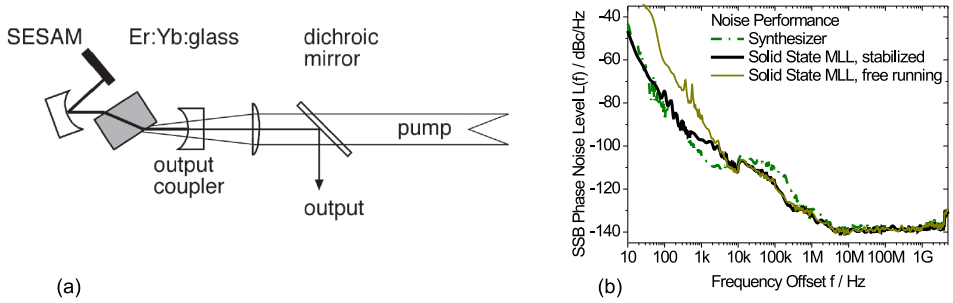

Figure 3.2: (a) Mode-locked Solid State Laser set-up [42] and (b) comparison of the measured single side band noise performance between the free running and stabilized Solid State Laser. The laser was operated at a carrier frequency of 10 GHz.

by a solid state material such as Er:Yb:glass. Extensively more pump energy has to be provided by a separate pump light source. The upper state of the gain material has a longer carrier life time of $\simeq$ 1 ms compared to few ns of in III-V semiconductor [20, 43]. Therefore the phase noise, especially at higher frequencies, is as low as the noise of an RF synthesizer used as reference to stabilize the pulse generation. In the SSB phase noise diagram in Fig. 3.2 the noise levels of the RF synthesizer, the free running solid state laser and the stabilized laser are shown. An active modulation is not necessary and in case of the gain also not possible. The stabilization of the cavity length is reached by the realignment of the cavity mirror. The repetition frequency of the pulse train is compared with an external RF frequency and a feedback signal for the cavity control is derived. The emitted 10 GHz pulse train has a pulse width of about 1.5 ps after a suitable length of DCF to compensate for a pulse chirp of -1.2 ps/nm.

Solid state mode-locked lasers have a good noise performance with a timing jitter as low as $\sigma_{rms} = 40$ fs, which is similar to the timing jitter of the external RF reference. The output power is several mW. Unfortunately commercially available lasers of this type offer no tunability neither in wavelength nor in repetition frequency. A monolithic integration of the laser cavity is not possible.

3.2.3 Harmonic mode-locking of a fiber ring laser

Fig. 3.3 (a) shows a typical set-up of a pulse source based on harmonic mode-locking in erbium doped fiber ring lasers (EFRL). The pulses generated with an EFRL have an almost sech^2 pulse shape, no pedestals and a low phase noise

identical to the RF source used for synchronization. However, the stabilization of the fiber ring is a rather elaborate task. The limited long term stability of such a device is shown in Fig. 3.3 (b) and will be discussed here briefly. This figure shows measurements of a section of the pulse train spectrum at different times with a delay to the first measurement as indicated in this figure. Due to the unavoidable length of a fiber ring resonator the fundamental repetition frequency is of the order of MHz. Therefore, for operation at 40 GHz harmonic mode-locking becomes essential. It requires exact suppression of lower frequency components, e.g. caused by the slopes of the modulator window, amplitude fluctuations and polarization mode dispersion (PMD). However, due to the limited perfection subharmonic components become apparent between the optical mode comb corresponding to the 40 GHz repetition frequency. It reduces the mode comb hight to values between 30 and 40 dB. The thermal influences on the resonator need a permanent control of cavity length and temperature in order to minimize wavelength drifts. In the worst case the cavity control drops out and requires some time for a realignment as shown in Fig. 3.3 (b) with the rise of subharmonics. Such realignment can become an outage time in system applications. The wavelength drifts are in the order of 0.01 nm and a problem for applications using a modulation format based on phase shift keying. If a stable operation point is found fiber ring laser generate pulse trains with good pulse quality with respect to phase noise and pulse shape. However, for application in laboratory environment or in flexible optical networks the tedious alignment becomes a drawback. For cavity stabilization a set-up as sophisticated as expensive is necessary.

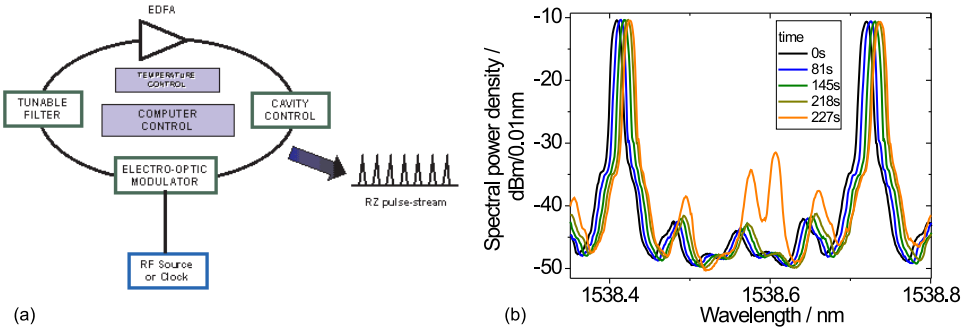

Figure 3.3: Harmonic mode-locked fiber ring laser: (a) set-up [44] and (b) the measured optical spectrum of a generated 40 GHz pulse at different times show wavelength drifts in the order of 0.01 nm induced by an thermal changes in the cavity. A stable suppression of subharmonics needs a careful alignment of the cavity length.

A number of publications deals with the optimization of this type of pulse source. Symmetric, transform limited pulses at gigahertz rates are reported by [45]. However, temperature changes affect the fiber length and lead to instabilities. Stable operation is reached e.g. with a clock signal following the changes

in cavity length [46]. Fine tuning of the wavelength as small as 0.0001 nm is reported in [47]. The super-mode competition within the ring laser has to be prevented to reduce noise figures. Suggested methods are the insert of a Fabry-Perot-Filter [45] or dithering the erbium fibre at a kilohertz rate [48]. In a 1.28 Tbit/s transmission experiment a 10 GHz fiber laser generated 3 ps pulses which were modulated with a PRBS signal and compressed to pulses shorter than 200 fs [49].

3.3 Modulation of cw- light

This optical pulse source comprises a CW laser and an electro-absorption modulator or a Mach-Zehnder modulator, which is driven by a high frequency sinus signal. Here the set-up with an electro-absorption modulator is considered solely (see Fig.3.4 (a)).

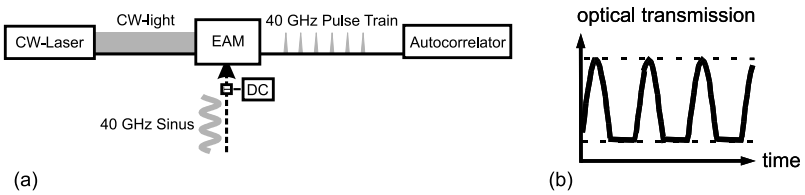

Figure 3.4: (a) Set-up for pulse generation with EAM and (b) transmission characteristic of an EAM with a combination of dc voltage and a modulation voltage [50].

Unlike mode-locking of several oscillating laser modes, the combination of a cw-light source with an electro absorption modulator relies on the generation of a frequency spectrum near the frequency $\nu = 193$ THz ($\lambda = 1550$ nm) of the cw light. The amplitude of the cw light is modulated by the 40 GHz RF signal applied to the EAM. If this RF signal would cause solely a sinusoidal modulation of the 193 THz carrier signal there are just 3 optical modes at 192.96, 193.00 and 193.04 THz. But, as shown in Fig. 3.4 (b), the transmission window $T_N(t)$ of the EAM can be shortened by a combination of DC bias with the RF voltage and the carved pulse train is more exactly approximated by a Fourier expansion of cosine terms

$$T_N(t) = \sum_{n=0}^{N} a_n \cdot \cos(n \cdot 2\pi \ f_{mod} \cdot t + \phi_0) \tag{3.5}$$

with the modulation frequency f_{mod} of e.g. 40 GHz. The product frequencies induced by the EA modulation are in phase due to the generation process. Therefore an additional mode-locking is not necessary. Fig. 3.5 (a) shows the corresponding spectrum (here the wavelengths) of a 40 GHz pulse train and (b) the autocorrelation of the generated 6 ps pulses. Wide pulse tails between the measured pulses reduce the contrast to values less than 25 dB (Fig. 3.5 (b)).

Fig 3.5 (c) shows the SSB phase noise curve of the generated pulse train and of the RF signal driving the EAM. The pulse generation by modulation of cw light has a timing jitter determined solely by the RF source.

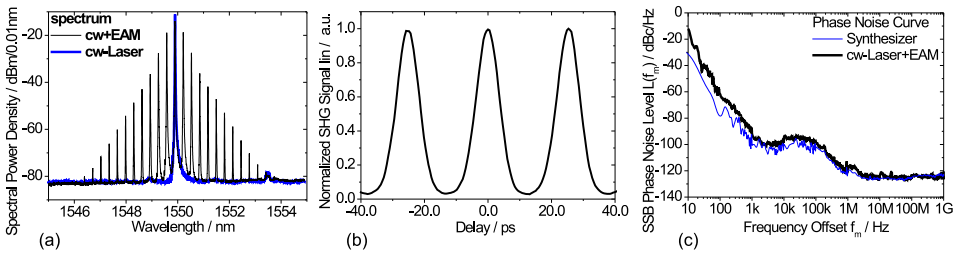

Figure 3.5: (a) Spectrum, (b) Intensity Autocorrelation (linear scale) and (c) SSB phase noise curve for a 40 GHz pulse train generated with a CW-Laser - EAM set-up

The electro-absorption modulators may be followed by an optical compression and/or optical regeneration stage. Using this technique 140 fs pulses were obtained with a repetition frequency in the range of 6.67 - 18 GHz at a wavelength of 1.54 - 1.553 μm [51]. In Ref. [52] pulses with 7 ps FWHM were compressed using an optical amplification and reshaping, a so-called 2R regenerator, based on self phase modulation in dispersion shifted fiber and subsequently optically filtered to provide transform limited 3 ps pulses. Using electro-absorption modulation, transform limited 3-4 ps pulses at 40 GHz with a 20 dB extinction ratio were reported in [53]. Here an improvement of the extinction ratio was reached by cascading two EAMs.

A monolithic integration of light generation and modulation is possible as shown in [54]. A combination of an EAM, a gain section and a DBR section was used for nearly transform limited 4 ps pulse generation at 40 GHz.

A drawback of this pulse source is the low output power. Pulse width and pulse contrast require subsequent pulse compression and pulse shaping for OTDM applications at 160 Gbit/s and higher. An advantage is the fast flexibility for choosing wavelength and repetition frequency. EAM based sources are often used for experiments with non return to zero (NRZ) data format.

Chapter 4

Architectures of Semiconductor Mode-Locked Laser

This chapter describes the investigated configurations of mode-locked semiconductor lasers (MLL), the external cavity mode-locked laser (EC-MLL) for a pulse generation at repetition frequencies around 10 GHz and the monolithic mode-locked laser (M-MLL) for repetition frequencies at 40 GHz. Both configurations of the laser diode were based on a semiconductor material with a buried heterostructure. Moreover the EC-MLL may have a saturable absorber (SA) based on Ion implantation, or a reversed bias section. Antireflection coating (AR) and electrical connection are important accessories of the semiconductor MLL.

4.1 External Cavity Mode-Locked Laser, EC-MLL

Fig. 4.1 (a) depicts schematically the External Cavity Mode-Locked Laser (EC-MLL) investigated in this work. It comprises a semiconductor laser diode in an external cavity. The laser diodes are mounted on a diamond heat sink to provide an efficient cooling during the laser operation. The laser diodes are Fabry Perot lasers with an antireflection coating (AR) on one facet. At this facet, the emitted light is collimated via a graded refractive index (GRIN) lens onto a grating, which defines one of the two mirrors of the cavity. The other mirror is given by the second facet of the laser diode. At this facet a saturable absorber is placed to achieve the mode-locking. A part of the laser pulse leaves the laser cavity at this facet and is coupled into a SSMF with a tapered fiber end. The external cavity laser is tuneable in the repetition frequency by the change of the grating position between 1 and 20 GHz and in the wavelength by a change of the inclination of the grating. The laser diode is described in detail in sec. 4.3.

The antireflection coating is described in detail in sec. 4.5. The antireflection coatings are optimized for just one wavelength which sets a limitation to the tuning range, because of a rise of the residual reflectivity. In consequence

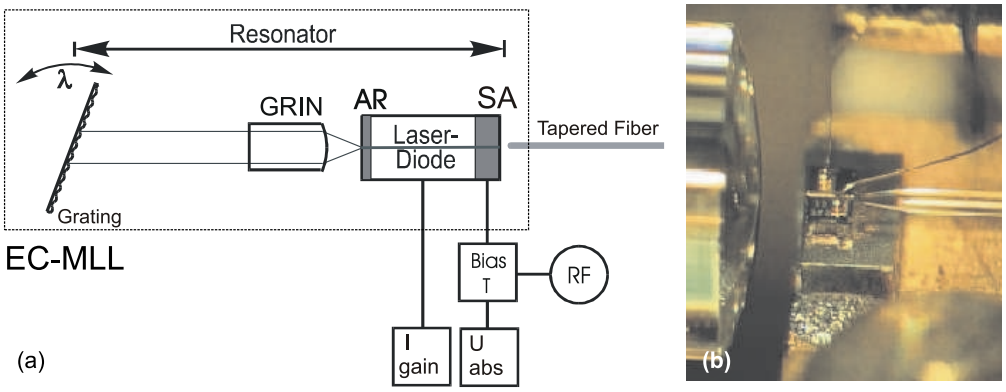

Figure 4.1: (a) Schematic set-up of the optical pulse source and (b) photograph of the laser diode with a gradient index lens on the left-hand side and a fiber taper on the right-hand side.

the strength of the saturable absorber cannot suppress the emission of trailing pulses. Another limitation of tunability to some 100 nm arises from the finite gain spectrum of the laser medium [55]. The saturable absorber (SA) is generated either by ion-implantation in the facet of the laser diode or by a reversed biased section of a two-section laser diode. More details on the saturable absorber (SA) are described in section 4.4. The electrical connection is provided by bond wires between the bond pads of the heat sink and the laser diode. The quality of this connection is considered in section 4.6.

4.2 Monolithic Mode-Locked Laser, M-MLL

In monolithic mode-locked semiconductor laser (M-MLL) diodes the extended cavity section is formed by a passive optical wave guide extension of the semiconductor chip. Fig. 4.2 shows the structure of the monolithic laser diode and the packaged M-MLL module.

The active section consists of a gain section and a saturable absorber section. The absorber and gain section have an identical multi quantum well (MQW) structure with 6 quantum wells. The absorber is operated with reversed bias. The passive extension comprises phase sections, a platinum stripe-heater section and a DBR section. The length of the sections is shown in tab. 4.1. The total cavity length of the laser chip has to be 1100 μm in order to provide the cavity round trip time of 25 ps.

The exact optical length depends of the refractive index which varies with the number of grown MQWs (ref. also to [57]). The additional sections of passive part of the monolithic cavity can be used for a increase of the refractive index by thermal effects (section with a platinum heater stripes) or for a decrease of the refractive index by electrical effects (phase section for insertion of additional carriers). Both facilitates to adjust the optical cavity length and therefore provides the possibility for the tuning of the repetition frequency [56].

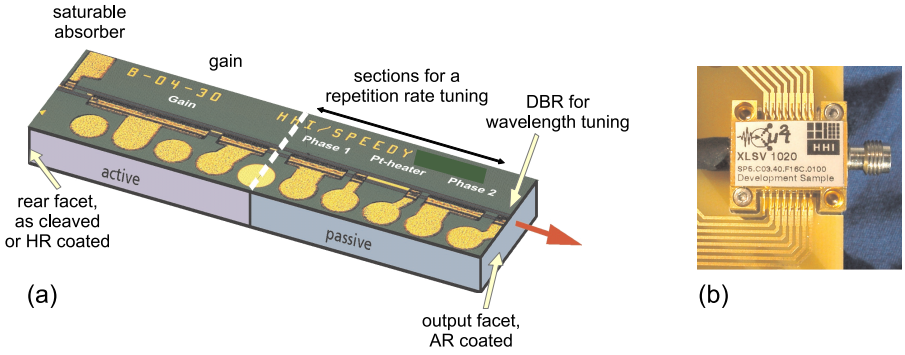

Figure 4.2: (a) Schematic view of the monolithic mode-locked laser diode and its integrated subelements and (b) the packaged M-MLL laser module. [56].

M-MLL section	SA	gain	Phase1	Pt heater	Phase2	DBR	Total
length / μm	50	560	155	125	155	50	1100

Table 4.1: Length of the M-MLL sections. The EC-MLL investigated in Sec. 5.2 comprise the saturable absorber section and the gain section only with a total length of 610 μm. For comparison: The implanted laser diodes have a shorter length of about 300 μm.

The selection of a suitable gain current and absorber voltage are further parameters to change the repetition frequency. These possibilities are required to compensate repetition frequency deviations caused by fabrication tolerances in the M-MLL cavity length, e.g. tolerances in the waveguide width and the thickness or tolerances of the cavity length caused by the cleaving of the waver. In total it is possible to compensate for deviations of a few μm by the refractive changes in the different laser sections. The DBR section is used to define the emission wavelength and includes the option of a fine tuning by 5 to 6 nanometer (ref. to Fig. 5.9). The active and the passive sections are butt coupled to minimize disturbing reflections within the laser resonator which is formed by the facet on the absorber side by a highly reflective (HR) coated facet in order to improve the cavity quality and the DBR section on the opposite end. Disturbing influences of the facet of the DBR section side are reduced by an antireflection (AR) coating. The laser output is coupled into a tapered fiber at the DBR facet (Fig. 4.2).

4.3 The Laser Diode

Fig. 4.3 shows the structure of the 1.55 μm InP laser diodes as they are used for the EC-MLL and M-MLL. The waveguide width is w = 0.9 and 1.2 μm for bulk and MQW laser diodes, respectively to ensure mono-mode (TEM_{00}) laser

operation. For ion implantation laser diodes with a bulk structure[1] have to be used. The MQW structure is the preferred choice for the MLL operated with a reversed bias absorber. The active region has a thickness of 150...200 nm. The buried heterostructure is grown with MOCVD technology. The active region is surrounded by a material of higher band-gap material and lower refractive index. Efficient and stable laser emission with low threshold currents can be achieved due to the index guiding of the buried heterostructure. The areas around the active material usually have a diode structure in opposite p-n-sequence. Therefore, leak currents can be avoided but on the expense of high parasitic capacities in the recombination regions. These capacities scale with the RF frequency applied for modulation. As an alternative, low capacity semi-insulating iron- blocking layers (InP:Fe) are introduced to circumvent this drawback. The simultaneous advances in wave guiding, carrier confinement and current guiding through the active area improves the modulation capabilities of these lasers. Additionally, the RF modulation power required for active (hybrid) modulation at frequencies up to 44 GHz can be kept reasonably low. However, it does not change the frequency roll off which limits the modulation frequency in general.

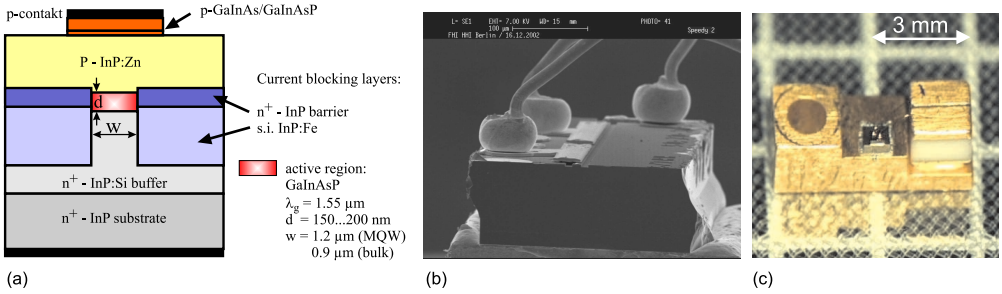

Figure 4.3: (a) Schematic cross section of the buried heterostructure of the laser diodes. The active laser waveguide consists of GaInAsP bulk or MQW material. (b) REM picture of the bonded EC-MLL chip, (c) EC-MLL chip mounted on a heat sink.

4.4 Saturable Absorbers

To achieve the hybrid mode-locking, a saturable absorber region has to be placed within the laser chip. A saturable absorber can be defined by a separate reversed bias section in a bulk or a MQW gain material. In laser diodes with bulk material an absorber section was defined by an ion implantation using nitrogen-, oxygen-, phosphorus ions or protons.Implantation by oxygen or phosphor-ions has been investigated by other groups [58]. In the frame of

[1] In case of MQW structures the volume of the active material available for an absorber based on crystal defects is smaller and requires longer absorber sections either by higher implantation energies, provided of their availability, or perpendicular implantation while shielding the gain region.

this work nitrogen ions were used for implantation of InGaAsP laser diodes with a bulk structure, adopting a technique investigated in [59]. The implantation of ions induces point defects in the semiconductor crystal, which act as fast non-radiative recombination centers in the semiconductor crystal. Thus, in consequence the carrier life time is reduced to picoseconds and satisfies the absorber condition as stated in eqn. (3.4). However, after an implantation thermal influences, already caused by high gain currents, have shown a complete annealing and remove the absorber properties. By increasing the implantation dose the formation of a stable defect cluster is obtained and provides a permanent saturable absorber characteristic. Further increase of the implantation dose leads to amorphous structures or formation of poly-crystalline material and provides a lower number of crystal defects acting as fast recombination centers. It may destroy the band structure needed to operate the laser diode. A detailed analysis for III-V materials can be found for GaAs in [60] and for InP in [61, 62]. In consequence there is an optimum implantation dose for a fast saturable absorption. The determination of the accurate implantation dose for the laser diodes investigated in the frame of this work are typically of the order of $10^{+12} cm^{-2}$. The dose has to be determined individually for every laser diode. This is done by controlling the change of laser threshold current to higher values or the suppression of the switch on of the lasing in the typical region of operation currents as depicted in Fig. 4.4 (b) with the dashed-dotted lines. The final power-current (L-I-) curve should show a change of some 10 mA or more to higher current values (dashed line) compared to the L-I- curve of the laser diode before ion implantation.

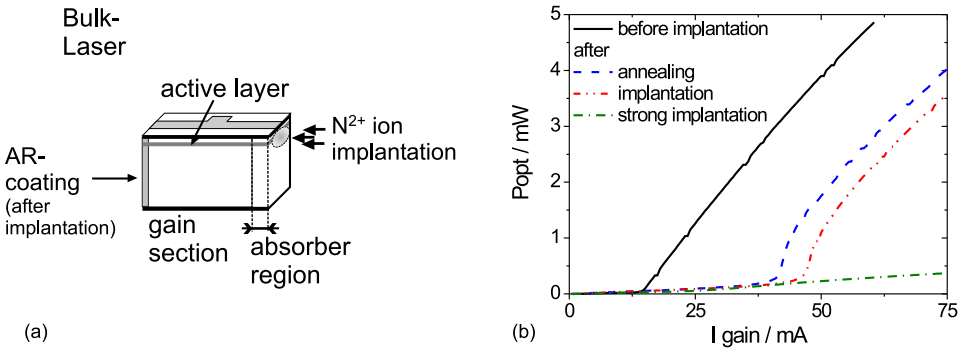

Figure 4.4: (a) schematic view of a bulk laser diode and implantation of N^{+2} ions at one laser facet for saturable absorption and (b) L-I curves for the laser diode without AR coating before ion implantation (solid line), after ion implantation (dash-dotted lines), after thermal annealing (double dashed line) and further absorber annealing (dashed line).

An annealing has to follow in order to finish the observed partial repair of crystal defects in a short time. The absorber strength can be evaluated after-

wards to confirm long term properties of the mode-locked operation. Otherwise the dose has to be increased by an additional implantation step. The implantations were carried out at the Hahn-Meitner-Institute in Berlin. The nitrogen ions were implanted perpendicular onto a diode facet with a kinetic energy of about 10 MeV. The energy defines the penetration depth, usually limited to 5 to 10 μm. The bulk structure is required for the implantation technique as MQW structures showed a failure due to QW intermixing after an implantation.

The saturable absorber based on a separate reversed bias section avoids the efforts of the implantation technique which is not everywhere and always available. However, due to the longer time constants for carrier depletion the trailing pulses become more critical for these lasers. A simple way to cope with the longer absorber recovery time is the increase of the length of the laser diodes. An optimization of the MQW structure, such as strained layers, focus on the reduction of the carrier lifetime and carrier escape times. A further possibility is to use absorber structures grown by MBE low temperature (200°C) epitaxy which show shorter time constants for recombination processes (cf. e.g. [63]). The shorter time constant is caused by additional recombination levels in the energy band gap of the semiconductor. On the other hand, it requires higher efforts on the technological process, e.g. by an additional selective area growth process. In case of the M-MLL in total five instead of four growth steps would be necessary.

4.5 Antireflection Coating

The refractive index of semiconductor laser diodes is determined by the refractive index of the active material InGaAsP, $n_{InGaAsP} = 3.5$ and the surrounding material (cadding) InP, $n_{InP} = 3.22$. The effective refractive index n_{eff} for the spherical waves depend on the exact thickness d of the active material [64]. For the investigated laser diodes d = 150 nm and n_{eff} has a value of 3.25. With the surrounding air ($n_0 = 1.0$) the reflectivity R at each laser facet is given by the plane-wave approximation

$$R = \left(\frac{n_{eff} - n_0}{n_{eff} + n_0} \right)^2 = 0.28 \tag{4.1}$$

.

This is a small value in comparison to the mirror reflection of R > 0.9 used in other laser types, e.g. gas laser. However, due to the high gain coefficient g of the semiconductor material of up to 10^3 cm^{-1}, higher losses can be tolerated. For optimization of the laser performance, the diode facets can be coated with a suitable material to increase (HR) or decrease (AR) the facet reflection. By experience made with this type of laser the operation of an EC-MLL requires the AR coating with R < 10^{-4} on one side of the semiconductor diode to achieve a coupling to the external cavity and to suppress the emission of trailing pulses (see Fig. 4.1).

The EC-MLLs investigated in this work were antireflection coated inside the cavity while the M-MLL were antireflection (AR) coated at the output facet of

the DBR side and high reflection (HR) coated at the absorber side (Fig. 4.2). The AR-coating at the DBR end of the laser diode is required in order to avoid a second resonator defined by the facet of the laser diode. Here a residual reflectivity of the laser facet of $R < 10^{-3}$ is sufficient. This lower requirement is adequate as the residual reflectivity is only relevant for the part of the laser pulse, that is leaving the laser cavity. The antireflection coating is accomplished by sputtering of TiO_2 and SiO_2 materials on the facet. The energy balance of a semitransparent laser mirror is

$$R + T + A = 1 \tag{4.2}$$

with R: the reflectivity, T: the transmission and A: the absorption of the interface. The low absorption A is important in order to avoid a thermal destruction of the AR coating and the facet at high laser intensities. During the sputtering process, the sputter rate, the thickness and the O_2-partial pressure have to be optimized for a specific target wavelength. The AR coating for a broader wavelength region or for higher reflectivity/transmission requires a multiple layer coating with layers, alternating with a higher- (H) and lower (L) refractive index. For a high reflectivity the sequence is LH(LH...), on the other hand for antireflection coating the sequence is HLHLHL, were H = TiO_2 and L = SiO_2. In the present work, only one pair of TiO_2 and SiO_2 coatings was sputtered. The required thickness of both layers depends on the refractive index of the semiconductor material, which has to be determined very precisely. By variation of the thickness an optimum replacement for a quarter wave layer is found (Table 4.2).

Material	refractive index	thickness
Laser active material cladding	 $n_{InGaAsP} = 3.5$ $n_{InP} = 3.22$	
TiO_2	$n_2 = 2.24$	$d_2 = 123.7$ nm
SiO_2	$n_1 = 1.48$	$d_1 = 183.2$ nm
Air	$n_0 = 1$	

Table 4.2: Parameters of the AR coating used for the layers deposited on one laser facet for EC-MLL applications.

The quality of the AR coatings can be evaluated adopting a technique described in [65, 66]. This method relies on the comparison of the ASE spectra of the laser diode, which is operated without cavity and below threshold. The spectral power density and the height of the mode comb are measured on the front and back side of a laser diode to derive an information about of the gain per round trip and the residual reflectivity. The detailed calculation of the AR values can be found [65]. Fig. 4.5 (a) shows the emission spectrum of a laser diode, with an AR-coating on one facet. The optimum of the AR coating can be identified by the disappearance of the mode comb, in this case at 1540 nm.

For the spectrum shown in Fig.4.5 (a) a residual reflectivity of the order of 10^{-5} was achieved for wavelengths between 1535 nm and 1545 nm (b). For

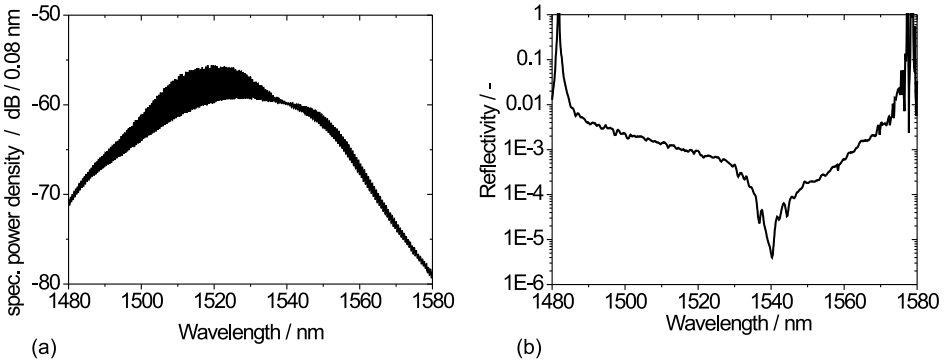

Figure 4.5: (a) Optical spectrum emitted from the AR coated facet of a laser diode and (b) reflectivity of a laser diode with antireflection coating (AR) on one facet.

wavelengths outside of this range the residual reflectivity exceeds $1 \cdot 10^{-4}$. It is possible to minimize the residual reflectivity for a broader wavelength range by sputtering of e.g. 4 layers. However, each of these layers has to meet the exact value of thickness otherwise the net result is an antireflection coating for a wider wavelength range, but with a higher value for the residual reflectivity.

A strong reduction of the requirements on the accuracy of the AR coating can be achieved by the use of bend waveguide structures. In this case, the waveguide orientation of the laser diode is not perpendicular to the output facet of the resonator. It has a bending with a final inclination of e.g. 7° at the laser facet towards the inner side of the cavity. In consequence, the light emitted into the external resonator has an inclination of about 20°, because of the semiconductor/air interface. Most of the reflected light is leaving the waveguide and thus, does not contribute to the rise of unwanted disturbing trailing pulses in EC-MLL configurations. One example of EC-MLL with bent waveguide was investigated. It was not possible to operate the laser without antireflection coating in the external cavity. If antireflection coating remains necessary, it has to be adapted to the new light path with an off-axis angle of 7°. In this case the evaluation of the AR-coating as described in Fig. 4.5 fails to provide reasonable results for the optimization. A rather poor antireflection coating provided a trailing pulse suppression (TPS) of 27 dB with the first run of the laser coating. For laser diodes with a waveguide orientation perpendicular to the output laser facet the coating has to be optimized in several steps to reach a comparable trailing pulse suppression (TPS). A curved waveguide can be grown with an off-axis angle of up to 15° and reduces the requirements on antireflection coatings even further (cf. SOAs with a curved waveguide in [67]). However, it becomes more and more difficult to handle the collimation of the beam in the external cavity with a lens of high numerical aperture lens over the lateral width of the laser facet.

4.6 Electrical Connection

The mode-locking in pulse sources is most often achieved by a combination of passive and active mode-locking. An effective carrier density modulation for active mode-locking requires a low loss radio frequency (RF) connection into the active laser region for the 10 GHz or even 40 GHz RF signals.

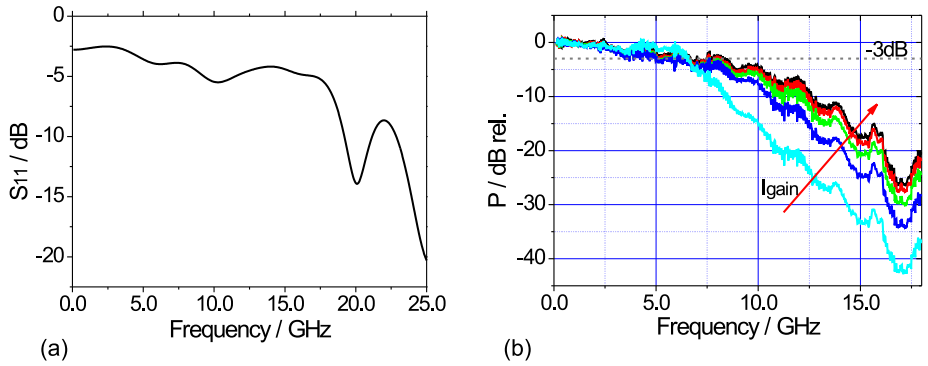

Figure 4.6: (a) RF Reflectivity and (b) optical small signal response of a semiconductor laser diode as used for the EC MLL.

Limitations of the modulation capability can have several reasons. On the one hand side there is the intrinsic modulation frequency limit in the semiconductor chip. On the other hand side external parameters such as parasitic capacities of connection pads and connecting wires have to be minimized. The connection between the external RF circuit and the laser chip cause a reduction of transmitted RF power onto the laser chip due the impedance mismatch. The series resistance of the laser diodes is typically 3-5 Ω compared to the line impedance with 50 Ω. Therefore a share of the RF modulation power will be reflected. For an impedance matching a serial resistor can be introduced but will not increase the submitted power. Alternatively, a circuit for impedance matching can only be optimized for limited frequency bandwidth, e.g. between 10.0 GHz and 10.7 GHz as used for forward error correction (FEC) of a 10.0 GHz signal, but does not match the resistivity for the full tuning range of an EC-MLL between 1 and 20 GHz.

In order to evaluate the electrical matching, S_{11} parameter measurements have been done (cf. Fig. 4.6 (a)). For modulation frequencies close to 10 GHz a reflectivity of $\leq 5\ dB$ is observed. For frequencies of 20 GHz and above, the absorption of the bias-T causes a reduction in the measured reflected power. Fig. 4.6 (b) shows the small signal response characteristic of the laser diode for gain currents at 25 mA, 50 mA ...125 mA. The small signal frequency response of the laser diode describes the modulation capability of the mode-locked laser. The low pass behavior and the missing resonance peaks indicate the reduction of the modulation power due to the impedance mismatch. For

the series resistance values of the laser diode $z_E = 5\ \Omega$ and of the SMA wire $z_L = 50\ \Omega$ a reflectivity r of $r = (z_E - z_L)/(z_E + z_L) \approx 0.8$ was expected and is confirmed by electrical time domain reflectometry.

At a frequency of 10 GHz the modulation response decreased by 7.7 dB and 4.5 dB for gain currents of 50 and 125 mA, respectively. Oscillations in the decreasing wings of the curves have to be attributed to resonances due to an electrical mismatch of the bond wiring to the laser diode.

For the operation of a hybrid mode-locked 10 GHz laser, these losses can be tolerated, e.g. by an increase of the modulation power. However, the operation of a 40 GHz mode-locked laser requires an improvement of the RF connection to enable a hybrid mode-locked operation. An improved RF connection was implemented by the company "u2t photonics" using a micro-strip connection and an impedance matching circuit. The bandwidth for the RF matching was about 1 GHz around the M-MLL operation frequency and allowed a hybrid mode-locked operation with an RF power as low as 12 dBm. In other publications [68] open RF stubs were trimmed for optimization of the electrical circuit. There the RF modulation power needed for hybrid mode-locking of a M-MLL was reduced to -20 dBm at the Bias-T output.

Chapter 5

Performance Characteristics of EC-MLL and M-MLL Pulse Sources

In this chapter detailed investigations on the performance characteristics of the different semiconductor mode-locked laser configurations, described in Chapter 4 are reported. Namely the EC-MLL with different saturable absorbers (SA) and the M-MLL are compared. The objective of the investigations was to evaluate these configurations for their application as pulse source in a 640 Gbit/s transmitter.

5.1 Characteristics of the EC-MLL with Saturable Absorber based on Nitrogen Bombardment

5.1.1 Bias Conditions, Output Power, Pulse Width and Chirp

Fig. 5.1 shows the power- current (L-I) characteristic of the EC-MLL. The three insets are autocorrelation traces in three regions of the laser pulse emission. Due to hysteresis a gain current of 53 mA is necessary to start the laser operation. For steady state laser operation a minimum gain current of 35 mA is necessary. If the gain current is larger than 45 mA, the EC-MLL pulses are accompanied by a single satellite pulse (inset of Fig. 5.1). Due to the high gain current, the round trip gain for trailing pulses is sufficient to saturate the absorber a second time. At high gain currents the condition for stable mode-locking in eqn. (3.4) is not fulfilled, because the gain recovery becomes faster. If the input current is further increased above 72 mA, a second satellite pulse appears. The emission of satellite pulses is connected with a change of the cavity round trip time (repetition frequency of the passively mode-locked laser) and the output power of the EC-MLL. The useful operation range of this particular EC-MLL is at injection currents between 35 mA and 45 mA. This range (including the lowest operation current) can be shifted to higher currents by a higher implantation dose in the saturable absorber.

A FROG measurement was made for these laser pulses in order to evaluate

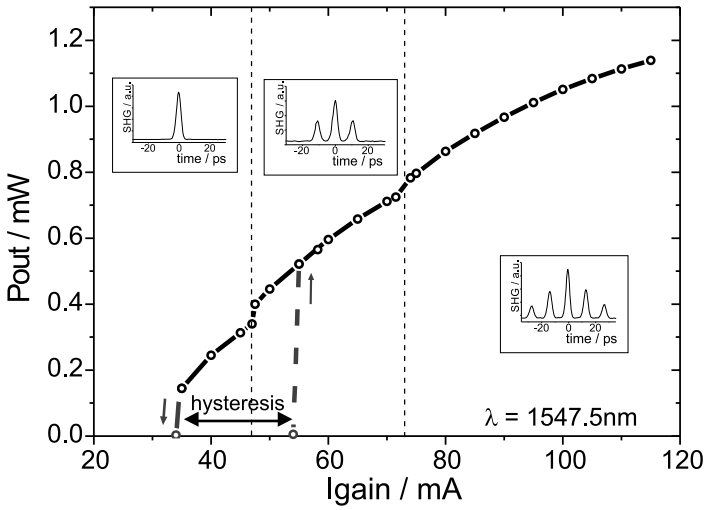

Figure 5.1: EC-MLL with a saturable absorber (SA) based on Nitrogen bombardment: L-I- characteristics with hysteresis and satellite pulses (inset: autocorrelation curves) at higher gain currents.

the pulse shape and the chirp. A linear positive chirp of 150 GHz was observed and corresponds to a wavelength dependent group delay t_{group} of 1 ps over the spectral pulse width (FWHM) of 1.6 nm (cf. Fig. 2.4 and Eqn. 2.3). This slight chirp can be compensated by transmission through a dispersive fiber with a Dispersion of $D = 1.0ps/1.6nm = 0.63ps/nm$, approximately 30 m SSMF.

Within the operation range given by the gain current, it is possible to change the wavelength over the complete C- band by the inclination of the grating. For this wavelength tuning only minor changes of the pulse properties are observed. The exchange of the grating with 300 lines/mm by a grating with 150 or 600 lines/mm has an influence on the ratio between spectral and temporal pulse width and on the phase noise of the laser (Tab. 5.1) and will be discussed in Section 5.4.2.

grating [lines/mm]	spectral width [nm]	temporal width [ps]	timing jitter [fs]
150	2.1	1.3	190
300	1.4	2.1	140
600	0.8	3.2	70

Table 5.1: Comparison of pulse properties generated by the EC-MLL using gratings with 150, 300 and 600 lines/mm.

Gratings with 150, 300 and 600 lines/mm caused a temporal width of 1.3, 2.1 and 3.2 ps and a spectral width of 2.1 nm to 1.4 nm and 0.8 nm, respectively. By the change of the gratings the timing jitter was measured as 190 fs, 140 fs

and 70 fs, respectively. This will be considered in more detail in Sec. 5.4.2. In the measurements the same RF synthesizer with a constant RF modulation power was applied. For example, a frequency spectrum for the laser operated with a grating with 600 lines/mm is shown in Fig. 1.3.

5.1.2 Noise Characteristics

Fig. 5.2 shows measurements of the RF spectrum of the EC-MLL. The RF spectrum was measured from 0 to 13 GHz (Fig. 5.2 (a)) and shows a clean carrier signal. Disturbing frequencies, e.g. caused by amplitude modulations, are suppressed to 70 dB below the carrier signal. Fig. 5.2 (b) depicts the measured SSB phase noise for the EC-MLL. The EC-MLL was operated at 1550 nm with a gain current of 37 mA, which is close to the threshold. The generated pulses had a width of 2.1 ps.

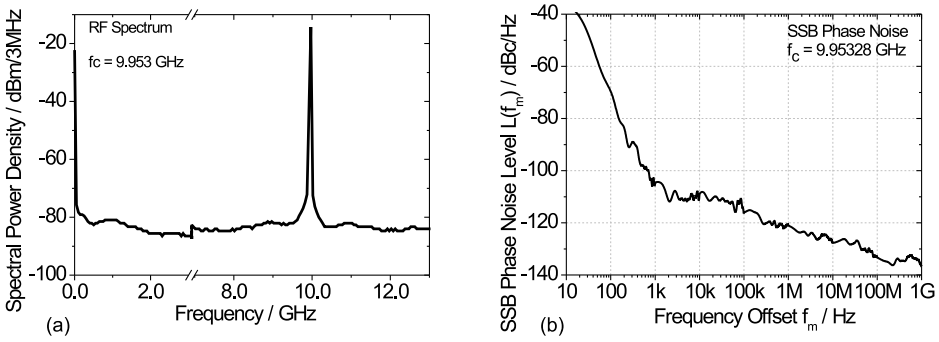

Figure 5.2: (a) RF-spectrum between 0 to 13 GHz and (b) single side band (SSB) phase noise spectrum of the EC-MLL.

A timing jitter of 70 fs was obtained for the EC-MLL by the integration within a frequency offset interval between 100 Hz to 10 MHz from the carrier frequency as discussed in sec. 2.3. An RF source with a jitter of 50 fs and an RF power of 29 dBm was used. Since the integration range of the SSB phase noise measurement technique is limited as an alternative an electrical sampling oscilloscope was used for timing jitter evaluation in particular for the low frequency components $f_m < 100$ Hz. The timing jitter σ_{rms} was measured to be 210 fs, including a jitter of 180 fs caused by the sampling oscilloscope. A rough estimation yields that phase noise with frequencies below 100 Hz add not more that 100 fs to the total jitter value. However, these components are not relevant if a clock recovery is used in the transmission set-up. The amplitude noise (AN) of this laser was measured to AN $\leq$ 2 %.

5.1.3 Locking and Tuning Range of the Pulse Repetition Frequency

Fig. 5.3 (a) depicts the timing jitter of a hybrid mode-locked laser versus the detuning of the RF modulation frequency f_{rep} from the repetition frequency $f_{0\ passive\ ML} = 9.95634$ GHz of the passively mode-locked laser. The detuning characterizes the locking range of the laser cavity, if the other pulse characteristics can be kept almost unchanged. This measurement was repeated for different RF modulation powers. Hereby a large share of the RF power is lost due the resistivity mismatch (cf. sec. 4.6).

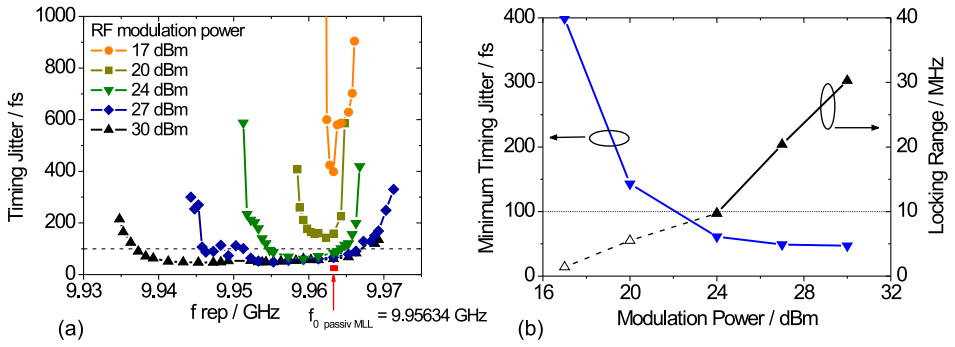

Figure 5.3: (a) Timing jitter of the EC-MLL measured with the SSB noise measurement versus the detuning of the external synchronization frequency at different RF power. (b) minimum timing jitter and locking range in dependence of the RF modulation power.

For hybrid mode-locking the lowest timing jitter is measured for the repetition frequencies lower than the corresponding repetition frequency of the passively mode-locked laser. The RF modulation yields an increase of the temperature of the device and leads to an increase of the refractive index of the laser chip. In consequence the optimum modulation frequency is shifted up to 15 MHz towards lower values.

For an RF modulation power of 30 dBm applied to the bias-T (ref. Fig. 4.1) the timing jitter remained below 100 fs in a tuning range of 30 MHz. At the edges of the tuning range a strong increase occurred until the hybrid mode-locking became instable. With the reduction of the modulation power the tuning range becomes smaller and eventually the hybrid mode-locking becomes too weak to provide timing jitter values below 100 fs (Fig. 5.3 (b)). An increase of the modulation power reduces the timing jitter value down to 50 fs, however this reduction saturates. For these measurements a grating with 600 lines/mm and an RF-synthesizer with a SSB-phase noise of $\sigma_{rms} = 40\ fs$ [100 Hz - 10 MHz]. The pulse width of the hybrid mode-locked laser was ≤ 1.2 times the transformation limit for a sech^2 pulse shape in the 30 MHz tuning range.

5.2 Characteristics of the EC-MLL with Saturable Absorber based on a Reversed Bias Section

The laser set-up described in section 5.1 requires an elaborate implantation of Nitrogen Ions into a laser diode with bulk structure to form a saturable absorber for mode-locking. As an alternative, laser diodes with multiquantum well structure were fabricated at HHI. The laser diodes are subdivided into two sections. One of the two sections was operated with a reversed biased section as a saturable absorber. The active waveguide of this laser structure had 6 quantum wells. The length of the gain section was 560 μm and the absorber had a length of 50 μm. Both sections were separated by a 20 μm region without electrical contact in order to provide an electrical separation of 2.8 to 3.8 kΩ between the gain and the absorber section. For the investigated laser diode the antireflection coating of the laser facet inside the laser resonator has a remaining reflectivity in the order of 10^{-5}. The grating of the investigated laser cavity had 300 lines/mm and was not changed for the investigations described in Chap. 5.2. As show later (Fig. 5.12), a change of the grating has a influence on pulse width and timing jitter too.

5.2.1 Bias Conditions, Pulse Width and Chirp

The performance of the EC-MLL with a two section mode-locked laser depends on the two parameters gain current I_{gain} and absorber voltage U_{abs}. In the following the absorber voltage is written as a positive value, although it represents a reversed bias.

Fig. 5.4 (a) shows the region of mode-locked laser operation (grey area) in dependence of the gain current and the absorber voltage. The higher the gain current, the higher the absorber voltage has to be for sufficient mode-locking. At gain currents less than 60 mA, the generated pulses were broad and showed wide pulse tails, which indicates incomplete mode-locking. Optimum mode-locking characteristic was possible at gain currents above 60 mA and absorber voltages between 1.0 V and 3.5 V. Higher absorber voltages were not applied in order to avoid a failure due to a break through of the laser diode. The laser operation was limited for each gain current by a maximum absorber voltage (describing the absorber strength). The pulses with shortest temporal width were observed at this limit (the lower borderline of the grey area in Fig. 5.4).

Fig. 5.4 (b) displays the temporal and spectral pulse widths for a selected gain current of 90 mA in dependence of the absorber voltage. The exact position of the mode-locking area in Fig. 5.4 depends on the alignment of the laser cavity and the grating, which is used in this resonator set-up.

The emitted pulses had a time-bandwidth product of 1.5 to 2.0 times the time-bandwidth of transformation-limited sech^2 pulses. Especially for low absorber voltages a higher time-bandwidth product was measured. In order to investigate the chirp, the generated pulses were transmitted over several sections of SSMF and the pulse width was measured versus the SSMF length. These measurements were taken at a constant gain current of 90 mA and an absorber voltage of 1.9 V, where the RF frequency spectrum showed low con-

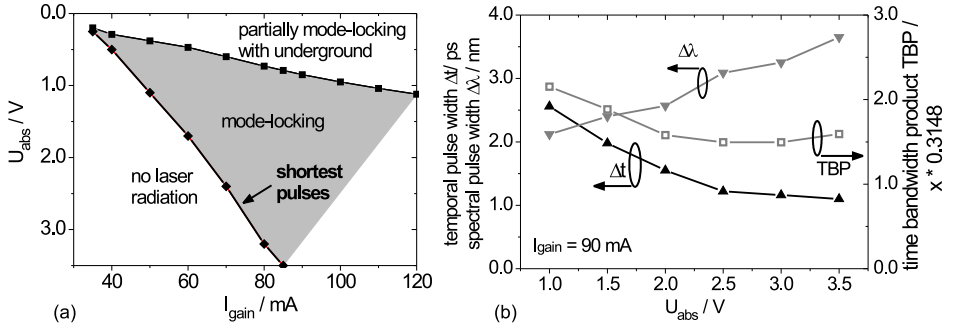

Figure 5.4: (a) Bias conditions for the passive mode-locked laser operation of the EC-MLL and (b) Temporal and spectral pulse width in dependence of the absorber voltage at a constant gain current $I_{gain} = 90\ mA$ and a grating with 300 lines/mm.

tributions from amplitude noise (cf. Fig. 2.5 (b)). The emission wavelength was 1550 nm and the cavity length was kept constant during the measurements. The spectral pulse width was 2.1 nm and 1.5 nm for hybrid mode-locking with gain modulation and hybrid mode-locking with absorber modulation, respectively. Simultaneously a temporal pulse width of 2.7 ps and 3.5 ps, respectively, was measured.

It was possible to compensate the chirp by transmitting the pulses through an appropriate length of 50 and 90 m SSMF for gain and absorber modulation, respectively. A SSMF fiber length of 20 m was already necessary for the measurement set-up being used. The observed chirp of the emitted pulse train is due to the self-phase modulation caused by gain saturation in the gain section, which is not compensated inside the cavity (cf. [69, 70]).

The minimum pulse width was 1.4 ps and 1.7 ps for gain and absorber modulation. It counts to 1.1 times the transformation limit of sech^2 pulses for both of the hybrid mode-locking operations.

5.2.2 Noise Performance, Trailing Pulses and Pulse Power

Fig. 5.5 (a) shows the timing jitter of the generated pulse train versus the absorber voltage. The gain current was kept at 90 mA. The lowest timing jitter of the hybrid mode-locked laser (absorber modulation) was σ_{rms}=55 fs was measured at an absorber voltage of 1.0 V and increased for higher absorber voltages. Therefore the generation of shortest pulses is accompanied by a higher timing jitter (cf. Fig. 5.4 (b)). Fig. 5.5 (b) shows the fiber coupled average power of the pulse train. With an increase of the absorber voltage the output power was reduced from 0.69 mW to 0.3 mW. For stable mode-locked operation the maximum output power for this laser was 0.46 mW (-3.4 dBm) at $U_{abs} = 1.0$ V. The trailing pulse suppression (cf. Fig. 1.2) can be increased from 14 dB at the onset of complete mode-locking to 32 dB for absorber voltages of 1.5 V and

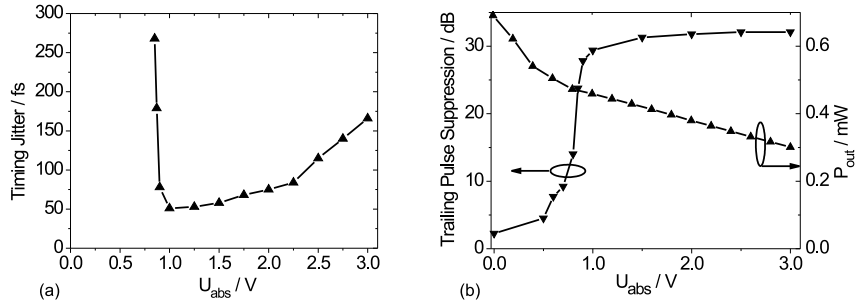

Figure 5.5: (a) Timing jitter versus absorber voltage, (b) Trailing pulse suppression and output power in dependence of the absorber voltage. Both measured at a gain current I_{gain} of 90 mA. The absorber section was hybrid mode-locked with an RF power of 20 dBm.

above. For higher absorber voltages there is no further improvement.

5.2.3 Comparison of Gain and Absorber Modulation

The two section laser device in the EC-MLL enables both, gain or absorber modulation by applying an external RF signal. Therefore the question is, whether there is an advantage for one or the other RF modulation with respect to the pulse width and jitter of the EC-MLL. The bias condition was chosen to I_{gain} = 90 mA and U_{abs} = 1.7 V.

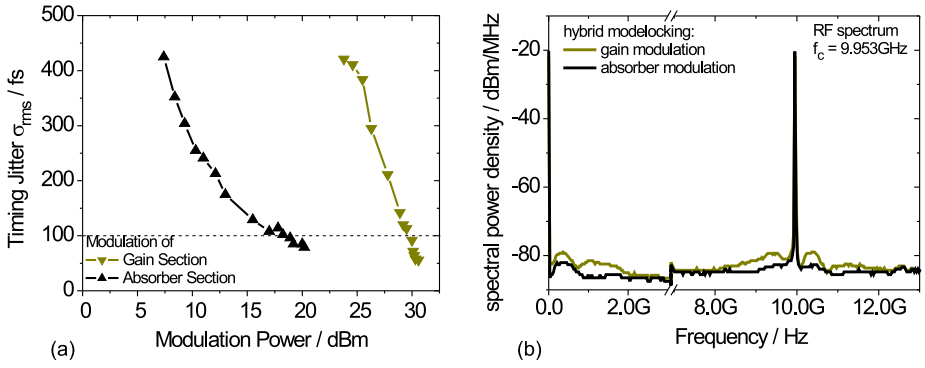

Figure 5.6: Comparison of gain and absorber modulation for hybrid mode-locking: Timing jitter (a) in dependence on the external modulation power and RF spectrum between 0 and 13 GHz for a modulation power of 20 dBm and 30 dBm, respectively (b).

Fig. 5.6 (a) compares the SSB phase noise curves and Fig. 5.6 (b) the RF spectrum of the 10 GHz pulse train for gain- and absorber modulation. The maximum RF power was 30 dBm for gain modulation and 20 dBm for absorber modulation. Despite the lower modulation power the timing jitter $\sigma_{rms} = 80$ fs for the absorber modulation was comparable with the timing jitter performance of $\sigma_{rms} = 70$ fs for the gain modulation.

The RF spectrum for absorber modulation showed slightly lower amplitude noise components close to the zero frequency and as mixing product around the carrier frequency.

5.3 Characteristics of the M-MLL

The architecture of the monolithic 40 GHz mode-locked laser (M-MLL) and its module packaging are described in Chapter 4 (cf. Fig. 4.2). In the following the basic properties of this M-MLL are discussed.

5.3.1 Bias Conditions, Pulse Width and Output power

In Fig. 5.7 (a), the grey area represents the region of absorber voltages U_{abs} and gain currents I_{gain}, where a stable mode-locking is possible at the fundamental pulse repetition frequency of 40 GHz. Light grey squares represent a short pulse width and dark gray a broad pulse width. For high absorber voltages the pulse width is shorter than for low absorber voltages.

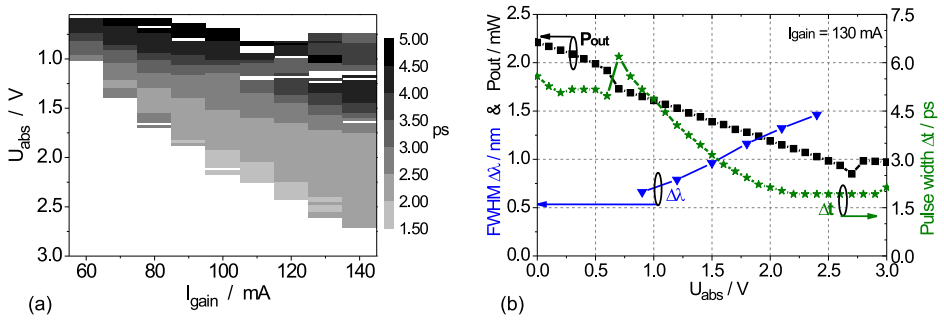

Figure 5.7: (a) Pulse widths of the M-MLL for different bias conditions at the gain and absorber section [71]. (b) Spectral pulse width, fiber coupled output power and pulse width versus absorber voltage at a constant gain current of 130 mA. Both diagrams were measured in passive mode-locked laser operation.

The operation region of the M-MLL is qualitatively similar to that of the EC-MLL with a saturable absorber based on a reversed bias section as shown in Fig. 5.4. For higher U_{abs} a higher I_{gain} is required in order to overcome the additional losses of the saturable absorber. The operation of the M-MLL at a repetition frequency of 40 GHz instead of the EC-MLL at a repetition frequency

of 10 GHz requires a slightly higher gain current, as shown in Fig. 5.7 compared to Fig. 5.4.

As Fig. 5.7 (b) shows, the pulse width Δt decreases from 6.0 ps to 1.8 ps for increasing U_{abs} at a given I_{gain} = 130 mA. Simultaneously, the spectral width $\Delta\nu$ increases, such that the time-bandwidth product $\Delta\nu\Delta$t remains between 1.1 and 1.4 times the time-bandwidth product of transformation limited sech^2 pulses. The output power is reduced from P_{out} = 1.65 mW to 1.03 mW within the region of stable mode-locking. Distinct changes of the pulse width and of the output power at U_{abs} = 0.7 V and for the output power also at U_{abs} = 2.7 V can be explained in context of the noise properties of the M-MLL, which are discussed in the next section.

5.3.2 Noise Properties and Chirp

Fig. 5.8 (a) shows measurements of RF spectra at a given gain current I_{gain} = 130 mA for various values of the absorber voltages U_{abs}. The absorber voltage was increased from 0.0 V to 3.0 V in 0.3 V steps. For absorber voltages U_{abs} below 0.9 V a multiple of spikes appeared in the frequency spectrum close the zero and as mixing products around the carrier signal. Such spikes indicate Q switching operation of the laser. An increase of the absorber voltage to $U_{abs} \geq$ 0.9 V caused these spikes to disappear and enabled a mode-locking at one stable pulse repetition frequency close to 40 GHz. With a further increase of the absorber voltage the amplitude noise components close to zero became apparent (cf. Sec. 2.3) and eventually, for absorber voltages at $U_{abs} >$ 2.4 V, the laser operation changed from the so-called cw- mode-locking to the Q switched mode-locking [72]. In the RF spectrum the Q switching can be identified by frequency components at 3.5 GHz, its multiples and the mixing frequencies around the carrier.

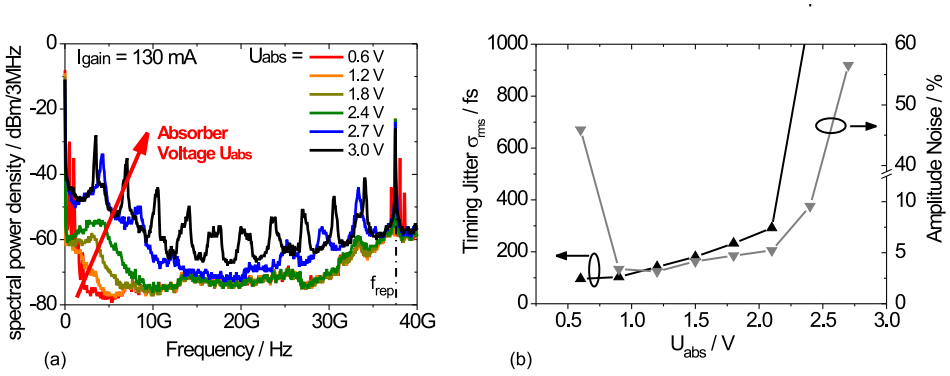

Figure 5.8: (a) Influence of the absorber voltage on the RF spectrum and (b) on the timing jitter and the amplitude noise.

Such instable mode-locking, also known as pulsation, was not observed for

mode-locked laser diodes operated in the EC-MLL at 10 GHz, although a slight increase of amplitude noise components and timing jitter was also found there for high absorber voltages.

Fig. 5.8 (b) shows the timing jitter and the amplitude noise in dependence of the absorber voltage. The measurements were performed with an electrical spectrum analyzer (SSB phase noise measurement) and a sampling oscilloscope, respectively (cf. sec. 2.3). The amplitude noise is reduced if the absorber voltage was increased to 0.9 V and a stable mode-locking operation became possible. However, higher absorber voltages cause an increase of the amplitude noise from 3 % to 10 % for an increase of the voltage from 0.9 V to 2.4 V. For higher absorber voltages the pulsation starts to destroy a stable pulse train generation. The comparison of the results in Fig. 5.7 (b) with those in Fig. 5.8 (a) show, that it will not be possible to optimize the pulse generation by the M-MLL for a narrow pulse width Δt and a pulse train with a low noise simultaneously [71].

The pulse quality of the M-MLL was investigated using FROG measurements. The M-MLL was operated with a gain current $I_{gain} = 130$ mA and the absorber voltage was varied from $U_{abs} = 1.5$ V to 2.5 V. An almost linear blue chirp in the order of 100 GHz was measured over the pulse center, which could be compensated by about 10 m of SSMF. An increase of the absorber voltage U_{abs} from 1.5 V to 2.5 V leads to a wavelength shift to shorter wavelength but was accompanied by a spectral broadening. The FROG traces shows the reduction in temporal pulse width on expense of an increase of the spectral width. A good pulse quality was only be identified for absorber voltages up to $U_{abs} = 2.5$ V.

5.3.3 Locking Range, Repetition Frequency and Wavelength Tuning

A major challenge for the development of a M-MLL is a sufficient tunability of the pulse repetition frequency and the wavelength. A certain tunability is needed to compensate for repetition frequency and wavelength deviations caused by production tolerances of a M-MLL, e.g. to meet the ITU frequency standards. Simultaneously, the properties of the generated pulses, especially the noise performance has to be maintained. Fig. 5.9 shows the timing jitter for the tuning of the repetition frequency by the change of the external synchronization frequency. For a locking range of 175 MHz the timing jitter remained below 100 fs (the integration range was 100 Hz to 10 MHz).

Additional repetition frequency tuning of up to 500 MHz is possible by changing the gain current and absorber voltage simultaneously, similar to results in [56]. This tuning range can be further increased by carrier injection into the phase shift sections and by thermal phase shifting. Other publications [73] report on tuning ranges of up to 1 GHz.

The emission wavelength is determined by the periodicity of the DBR grating. Wavelength changes of about 5 nm towards lower wavelengths are possible by a current injection into this section. The change of the wavelength shows discrete steps rather than a continuous shift. The intermediate wavelengths can

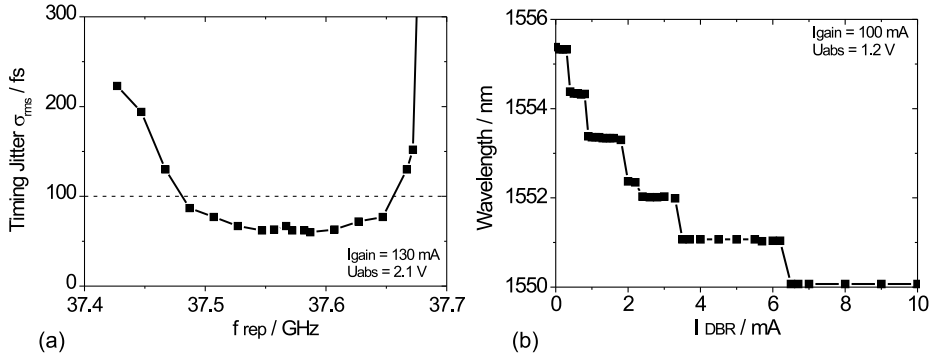

Figure 5.9: (a) Timing Jitter of a M-MLL for the variation of the synchronization frequency. (b) Tuning of the emission wavelength by current injection into the DBR section.

be attuned by an additional carrier injection into a phase section of the M-MLL (cf. also [74, 75]).

Unfortunately, the change of one parameter also affects the total performance. Therefore a readjustment of other operation parameters can become necessary.

5.4 Low Noise Pulse Generation with Mode-Locked Semiconductor Lasers

The importance of a low phase noise of pulse trains for high data rate OTDM applications was pointed out in chap. 1. An example is shown in sec. A.1. In the following sec. 5.4.1 the characteristics of the phase noise curves of MLL are considered in detail.

The main possibilities to reach low phase noise laser operation can be distinguish in 1^{st} a suitable choice of the parameters of the semiconductor laser material and the laser cavity set-up, 2^{nd} the choice of optimum laser operation conditions and 3^{rd} the noise reduction by a subsequent phase stabilization. The 1^{st} group comprises design features of the semiconductor material such as the introduction of an iron blocking layer in the semiconductor material as discussed in sec. 4.3 and an increase of the saturation energy, e.g. with the reduction of the number of quantum wells [76, 57]. Once the semiconductor material is grown only the set-up of the laser cavity can be changed. Here a high cavity quality helps to reduce the injection current and consequently also the amount of spontaneously emitted photons. For an increase of the cavity quality high reflection (HR-) coatings can be sputtered onto the facet of the cavity end. A further cavity parameter is the spectral filter bandwidth in the cavity as will be discussed in sec. 5.4.2. As a 2^{nd} step the choice of operation

conditions is important. This was discussed in the preceding sections of this chapter. In a third step subsequent methods for phase stabilization such as the application of feedback loops can be used. The last method suffers from the limited bandwidth of e.g. electrical loop setups. Especially the disturbing phase noise components in the high frequency range cannot be removed. The set-up of a laser operated with a feedback loop as discussed in appendix A.2.1 did not show an advantage in comparison to the precautions addressed in the first and the second place.

5.4.1 General Characteristics of the SSB Phase Noise Curves

In Fig. 5.10 the SSB phase noise curve of a EC-MLL as investigated in Sec. 5.1 is displayed for hybrid and passive mode-locking. For comparison the SSB phase noise curve of the RF synthesizer is shown. Three different regions A, B and C of the SSB-phase noise characteristics of the hybrid mode-locked laser are defined, which apply to all laser configurations investigated in sections 5.1 - 5.3.

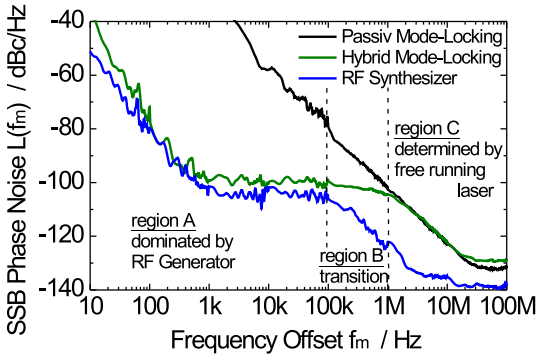

Figure 5.10: Characteristics of the single side band curves for a EC-MLL in passive mode-locking, hybrid mode-locking and the corresponding RF source for the active mode-locking part.

A strong dependence on the phase noise of the driving RF-generator is obtained for offset frequencies below 100 kHz (region A). On the other hand, for offset frequencies between 100 kHz and 1 MHz (region B), the phase noise behavior shows a transition from the phase noise of the RF-generator to that of the passively mode-locked laser. Above 1 MHz (region C) the SSB phase noise is clearly determined by the EC-MLL. In dependence on the RF coupling and the laser structure the frequency range of these regions show a slight variation [77].

Fig. 5.11 (a) shows the measurement of the SSB phase noise curve of the EC-MLL in dependence of the modulation power. Within the integration range between 100 Hz and 10 MHz, the timing jitter values have been measured down

to σ_{rms} = 120 fs at an RF-power of 25 dBm. This is close to the timing jitter of σ_{rms} = 105 fs of the RF oscillator used in these measurements. Most of the RF power is lost due to electrical mismatch between the laser diode and the connecting RF wires. The SSB phase noise curves shown in Fig. 5.11 (a) depend on the powers applied onto the bias-T. The signal RF power transferred to the chip is estimated taking into account the impedance mismatch between 50 Ω connection and the semiconductor laser chip with 5 Ω to about 20% of this value.

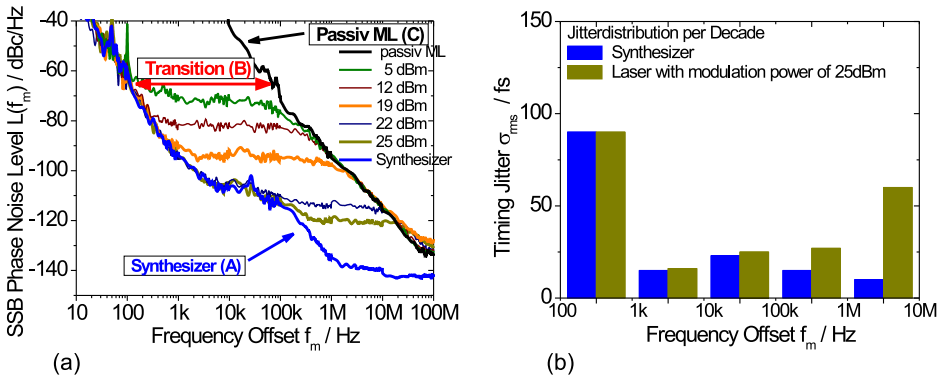

Figure 5.11: (a) This picture describes the influence of the driving power on the single side-band phase noise curves. The EC-MLL had a repetition frequency of 10 GHz. Fig. 5.11 (b) shows the reduction of timing jitter close to values of the synthesizer for maximum modulation power of 25 dB. The Jitter values for the lower and upper side-band are equal.

In Fig. 5.11 (a) the three regions (A-C) of the frequency offset can be identified as explained in Fig. 5.10. However these sections depend on the modulation strength. In the region A up to 100 kHz, the EC-MLL phase noise level can be reduced down to the oscillator phase noise level by hybrid mode-locking. In the region C (above 100 kHz for an RF power about 5 dBm and above 10 MHz for an RF power about 22 dBm) an increase of modulation power does not change the phase noise level. For this frequency offset the phase noise is determined by the passive mode-locking behavior. In the transition region B, the phase noise level can be further reduced by applying a higher modulation power. For a modulation power of 25 dBm the phase noise level is -120 dBc (Fig. 5.11 (a)).

Fig. 5.11 (b) shows the timing jitter evaluation for the RF power of 25 dBm. The integration over the frequency offset range according to eqn. 2.6 is subdivided into intervals for each offset decade and the jitter is calculated for these intervals. It reveals a high jitter contribution from low offset frequency components to the total jitter value. It is caused by the noise of the RF oscillator driving the laser and the evaluation limits of the electrical spectrum analyzer. Another contribution originates from high frequency offsets, where the laser does not follow the oscillator noise performance but shows additional, intrinsic

contributions to the phase noise.

The noise behavior shown in Fig. 5.11 could be identified for all mode-locked laser described in this chapter. Differences may occur for the exact position of the passive mode-locking according to the resonator quality and for the required RF modulation power due to the different RF coupling quality (cf. also sec. 5.2.3). This synchronization behavior is also observed for other laser types, e.g. DFB laser as discussed in [78].

5.4.2 Compromise Between Pulse Width and Timing Jitter Optimization

By the choice of the grating of the EC-MLL (cf. Fig. 4.1), it is possible to change the width of the generated pulses. For gratings with 150 lines/mm it was possible to generate 1.2 ps pulses but with a timing jitter of $\sigma_{RMS} = 190\ fs$. For gratings with smaller spectral bandwidth (e.g. 600 lines/mm) the pulse width increased to 3.2 ps while the timing jitter was reduced down to values of $\sigma_{rms} = 70\ fs$. Fig. 5.12 (a) shows this dependence for three different laser diodes. Similar results are discussed in [79].

Gratings with less lines/mm lead to a broader spectral filtering. Therefore the spectral width $\Delta\nu$ in eqn. 3.3 broadens and the temporal pulse width Δt becomes consequently shorter. However, this decrease of the temporal pulse width is accompanied by an increase of the timing jitter as Fig. 5.12 (a) shows. The timing jitter increases with an increase of the spectral width $\Delta\nu$, because a larger amount of spontaneously emitted photons are coupled into the cavity.

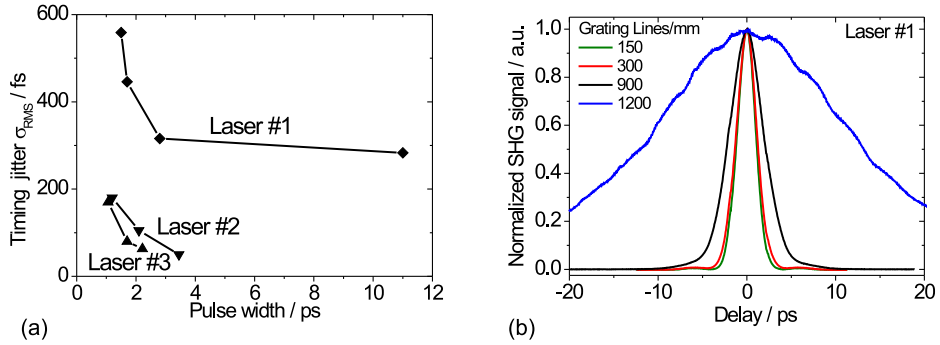

Figure 5.12: (a) Timing jitter versus pulse width for three different laser diodes. The change of the pulse width is obtained by the exchange of the gratings in each of the EC-MLL. (b) Pulse shape for laser #1 with different gratings.

On the other hand side gratings with a narrow filter bandwidth, i.e. more lines/mm, filter out more spontaneous emission. This is achieved on expense of a broader temporal pulse width. Furthermore, the spontaneous emission within the narrow filter bandwidth cannot be switched off. However, the temporal broader pulses experience a stronger retiming by the active modulation envelope

[28]. Therefore the influence of the remaining spontaneous emission onto the temporal pulse position in the cavity will be better suppressed.

The improvement of the timing jitter behavior of three different lasers is shown in Fig. 5.12. The lasers differ in the laser chip used and the modulation capability. All laser were semiconductor EC-MLL, thereof Laser #1 and #2 comprised a bulk laser diode with ion implanted saturable absorber and Laser #3 comprised a two section laser diode with a reversed biased absorber section. Laser #1 was operated at 5.5 GHz and the cavity end was defined by a grating with 150, 300, 900 and 1200 lines/mm. For the application of a grating with 150 lines/mm a strong increase in the timing jitter but no reduction of the pulse width was observed with respect to the results for the grating with 300 lines/mm grating. For a very narrow optical bandwidth filtering (1200 lines/mm) the spatial pulse width exceeds the absorber length and an effective mode-locking becomes impossible (Fig. 5.12 (b)). This defines the limits of the change of the spectral bandwidth. EC-MLL #2 and #3 were operated at a pulse repetition frequency of 10 GHz. The reduction of parasitic capacities within the laser diode improved the modulation bandwidth. Laser #2 was investigated in sec. 5.1. For the jitter measurement in dependence of the used grating it was operated using hybrid mode-locking. The gain current was chosen to 38 mA, which is close to the threshold current of this laser. Laser #3 was investigated in sec. 5.2. In this measurement the gain current was chosen to 90 mA and the absorber voltage to 2.0 V. For hybrid mode-locking the absorber was modulated. The pulse widths of laser #3 shown here are measured after the compensation of the pulse chirp.

Laser #2 and #3 represent the final timing jitter performance reached with the EC-MLL set-up in the frame of this work.

5.4.3 Low Noise, Short Pulse Generation

As discussed in the previous section, the generation of a low phase noise pulse train can be achieved by tighter spectral filtering within an external cavity MLL and by an increase in RF modulation depth. However, this leads to an increase of the pulse width, which is not suitable for optical time domain multiplexing up to 640 Gbit/s.

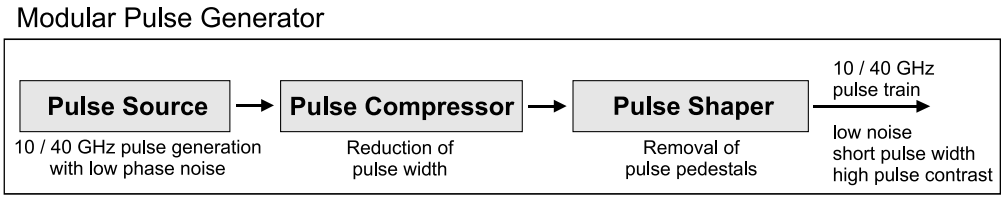

Figure 5.13: Schematic of the concept of an modular pulse generator to generate short pulses at a fundamental repetition frequency of 10 GHz or 40 GHz.

Therefore, a combination of low noise pulse generation and subsequent pulse compression is a promising way to meet the requirements for low jitter and short

pulse width simultaneously [11]. This leads to the modular set-up of a pulse generator as shown in Fig. 5.13: In the first step a pulse train with low phase noise is generated by narrow optical filtering inside the laser cavity. The second step is the reduction of the pulse width in a fiber based pulse compressor. This will be discussed in detail in the following chapter 6. In a third step a pulse shaper is used to remove the pulse pedestals. It increases the pulse to pedestal contrast as will be considered in Chap. 7.

Chapter 6

Pulse Compression

The typical pulse widths of semiconductor MLL and other pulse sources described in chapter 5 and 3 are in a range between 1.2 ps to 3.5 ps and a direct use for OTDM applications at multiples of 160 Gbit/s is not possible due to the coherent interference of the pulse slopes. As described in the last chapter the pulse generation with a mode-locked laser is a trade-off between a low noise performance and a short pulse width. Since a pulse compression is necessary in each case it is advantageous to optimize the pulse source for low noise and to accept a broad pulse width. The pulse width will be reduced in the next building block of the pulse generator, the pulse compressor. Different possibilities for a pulse compression exist and the selection of a method depends on the wavelength of the pulses. Fiber based pulse compression schemes are attractive because they avoid free space optics with high requirements on adjustment and low vibration. For communication applications the two most common techniques are adiabatic soliton compression using a dispersion decreasing fiber [80] and supercontinuum generation combined with a linear pulse chirping and spectral carving [81, 82].

6.1 Soliton Pulse Compression

Soliton formation is observed in the anomalous dispersion region of the optical fiber and it is described by the nonlinear Schroedinger equation [83]. A particular property of the soliton of the 1^{st} order (fundamental soliton) is the relation

$$P_0 = \frac{\mid \beta_2 \mid}{\gamma \cdot T_0^2} \tag{6.1}$$

between the peak power P_0, the pulse width T_0, the dispersion parameter β_2 and the nonlinear coefficient γ. Hereby the pulse width T_0 is related to the full width half maximum T_{FWHM} by $T_{FWHM} = 1.763 \cdot T_0$. The energy of a $sech^2$ pulse with the peak power P_0 is given by

$$E = 2 \cdot P_0 \cdot T_0 \tag{6.2}$$

cf. eqn. (B.12) in the appendix. From equation (6.1) it follows that the energy E of a soliton can be expressed as

$$E = 3.526 \frac{\mid \beta_2 \mid}{\gamma \cdot T_{FWHM}}.$$

If a soliton propagates over a lossless fiber (E=const) from the coordinates 0 to z, the relation between $T_{FWHM}(z)$ and $T_{FWHM}(0)$ is described by

$$T_{FWHM}(z) = \frac{\beta_2(z)}{\beta_2(0)} \frac{\gamma(0)}{\gamma(z)} \cdot T_{FWHM}(0) \tag{6.3}$$

which shows that a pulse compression can be reached by a decrease of $\beta_2(z)$ or by an increase of $\gamma(z)$ along the fiber. The formula 6.3 is strictly valid only for an adiabatic pulse change.

Fibers with a decreasing $\beta_2(z)$ along the fiber length have successfully been produced [84]. In this work soliton pulse compression is reached by various types of dispersion decreasing fiber, such as a simple dispersion decreasing fiber (DDF), dispersion flattened- dispersion decreasing fiber (DF-DDF) and highly nonlinear-dispersion decreasing fiber (HNL-DDF). A detailed overview over the fiber properties is given in Sec. B.1. For the dispersion decreasing fibers the pulse compression factor at the end of the fiber is expected to be equal to the ratio of the initial to the final second-order dispersion.

Different fiber profiles such as linear, gaussian, cosine, exponential and hyperbolic can be used. There is an ongoing discussion about the optimum dispersion profile for a fiber based soliton compression [85, 86]. However, an adequate choice is already made with a linear dispersion decreasing profile.

6.1.1 Pulse compression using simple DDF

The set-up for a soliton compressor using dispersion decreasing fiber is shown in Fig. 6.1.

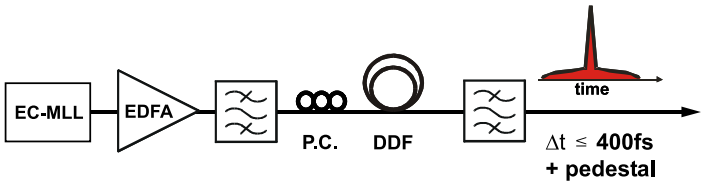

Figure 6.1: Set-up for a pulse compressor using dispersion decreasing fiber (DDF) for a reduction of the pulse width to $\Delta t \leq 400$ fs accompanied by the formation of a pulse pedestal.

The EC-MLL generates a 10 GHz pulse train with a pulse width of $T_{FWHM} = 3.2$ ps. The pulses are amplified and transmitted through a bandpass filter, a polarization controller and coupled into the dispersion decreasing fiber (DDF).

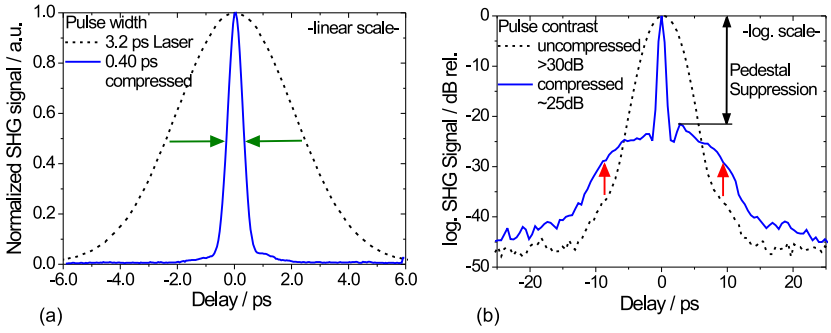

Figure 6.2: Pulse compression and pulse peak to pedestal contrast (Pedestal Suppression) before and behind a soliton compression stage setup by DDF, (a) on linear scale and (b) on logarithmic scale.

The length of the DDF is chosen to be 1000 m and the dispersion decreases linearly from 10 ps/nm/km to 0.5 ps/nm/km. Thus the expected compression ratio is 20 according to eqn. (6.3) if $\gamma(0)/\gamma(z) = 1$. The length was chosen to provide a slow gradual dispersion change for an adiabatic soliton compression. As described in [87], this gives the following condition for the length L

$$L > 335 \cdot T_0^2 \frac{m}{ps^2} \tag{6.4}$$

For a start pulse width of $T_{FWHM} = 3$ ps this yields L $\geq$ 970 m and is good in agreement to the experience made by the fiber manufacturer [88].

Behind the DDF the compressed pulses pass again a bandpass filter. Despite the attempt to achieve an adiabatic soliton compression, the output pulse usually comprises a narrow pulse and a pedestal due to an incomplete soliton formation. The pulse pedestals will cause coherent interferences if the 10 GHz pulse train is multiplexed to 160 Gbit/s or higher which inhibits an applications of the pulse train in error free data transmission. Fig. 6.2 shows the autocorrelation traces for a pulse width reduction reached with the soliton compression in the DDF.

For the evaluation of the pulse width the autocorrelation measurement is shown with the normalized SHG signal on a linear scale (a). The pulse pedestal can be recognized in the autocorrelation measurement with the SHG signal on a logarithmic scale (b). For the example shown, the pulse width was compressed from 3.25 ps to 0.4 ps while the pulse pedestal contrast was 25 dB after compression. The input power was 23 dBm.

A detailed investigation of the pulse compression was made. Fig. 6.3 shows measurements of the pulse width, the pedestal suppression, the spectral width and the spectral mode comb height versus the power $P_{IN\ DDF}$ into the DDF. The spectrum was broadened to a spectral width between 5 and 12 nm. For a high input power a shift of the wavelength maximum to higher wavelength was

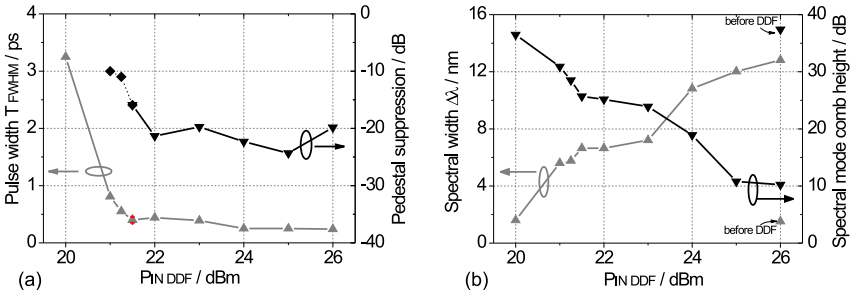

Figure 6.3: (a) pulse width T_{FWHM} and pulse pedestal suppression at the next 640 GHz bit position in dependence of the DDF input power. (b) spectral mode comb height and spectral 3 dB width of compressed pulses versus the DDF input power. The input wavelength was $\lambda = 1550$ nm. For comparison: For an EDFA output power of 26 dBm the spectral width was 1.5 nm and the spectral mode-comb height was 37.4 dB before the compression fiber. The pulse compression was measured without a bandpass filter behind the DDF.

observed. It is referred to a soliton self-frequency shift [89]. As shown in Fig. 6.3, the minimum optical average power to obtain temporal pulse compression was 21 dBm. The minimum pulse width of the compressed pulses was 0.25 ps for the set-up without a bandpass filter behind the DDF. This pulse width increased to 0.37 ps after a 13 nm bandpass filter which was inserted behind the DDF. The broadening is caused by a wavelength dependent differential group delay due to the filter passage. In a measurement of the differential group delay (DGD) this delay was determined to be ≤ 0.1 ps. A pulse pedestal was observed with a suppression of 20 dB.

An increase of the pulse power launched into the DDF caused a degradation of the optical mode comb spectrum of the compressed pulses. The increase of the EFDA amplification goes along with an increase of the amplified spontaneous emission (ASE). Especially ASE at the input pulse wavelength cannot be filtered by the 5 nm filter inserted between EDFA and DDF. The interaction between ASE and the solitons is taken responsible for the observed degradation [90].

The maximum input pulse width used was 3.25 ps and the minimum output pulse width obtained was 0.25 ps at a power of 25 dBm. Therefore, the experimentally observed compression factor is 13 while the value expected form the dispersion ratio $D_{in} = 10$ ps/nm/km to $D_{out} = 0.5$ ps/nm/km was 20. There are several reasons responsible for this difference: The dispersion tolerances are in the order of $\Delta D = 0.1$ ps/nm/km, about 20 % of the dispersion at the fiber end. A fiber dispersion of e.g. $D_{out} = 0.6$ ps/nm/km would already reduce the expected compression ratio to 16.7. Higher order dispersion, such as the dispersion slope, limits the pulse compression as discussed in [91]. Another effect, which reduces the experimental compression factor, is the power dissipation into pulse pedestals, which occurs during the soliton compression as shown in

Fig. 6.2 (b). This limits the compression of the soliton pulse in comparison to (eqn. 6.1). Also polarization mode dispersion (PMD) reduces the compression factor. A careful selection of the pulse polarization at the fiber input is necessary to minimize the effect of PMD. However, higher order polarization mode dispersion cannot be alleviated.

6.1.2 Pulse compression using DF-DDF

A limitation of the pulse compression is given by higher order chromatic dispersion [91]. Dispersion flattened DDF (DF-DDF) can be used for a pulse compression over a broader wavelength region. In consequence the spectral shape of the compressed pulses is more symmetric and a pulse compression down to a minimum pulse widths of T_{FWHM} = 0.19 ps was measured. The fiber had a linear dispersion profile from the anomalous dispersion region with D = 10 ps/nm/km into the normal dispersion region with D = -1.0 ps/nm/km at the output end[1] in order to enlarge the spectral broadening as suggested in [92].

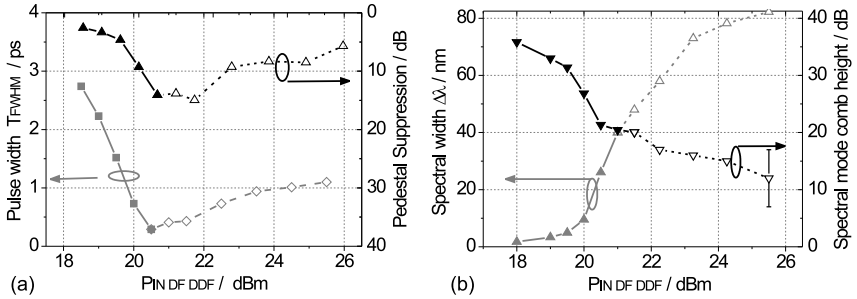

Figure 6.4: (a) temporal pulse width T_{FWHM} and the pulse to pedestal contrast versus the pulse input power. (b) spectral pulse width and spectral mode comb height versus the input power into the DF-DDF compressor. The input wavelength was $\lambda = 1550$ nm. For higher input powers a pulse slitting was observed.

In Fig. 6.4 (a) the change of the pulse width for an increase of the pulse input power from 18.0 to 20.5 dBm is shown. The original pulse train had a repetition frequency of 10 GHz and the pulses a width of 3.5 ps. In this measurement the pulse width was reduced to 0.27 ps. A draw back of this method is the pulse instability for higher input pulse powers. For high pulse powers exceeding 20.5 dBm a strong deviation from a sech shaped spectrum was observed. Simultaneously the autocorrelation measurement of the compressed pulse showed a split up in the pulse peak. The compressed pulses pass a region

[1]The dispersion slope changes from S $\approx$ 0.20 ps/nm^2/km for D = 10 ps/nm/km to S $\approx$ -0.05 ps/nm^2/km for D = -2 ps/nm/km at a wavelength of $\lambda = 1550$ nm. At the output end of the DF-DDF used the in these experiments, S lies in the proximity of 0 ps/nm^2/km according to the dispersion map provided by the fiber manufacturer

of zero dispersion before they are broadened in the final normal dispersion end of the DF-DDF. The observed pulse distortions are considered as a consequence of a higher order soliton formation in the vicinity to the zero dispersion. In Fig. 6.4 (b) the spectral broadening and the spectral mode comb height is shown in dependence of the input power. A wide spectral pulse broadening is achieved on expense of the quality of the optical spectrum. The mode comb height is continuously reduced if the input power was increased over 20.5 dBm.

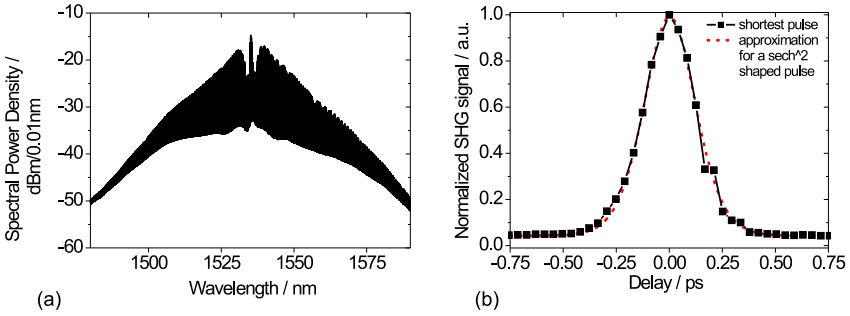

Figure 6.5: (a) an optical pulse spectrum, (b) an autocorrelation measurement for the minimum T_{FWHM} of 0.19 ps after the compression in DF-DDF.

Fig. 6.5 (a) shows the spectrum for the optimum input power of 20.5 dBm and Fig. 6.5 (b) shows the measured autocorrelation trace for the shortest pulse width of 0.19 ps (FWHM). The curves were taken without spectral bandpass filter behind the DF-DDF. A pulse compression with symmetric spectrum is characteristic for a dispersion flattened fiber and was measured for the wavelengths of the entire C-Band.

For an enlarged and stable pulse spectrum, a DF-DDF with a dispersion (e.g. D = 10 ps/nm/km to D = -1 ps/nm/km) is suitable only in a small power range as shown in Fig. 6.4 (a). Instead a combination of DF-DDF in the anomalous dispersion region only followed by a highly nonlinear fiber with a normal dispersion region is considered here for further investigations.

6.1.3 Pulse compression using HNL-DDF

In order to reduce the power requirements for a higher base frequency at the pulse compressor, e.g. 40 GHz instead of 10 GHz, a reduction of the pulse peak power is necessary. A practical reason is the limited power available by the EDFAs. The peak power for a soliton formation and compression can be reduced by an increase of the nonlinearity of the fiber. A HNL-DDF, also with a linear decreasing fiber dispersion from D = 12 ps nm^{-1} km^{-1} to 0.5 ps nm^{-1} km^{-1} along a length of l = 920 m was used to compress a 40 GHz pulse train generated with a M-MLL pulse source as described in Section 5.3. For a reduction of the required soliton peak power (cf. eqn. 6.1) this fiber had an increased fiber nonlinearity coefficient of γ = 9 $W^{-1}km^{-1}$ in average while the typical fiber

nonlinearity of the DDF used in the measurements described in the previous sections was about $\gamma = 3$ W^{-1}km^{-1}. A gradual change of the fiber dispersion profile is necessary to obtain the linear decreasing dispersion along the fiber. At the same time the value of γ changes rather than remaining on a constant value. Since the effective area A_{eff} of a DDF decreases the value of γ increases. It is also possible to consider the DDF as fiber with increasing nonlinearity. However, the nonlinearity coefficient $\gamma \sim \frac{1}{A_{eff}}$ only changes with a small factor compared to the change of dispersion D with factor 1/24 [88], cf. Tab. B.1.

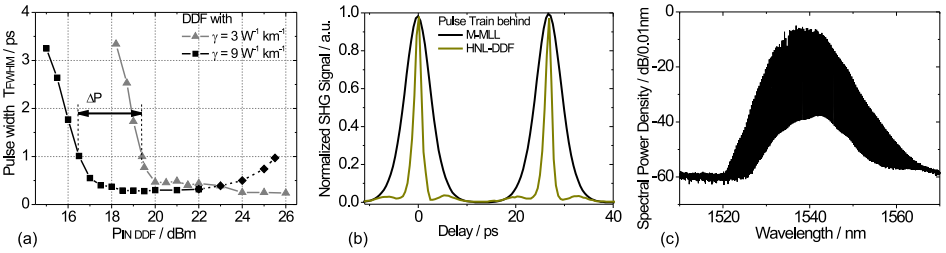

Figure 6.6: (a) Pulse width T_{FWHM} versus average input power of a 10 GHz pulse train into DDF and HNL-DDF. (b) Temporal pulse width of a 37.6 GHz pulse train of the M-MML before and after compression in HNL-DDF and (c) spectral shape of compressed pulses behind the HNL-DDF.

In Fig. 6.6 (a) the required average pulse power for a 10 GHz pulse train for a DDF with a $\gamma = 3$ W^{-1}km^{-1} is compared to the HNL-DDF with $\gamma = 9$ W^{-1}km^{-1}. A pulse compression has been reached for an input power which was about 3 dB lower than that for the conventional DDF. The expected power difference of 4.8 dB (cf. eqn. (6.1)) due to the change of γ is reduced by higher splicing losses between SSMF and HNLF. For input powers of 20 dBm and higher the compression effect saturates and in case of the compression with HNL-DDF the formation of a pulse pair has been observed. This is considered as an higher order soliton effect, which appears if the length of the HNL-DDF does not coincide with the soliton period $z_0 = \frac{\pi}{2}\frac{T_0^2}{|\beta_2|}$ or an multiple thereof.

The reduction of the required pulse peak power for a soliton pulse compression enables the use of a commercially available high power EDFA for pulse compression at 40 GHz. The 37.6 GHz pulse train of the M-MLL was compressed in HNL-DDF. Fig. 6.6 (b) shows the autocorrelation trace of two adjacent pulses before and after compression. In Fig. 6.6 (c) the optical spectrum is shown after the pulse compression in HNL-DDF. The spectral mode comb of the compressed pulse train had a height of 35 dB. The pulse width was reduced from 3.75 ps to 0.365 ps. The average input power of the pulse train was as low as 22.8 dBm.

The higher value of the nonlinearity coefficient γ reduces the required pulse amplification and therefore enables a soliton pulse compression at 40 GHz. It also reduces the disturbing effects of ASE due to a high power amplification.

6.2 Pulse Compression using Supercontinuum Generation

The process of spectral broadening and pulse compression comprises several effects, such as self phase modulation (SPM), cross phase modulation (XPM) and four wave mixing (FWM). It has to be distinguished between the conditions, either for the most efficient spectral broadening, which is often considered in this context, or the spectral broadening with the aim of pulse compression, which also obeys all pulse criterions considered in chap. 1. For pulse compression the HNLF is followed by a piece of SSMF to compensate for the chirp of the broadened pulse spectrum. A linear blue-chirp can be reached if the dispersion along the HNLF is kept in the normal dispersion region. Then the self phase modulation is considered as the main effect for the spectral broadening [82] while disturbing effects, such as modulation instabilities and soliton formation do not interplay [83].

Experimental Results

The set-up for pulse compression using supercontinuum generation with HNLF is depicted in Fig. 6.7. The fiber properties of the HNLF are listed in Sec. B.1. In difference to the set-up used for a soliton pulse compression with DDF, here an additional chirp compensation behind the HNLF is necessary. The chirp is induced during the pulse broadening in the HNLF and its amount also depends on the input power. It can be compensated by transmission through a short length of SSMF as long as only a linear chirp is induced. For a significant change (e.g. 2.5 dB in Fig. 6.10) of the pulse input power into the HNLF the SSMF length for chirp compensation had to be readapted. Pulses with a higher peak power experience a wider spectral broadening but smaller chirp during the transmission through the HNLF (cf. [81]). Therefore length of SSMF required for the subsequent pulse compression by opposite dispersion is reduced. Typical SSMF fiber length, required for chirp compensation varied between 20 and 40 m. A length of 10 m is already required for the fiber connection between the HNLF end and the free-space michelson set-up of the autocorrelator.

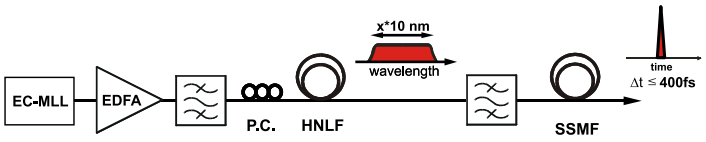

Figure 6.7: Set-up for pulse compression using supercontinuum generation in a highly nonlinear fiber (HNLF). The pulse widths are reduced to values of $\Delta t \leq 0.4$ ps after a chirp compensation by transmission through x·10 m meters of SSMF. For investigation of the compressed pulse spectra the second filter is omitted. Otherwise, for a further application of the compressed pulses, a selection of the wavelength is often required.

In the experiment, depicted in Fig. 6.7, an EC-MLL generated a 10 GHz pulse train with a pulse width of 1.8 ps. The pulses were amplified and transmitted through a bandpass filter and a polarization controller before they were launched into the HNLF1 (cf. Sec. B.1). The HNLF1 had a length of 510 m and a nonlinear coefficient $\gamma = 21$ W^{-1} km^{-1}. In the measurement using the HNLF1 the spectrally broadened pulses pass a bandpass filter to cut off evanescent pulse tails.

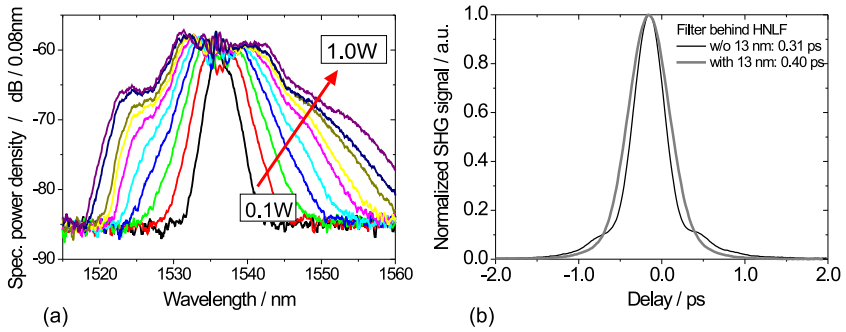

Figure 6.8: (a) Broadening of the optical pulse spectrum in the highly non-linear fiber HNLF1 for different input power P_{avg}, (b) autocorrelation traces of a pulse without and with spectral filtering.

The spectral pulse broadening in a highly nonlinear fiber induces a chirp, which depends on the input power of the pulses. For an average input power of 1 W the chirp was compensated by a pulse transmission through 20 m of SSMF (0.34 ps/nm). The HNLF1 ($\lambda_0 = 1569$ nm) was used in the normal dispersion regime with a low dispersion in order to maintain the high pulse peak power over a longer fiber length. Fig. 6.8 (a) shows the optical spectra measured behind the HNLF1 for an average pulse power launched into the compression stage varying from 100 mW to 1 W in steps of 100 mW. The input pulse wavelength was 1537 nm, and the dispersion was D = -1.0 ps/nm/km. The fiber dispersion slope $S_{1550nm} = 0.03$ ps / nm^2 / km caused the observed asymmetries in the optical spectra (cf. another example in Fig. 6.9 (d)). A general possibility to reduce the disturbing effect of higher order dispersion is the reduction of the fiber length. In turn, an increase of the pulse power is required for the compression (cf. also Fig. 6.11). The available amplification limits the reduction of the fiber length.

Fig. 6.8 (b) shows the autocorrelation trace of a compressed pulse before and behind the 13 nm bandpass filter for an average input power of 1 W. The compressed pulses had a spectral width of 19 nm and 12 nm and a temporal pulse width of 310 fs and 400 fs, respectively. The insertion of the bandpass filter increased the temporal pulse width but provided also a better pulse pedestal suppression. A limitation arises from the PMD of the HNLF (cf. Fig. 6.13 (b)) and the bandpass filter with a measured DGD of ≤ 0.1 ps.

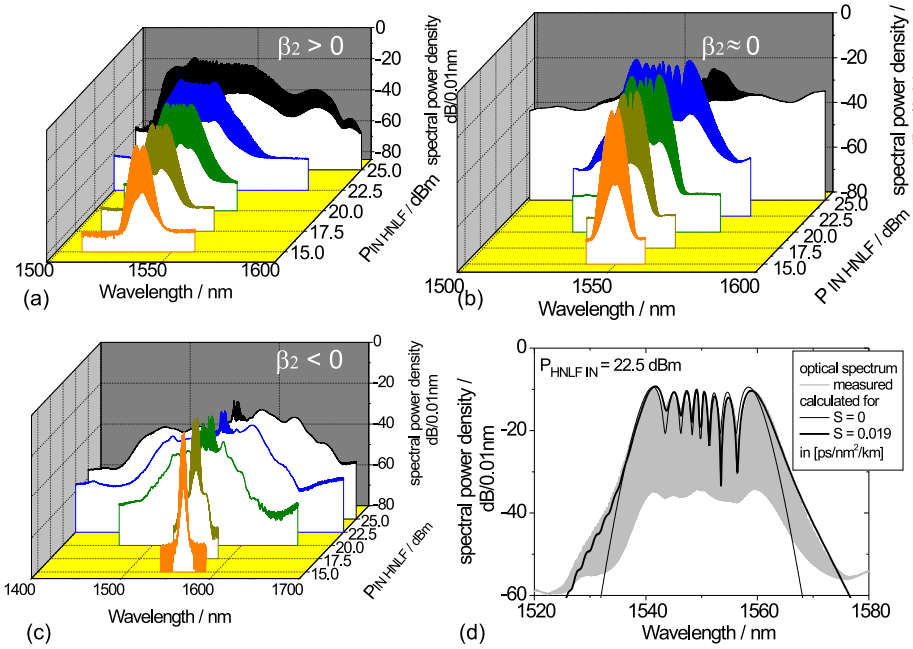

Figure 6.9: Supercontinuum generation in dependence of the input wavelength launched into the HNLF2 with $\lambda_0 = 1555$ nm. The wavelength of the input pulses was chosen (a) in the normal, (b) in the normal close to zero and (c) in the anomalous dispersion region. In (d) the measured optical spectrum for an input power of 22.5 dBm at $\lambda = 1550$ nm (as in case (b)) is compared with calculations of the spectral envelope with D = -0.09 ps/nm/km without and with a dispersion slope of S = 0.019 ps/nm^2/km. Calculated curves shown in (d) by courtesy of Ayhan Demiran, WIAS Berlin.

The investigation of the optimum fiber dispersion for pulse compression by supercontinuum was made using HNLF2. This fiber has a length of 789 m, a nonlinearity of $\gamma = 10.5$ W^{-1}km^{-1} and a zero dispersion wavelength of $\lambda_0 = 1555$ nm. The wavelength of the pulse source was tuned to achieve the pulse compression for the three cases of the normal dispersion ($\beta_2 > 0$) at 1535 nm, low dispersion ($\beta_2 \approx 0$) at 1550 nm and anomalous dispersion ($\beta_2 < 0$) at 1562 nm. The pulse width of the input pulses where 3.2 ps and the pulse repetition frequency 10 GHz.

The broadening of the optical pulse spectra is shown in Fig. 6.9 in dependence of the HNLF2 input power. In the regime of anomalous dispersion the spectral pulse broadening exceeds a width of 100 nm, but the mode-comb structure is strongly reduced (Fig. 6.9 (c)). In case of a low dispersion ($\beta_2 \approx 0$) the generation of new spectral components by SPM is more efficient (Fig. 6.9 (b)). Simultaneously the disturbing effect of higher order dispersion becomes more distinctive as seen in (d) by the power fluctuations within the pulse spectrum. The calculated pulse envelopes are symmetric if the dispersion slope equals zero

but becomes asymmetric for, in this case, slope values of S = 0.019 ps/nm^2/km. For high input powers spectral components reach into both adjacent dispersion regions and lead to an onset of coherence degradation as known from the situation in the anomalous dispersion region.

Only in the normal dispersion region, shown in Fig. 6.9 (a), the maintenance of a mode comb structure with increasing input power was possible. The maximum spectral pulse width for an input power of 25 dBm was 30 nm. This relatively small supercontinuum (cf. e.g. [93, 94]) provides a spectral width, which is more than sufficient for a pulse compression to below 0.4 ps (Fig. B.1). This situation is considered in more detail in Fig. 6.10.

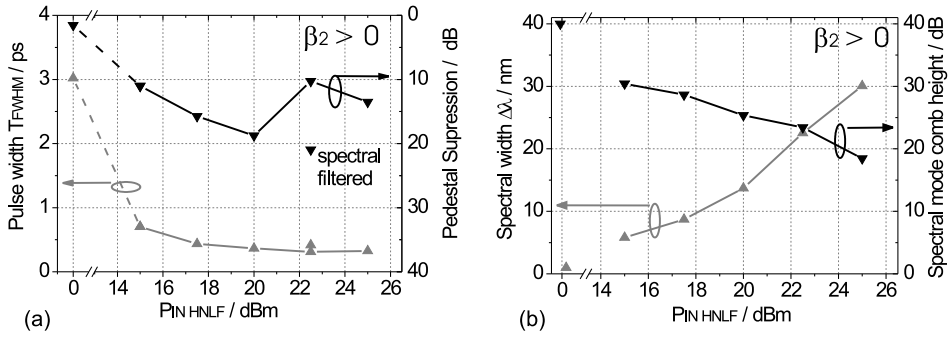

Figure 6.10: Evaluation (a) of the pulse width $\Delta t = T_{FWHM}$ after chirp compensation and (b) of the mode comb height versus the HNLF2 input power. The improvement of the pedestal suppression by spectral filtering is shown exemplarily in (a) for an input power of 22.5 dBm. Simultaneously a slight pulse broadening is inevitable.

Fig. 6.10 (a) shows the pulse width and the pulse to pedestal contrast versus the pulse input power. Fig. 6.10 (b) shows the spectral width and the mode-comb height versus the pulse input power into the HNLF2. These results were measured for an input wavelength in the normal dispersion region of the HNLF2 ($\lambda < \lambda_0$).

In Fig. 6.10 (a) a limitation of the pulse compression can be observed for an increase of the input power over 18 dBm. The generation of new spectral components in the normal dispersion region is accompanied by a temporal broadening of the pulses. In consequence the pulse peak power is reduced and the pulse shape changed from parabolic to rectangular shape. The induced chirp, suitable to compress the pulse, is limited to the edges of the pulse spectrum [83]. In consequence the nonlinear effects to enhance the spectral width by SPM saturate. Fig. 6.10 (b) shows the increase of the spectral width. This is accompanied with a reduction of the mode comb structure, e.g. due to the increase of the EDFA noise and the distribution of the pulse energy over a broader spectral range.

Dependence from the HNL fiber length

Fig. 6.11 (a) shows the evolution of the pulse width after a chirp compensation with SSMF in dependence of the HNLF fiber length and the input power. For these measurements the dispersion flattened HNLF 3, 4, 5 and 6 (cf. Appendix B.1) were used. The dispersion D was (-0.5 ± 0.1) ps/nm/km in order to provide a sufficient distance to the zero dispersion over the C-band and the fiber length despite unavoidable fabrication tolerances.

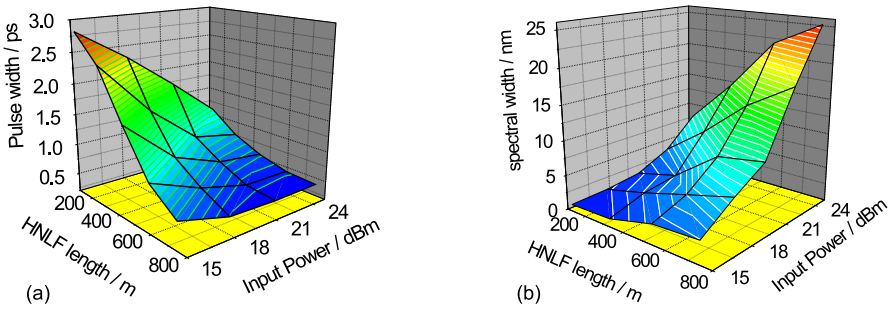

Figure 6.11: (a) pulse width over HNLF fiber length and input power, (b) spectral width over HNLF fiber length and input power. For a high fiber input power and a fiber length exceeding 500 m the pulse width reduction saturates while the spectral width continues to increase.

The color graded pulse width diagram shows the requirements on fiber length and input pulse power for the maximum available pulse width reduction. For high fiber input power and fiber length exceeding 500 m the pulse width reduction saturates while the spectral width continues to increase. The time-bandwidth product increases from the transform limit of sech pulses for short fiber length and low powers up to four times for maximum power and fiber length at right hand corner of the diagram. A spectral broadening towards this point is a prerequisite for wavelength conversion rather than pulse compression. For the latter case higher input power should be avoided in order to preserve the spectral mode comb height, as shown in Fig. 6.10. Furthermore simulations for dispersion flattened fiber with a dispersion D $\sim$ -0.5 ps/nm/km indicate a tendency to optical wave-braking [95]. The combination of a lower pulse power and a longer fiber length helps to avoid this effect.

6.3 Comparison of pulse compression methods and limitations

The pulse compression results for the three representative fibers HNLF2, DDF and HNL-DDF are summarized in Table 6.1. The combination of soliton

compression in the anomalous dispersion region with an increased fiber nonlinearity significantly reduced the power requirements for pulse compression. Soliton based fiber compressor can be subject to additional noise, e.g. caused by Gordon-Haus-Jitter [96]. However, in the frame of this work only a minor increase of the timing jitter was observed (cf. Fig. 7.4). In general the pulse compression with supercontinuum is reached with shorter fiber length. Apart from these differences the obtained pulse properties such as pulse width, pulse to pedestal contrast and mode comb height do not suggest the one or the other method to be advantageous.

Method / Fiber type	Fiber length / m	Pulse width after compression / ps	Peak to pedestal/slope contrast / dB	Mode comb height / dB	Input power / dBm	Spectral width / nm
Solit. compr. DDF	1000	0.25	24.3	10.8	25	12.2
		0.40	15.9	25.7	21.5	6.7
Solit. compr. HNL-DDF[1]	920	0.27	20.1	20.1	21.5	17.6
		0.40	24.2	23.1	17.5	11.6
SC gener. HNLF2	789	0.31	10.3	18.4	25	30.0
		0.44	15.7	28.7	17.5	8.7

Table 6.1: Evaluation of the three main types of fiber for pulse compression: DDF, HNL-DDF and HNLF. The results are shown for the generation of 0.4 ps pulses and for the minimum possible pulse width. The peak to pedestal contrast is determined by the height of the autocorrelation function of the pulse slope or, if worse, the formation of a pulse pedestal. The slope height is measured at the next 640 GHz bit position in a distance of 1.5625 ps from the pulse peak. For comparison: In an autocorrelation measurement a sech^2 pulse with a FWHM of 0.4 ps is decreased by 20.0 dB in a distance of 1.5625 ps from its maximum. The average power of a 10 GHz N=1 soliton sequence in SSMF is equal to 31.6 dBm (1.45 W).

The pulse width reduction is limited and the filtering of a part of the spectrum leads to a slight increase of the final pulse width to values between 0.40 ps and 0.50 ps. In the following some aspects of the pulse compression limits are discussed.

Phase coherence of the pulse train

Data formats such as differential phase shift keying (DPSK) require a well-defined phase of the optical carrier (optical field) between adjacent pulses. The

[1] measured with a pulse repetition frequency of $f_{rep} = 10$ GHz

maintenance of the mode-comb structure is an indication for the preservation of coherent phase relations in optical pulse trains. In particular deviations in the carrier phase and therefore in the phase coherence of the pulse train, cause a line width broadening in the optical spectrum [10]. In section 8.3 an error free DPSK 640 Gb/s back-to-back measurement is demonstrated and proofs the maintenance of a stable phase between adjacent pulses in the pulse compressor and for the pedestal reduction.

EDFA Noise

The pulse sources considered in Chap. 3 generate pulse trains with pulse peak powers which are not sufficient to stimulate the required nonlinear effects in the available fibers (DDF and HNLF) for the pulse compression. In consequence there is the need for a high power amplification which inevitable adds noise to the pulse trains. Fig. 6.12 (a) shows the mode-comb spectrum of a 1.5 ps 10 GHz pulse train after a spectral broadening in HNLF2. Therefore the pulse train is generated in a solid state MLL and amplified to $P_{avg} = 21$ dBm. In order to evaluate the influence of the amplifier, the EDFA input power was reduced from 9.2 dBm to -17.5 dBm by a manual attenuator. The EDFA output power was kept at 21 dBm, a typical average power needed for the compression of a 10 GHz pulse train.

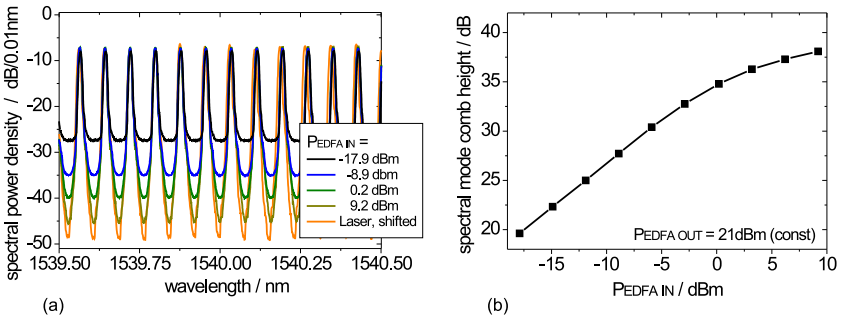

Figure 6.12: (a) The optical spectrum of a pulse compressed in HNLF2. The input power into the EDFA was varied. (b) the mode-comb height in dependence of the optical EDFA input power. The resolution bandwidth was 0.01 nm.

Fig. 6.12 (b) shows the reduction of the mode-comb height after the pulse compression in HNLF2 in dependence of the EDFA input power. The mode comb height of the laser spectrum is gradually reduced from 38.1 dB to 19.6 dB behind the HNLF2 if the EDFA input power was attenuated. The mode comb height of the laser spectrum without amplification was as high as 41.3 dB.

The degradation of the optical mode-comb spectrum has to be distinguished between underlying white noise components which form a noise floor and the phase deviations which cause a line width broadening. Here the observed reduction of the spectral mode-comb height is caused by the increase of the noise floor.

A problem for further applications are very low pulse powers. In Fig. 6.12 (a) a noise floor becomes apparent if the signal input power of a 1.5 ps 10 GHz pulse train into the EDFA becomes lower. In this case the amplification to the constant output power of 21 dBm requires a higher EDFA gain and simultaneously increases the noise figure of the EDFA.

PMD

For pulses launched into a fiber compressor a controlled input polarization is necessary for an optimum pulse width reduction. The fibers used for the pulse compression have remaining PMD values in the order of 0.5 $ps/\sqrt{km}$. Especially HNLF fibers often have a higher PMD value. The input polarization plane of a pulse train has to be aligned parallel with one of the main polarization axis of a compressor fiber. It avoids the pulse splitting into separate short pulses travelling along the fast or slow fiber axis which eventually recombine and lead to a broader final pulse width. With an alignment parallel to one polarization axis it is possible to reduce the influence of the first order PMD. However, the higher order fiber PMD as measured over the wavelengths of the C-Band in Fig. 6.13 cannot be alleviated by an alignment of the polarization axis. The change of the differential group delay is especially critical for pulses with a broad spectrum, i.e. short pulses, and limits the possible pulse compression. The evaluation of the differential group delay (DGD) showed a similar course if the measurement was repeated at different times. Due to the short fiber lengths of $\leq$ 1 km a change of the distribution of the DGD versus the wavelength is not observed.

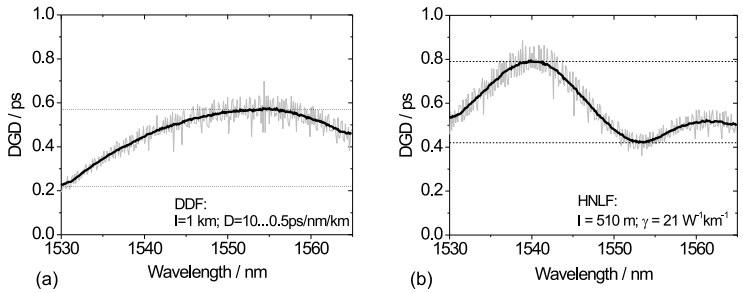

Figure 6.13: PMD evaluation: Differential group delay measurement for (a) the DDF and (b) HNLF1 over the C- band. These fibers were used for the pulse compression as displayed in Fig. 6.3 and Fig. 6.8.

An alternative is the use of polarization maintaining DF-DDF as used in [97] for 54 fs 10 GHz soliton generation and in [98], where a 2.3 ps 40 GHz pulse train of a mode-locked laser diode was compressed to 100 fs.

Higher order dispersion

The pulse compression based on soliton effects has not reached the expected theoretical pulse width. For the simple DDF a pulse compression factor of 20 was expected according to the fiber dispersion decreasing from D = 10 ps/nm/km at the fiber input to D = 0.5 ps/nm/km at the fiber output. A part of the EDFA power is lost due to amplified spontaneous emission and due to pulse broadening by PMD effects. Additionally a soliton self-frequency shift was observed for high input powers. The spectral pulse maximum was shifted by about 10 nm to longer wavelength. In combination with third order fiber dispersion in the order of S = 0.02 ps/nm^2/km, the effective dispersion at the end of the fiber increased to D = 0.6 ps/km/nm and reduced the expected compression factor to 16.7 . For dispersion flattened DDF this effect has smaller influence due to the reduced slope of the order of S $\sim$ 0.005 ps/nm^2/km.

6.4 Alternative types of fiber based pulse compression

A broad range of fiber types has been investigated elsewhere for pulse compression. They can be considered as an alternative or supplement to the methods investigated in the preceding chapter.

For very broad pulses exceeding pulse widths of 10 ps, e.g. generated with a cw-laser - modulator combinations, a consecutive set-up of two DDF compression fiber with an intermediate pedestal suppression stage is proposed to compress pulses to below 300 fs [99].

Despite the high pulse peak power requirements a pulse compression with N>1 solitons is an attractive choice for pulse compression, especially for lower data rates and is investigated in [86]. A possibility to circumvent the high pulse powers is the use of low dispersive fiber such as DSF which were used to compress pulses from 5 ps to 1.5 ps for 160 Gbit/s OTDM applications [100]. The continuous dispersion decreasing profile of DDFs can be approximated by Step Like Dispersion Profiled Fiber (SDPF) or Comb Like Dispersion Profiled Fiber (CDPF). The fibers used for the separate sections of a SDPF or CDPF are commercially available fiber types such as DSF and SSMF. SDPF stages have been used to compress pulses to a final pulse width of 500-700 fs [101] or even to the sub-100 fs region [102]. CDPF pulse compressors were constructed with different fiber combinations such as DSF and SSMF to compress sinusoidal pulses to 3 ps [103] or 11.5 ps pulses to 538 fs [104]. Alternatively HNL-DSF and SSMF were used for the compression of a 104 GHz pulse train to a pulse width of 328 fs [105]. The use of HNL-DSF reduces the required length of the compression stage to 693.6 m.

In addition, the recent development of micro structured fibers (also known as photonic crystal fibers) offers a possibility to increase the light confinement in the fiber core and therefore the nonlinearity. The pulse compression can be achieved along a shorter fiber length. This is attractive since thermal phase deviations induced in each fiber based pulse transmission scale with the length

of the fiber. In a data transmitter a shorter compression fiber can help to reduce the fiber length between pulse source and data modulator. Therefore the variations of the temporal pulse position with respect to the transmitter clock are reduced. Such an improvement could save an additional clock extraction unit behind the pulse compressor, overwise required to realign the modulator switching window (cf. Transmitter (Tx) set-up in Fig. 8.6, sec. 8.3).

Chapter 7

Pedestal Suppression

The reduction of the pulse width is often accompanied by the formation of pulse pedestals. These pedestals cause a degradation of the data signal and have to be removed by e.g. a loop mirror or simply by wavelength conversion if the required spectral width is available. A number of investigations made elsewhere, e.g. [91, 100, 106, 107], used the nonlinear switching behavior of fiber ring configurations. This approach will be investigated in more detail in the following section 7.1.

Another possibility to remove the pulse pedestals is the use of a wavelength conversion following a spectral broadening which will be considered in section 7.3. A further method, not considered here, is the pulse shaping incorporating an EAM. This method follows the idea of the pulse generation by modulating an cw- light signal (cf. sec. 3.3). It is not appropriate for pulses with a pulse width < 1 ps.

The optimum set-up has to be selected according to parameters such as the properties of the available fibers, the pulse repetition frequency, the available amplifier power and the available wavelength range.

7.1 Pedestal reduction by a dispersion imbalanced loop mirror (DILM)

A particular set-up for pedestal reduction is shown in Fig. 7.1. The incoming pulses are split by a fiber coupler to provide a pair of pulses which propagate in opposite directions through the loop.

The pulse pair introduced into a fiber loop experiences a nonlinear switching if a π phase shift is obtained between both pulse parts, which propagate in opposite directions through the loop. If a loop pulse pair reaches the fiber coupler after a circulation with a π phase shift or an uneven multiple of π it recombines and is switched to the output port while pulse pairs without or an even multiple of the phase shift π are switched back to the input port. The important feature for the nonlinear switching with a fiber loop is the introduction of an asymmetry, which influences the pulse peaks but not the pulse pedestals. Several configurations of fiber loops were investigated for the pedestal removal. There are different possibilities to insert an asymmetry in

the fiber loop

- a fiber loop set-up with an attenuator at an asymmetric position within the DSF loop [108]
- a fiber loop set-up with an amplification at an asymmetric position within the loop [109].
- a NOLM with an asymmetric coupler [110].
- A dispersion imbalanced loop by use of a DSF-SMF fiber combination [111, 112]

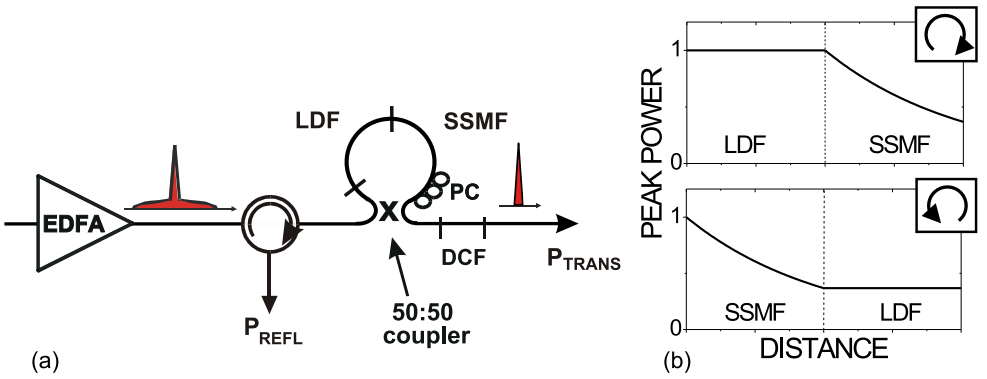

Figure 7.1: (a) set-up of the dispersion imbalanced loop mirror (DILM) comprising low dispersive fiber (LDF) and standard single mode fiber (SSMF), (b) changes of the pulse peak power circulating either in clockwise or in counter clockwise direction.

The principal difference between the listed concepts is the way in which the asymmetry for the pulse switching effect is reached: The first three examples rely on the concept of an asymmetric pulse power distribution between both pulses propagating in opposite directions through the fiber loop. The asymmetric power distribution is required for the switching effect. However, a strong coupler asymmetry reduces the difference between the transmission maximum and minimum of the loop mirror [106] and therefore limits the possible pedestal reduction. The proposed NOLM set-up with an attenuator leads to an enhanced inherent power loss while a NOLM set-up with an amplifier within the loop, e.g. an EDFA, is susceptible to an increased time dependent polarization change within the loop.

The concept of the dispersion imbalance (forth item) utilizes the influence of the different fiber dispersions. It leads to a different pulse width and peak power for both pulses propagating through the loop while both pulses have the same pulse energy.

7.1.1 Operation principle of a DILM

Here the calculation of the phase shift to achieve the switching effect is considered. The switching behavior of a fiber loop mirror is described by the formula [107]

$$P_{trans} = P_{in} \cdot \frac{1}{2}(1 - \cos(\Delta\phi)) \tag{7.1}$$

with $\Delta\phi$ the experienced phase difference for counter propagating pulses after the circulation through the loop. The phase difference $\Delta\phi$ for the loop pulse propagation in the DILM is calculated for clockwise (cw) and counter clockwise (ccw) propagation by:

$$\Delta\phi = \phi_{cw} - \phi_{ccw} \text{ with} \tag{7.2}$$
$$\phi_{cw} = \phi_{LDF} + \phi_{NL\ LDF} + \phi_{SSMF} \tag{7.3}$$
$$\phi_{ccw} = \phi_{LDF} + \phi_{SMF} \tag{7.4}$$

were LDF is a low dispersion fiber, e.g. DSF, and were ϕ_{cw} and ϕ_{ccw} are the accumulated phases of the clockwise and counter clockwise propagating pulses, respectively. The difference is the nonlinear phase shift $\phi_{NL\ LDF}$, which is induced due to the preserved peak power of the unchanged clockwise propagating pulse. The peak power is maintained due to the small dispersion of the low dispersion fiber (in our case DSF) section.

Counter propagating pulse components with low power do not experience a relative phase shift with respect to each other and have accumulated the same phase $\phi_{cw} = \phi_{ccw}$ after the circulation. For these components $P_{trans} = 0$.

For pulse peaks with high power the clockwise circulation comprises the additional phase shift $\phi_{NL\ LDF}$ along L_{LDF}. Hereby the formation of a fundamental soliton (N = 1) is attractive, as only in this case the nonlinear phase shift applies for the complete sech^2 shaped soliton and therefore maintains the pulse shape [113]. Counter propagating pulses have a lower pulse peak and will not experience a significant nonlinear phase shift.

A clockwise propagating pulse with a peak power below soliton peak power experiences a phase shift according to the power which varies over the pulse. For the calculation of the required DILM input power only pulses, which satisfy the soliton condition and experiences the same phase shift for all parts of the pulse, are considered.

ϕ_{ccw} on the other hand does not comprise an additional soliton phase shift. Pulses in counterclockwise propagation are dispersed due to the propagation through the SSMF. A pulse broadening by a factor $\hat{a}$ leads to a reduction of the peak power by a factor $1/\hat{a}$. The required soliton peak power is reduced simultaneously by a factor $1/\hat{a}^2$, i.e. faster and would allow a soliton formation too. However due to the chirp induced by the transmission through SSMF such soliton formation is not possible. In consequence, the soliton formation is only achieved in clockwise direction.

The fundamental soliton is given by the following equation [114]

$$u(\xi,\tau) = sech(\tau) \cdot \exp\,(i\frac{\xi}{2}). \tag{7.5}$$

Here $\tau = \frac{T}{T_0}$, where T is the laboratory time and T_0 a time characteristic for the pulse width. Using the required phase shift $\frac{\xi}{2} := \pi$ and the definitions $\xi := \frac{z}{L_D}$, $L_D := \frac{T_0^2}{|\beta_2|}$ then

$$\frac{\xi}{2} = \frac{1}{2}\frac{L_{LDF} \cdot |\beta_2|}{T_0^2} = \frac{1}{2}\gamma L_{LDF} P_0 = \pi \tag{7.6}$$

$$L_{LDF} = 2 \cdot \frac{\pi \cdot (\frac{T_{FWHM}}{1.763})^2}{|\beta_2|} \tag{7.7}$$

with L_{LDF} equal to fiber length z and with $T_0 = T_{FWHM}/1.763$ due to the $sech^2$ shape of the soliton pulses. The required fiber length to satisfy the phase shift π therefore scales linearly with T_{FWHM}^2 and $1/|\beta_2|$.

Furthermore a loop operation with nonlinear phase shift requires a certain pulse peak power to form a N=1 soliton. The required power is calculated according to

$$P_0 = \frac{|\beta_2|}{\gamma \cdot T_0^2} \tag{7.8}$$

$$P_{avg} = 2 \cdot \frac{P_0 \cdot T_0}{T_{Bit}}. \tag{7.9}$$

The expression for P_{avg} is derived in eqn. B.11 in sec. B.2. The required input power is determined to satisfy the soliton condition for the clock wise propagating pulse. However, due to the 50:50 power splitting the input power has to be twice as high with $P_{in} = 2 \cdot P_{avg}$ and the final expression is

$$P_{in}[W] = 4 \cdot 1.763 \cdot \frac{|\beta_2|}{\gamma \cdot T_{FWHM} \cdot T_{Bit}} \tag{7.10}$$

if γ is given in $W^{-1}\ km^{-1}$, β_2 in ps^2/km and T,τ in ps. The required average power thus scales with β_2 and the inverse of γ, T_{FWHM} and the bit period T_{Bit}. The latter is equal to the inverse of the pulse repetition frequency, thus the required input power scales linear with the repetition frequency.

The optimum loop layout

According to eqn. 7.6, the DILM operation requires the following condition:

$$2\pi = L_{LDF}\gamma P_0 \tag{7.11}$$

The optimum loop layout has a short fiber length L_{LDF} and low pulse peak power. In consequence a high value of γ is favorable. If an operation over the whole C (S-,L-) band is of further interest, a dispersion flattened highly nonlinear fiber (DF-HNLF) with a low anomalous dispersion is the preferred

choice. Signals with a narrow bandwidth do not experience the effect of different dispersion. Hence the DILM is nontransmitting for these signal components. This property is not valid for the power imbalanced schemes and explains the advantage of a DILM to reach a high extinction ratio [115].

7.2 Investigation of the switching characteristic of a DILM

In the experiments a Dispersion Imbalanced- NOLM = DILM with 100 m DSF as low dispersive fiber (LDF) and 20 m SSMF was used and the improvement of the pulse contrast investigated. A piece of DCF of a length 2 m was placed behind the exit of the loop to compensate for the dispersion the pulses have experienced in the loop.

The evaluation of the measured and calculated power transfer characteristic is shown in Fig. 7.2. shows the measured DILM power balance with the total output power P_{out}, the transmitted power P_{trans} and the reflected power P_{refl} versus the average input power P_{in} of the 10 GHz pulse train with a pulse width of 0.4 ps. Fig. 7.2 (b) depicts a calculation of the power balance of the loop mirror for a pulse train without pedestals.

The power P_{trans} (cf. eqn. 7.1), P_{refl} and P_{out} are defined as follows:

$$P_{trans} = P_{in} \cdot \frac{1}{2}(1 - cos(\Delta\phi)) \tag{7.12}$$

$$P_{refl} = P_{in} - P_{trans} \tag{7.13}$$

$$P_{out} = P_{trans} + P_{refl} \tag{7.14}$$

$\Delta\phi$ is the phase difference between the clock and counter clock wise circulating pulses in the loop. Due to the nonlinear interaction, $\Delta\phi$ depends on the power P_{in}. According to eqn. 7.5 $\Delta\phi$ can be expressed by $\Delta\phi = \frac{\xi}{2}$. Maximum transmission P_{trans} is obtained for $\frac{\xi}{2} = \pi$. The required power P_{in} for this maximum is derived in eqns. 7.5 to 7.10.

For the calculation of the switching behavior of the loop mirror the variables are $T_{Bit} = 100$ ps, $\gamma = 1.6\ W^{-1}\ km^{-1}$ and $\beta_{DSF} = 2.5\ ps\ nm^{-1}\ km^{-1}$ and $L_{LDF} = 100$ m. The dotted lines in Fig. 7.2 indicated $P_{out} = P_{in}$ represent theoretical lines, which take not into account the experimentally observed loss of 2 dB mainly due to splicing. In the calculation the observed loss of 2.0 dB was taken into account. For a pulse width of $T_{FWHM} = 0.4$ ps the required input power for the soliton formation is 22.4 dBm and where experiments show a good pedestal reduction. Here the power losses at the DILM input have to be considered. With these approximations the power balance in Fig. 7.2 (a) is calculated using eqn. 7.12 to 7.14 and compared with the experimental results in Fig. 7.2 (b).

In the measurement of the power balance (Fig. 7.2 (b)) the power minima expected according to eqn. 7.12 and as shown in Fig. 7.2 (a) cannot be observed. In real applications the pulse train comprises not only ideal pulses but also noise components. The deviation of the measured curves can be explained by pulse

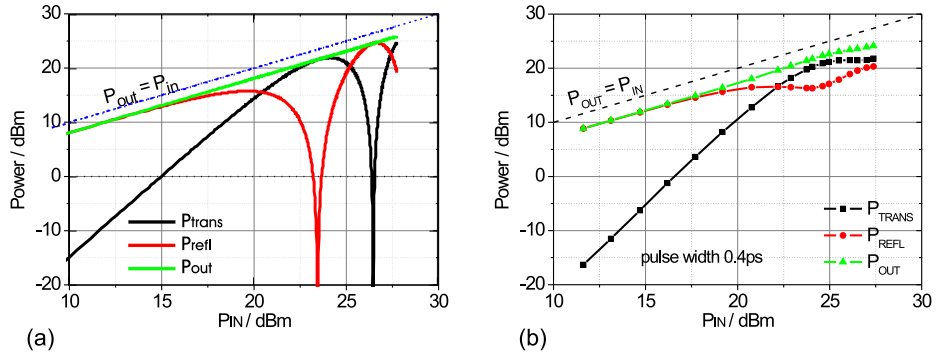

Figure 7.2: (a) DILM power transfer calculated for the ideal pulse train according to eqn. 7.12 without a pedestal and (b) measured for the real pulse train.

pedestals which are reflected independently of P_{in}. This causes a flattening of the curves shown in the calculation.

7.2.1 Experimental results of pedestal reduction by a DILM

Fig. 7.3 (a) shows three curves: The generated pulse shape (Laser) of the original laser signal, the pulse shape (DDF) after pulse compression and the pulse shape (DILM) after pedestal suppression.

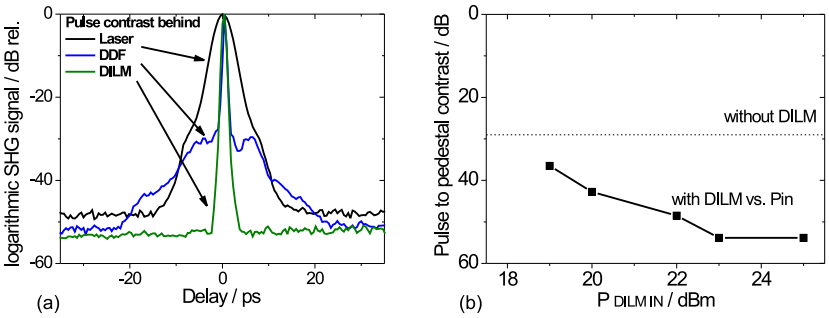

Figure 7.3: (a) Improvement of the pulse contrast using the DILM set-up measured by autocorrelation. The trailing pulses of the EC-MLL are removed together with the pulse pedestal. (b) The pedestal suppression scales with the DILM input power until the phase shift condition is reached.

The peak to pedestal contrast was increased with the increase of the DILM input power as shown in Fig. 7.3 (b). A critical issue is the polarization sensitivity of the DILM. For an improper alignment a noise floor occurs which can cover the whole pedestal structure at the expense of the maximum available

contrast ratio. It was difficult to deduce the minimal necessary pulse power at the input of the DILM but the typical values exceed 20 dBm optical average power for pulses of a width of 0.4 ps. In the experiment the input power into the DILM was increased to reach an optimum switching behavior, which was obtained for an average power above 23 dBm. There was no sharp transition from the complete pulse reflection to the pulse peak transmission.

7.2.2 Noise and Jitter

The phase noise of the modular pulse source (sec. 5.4.3) was evaluated by SSB phase noise measurements. A minor increase in jitter from 50 fs to 60 fs was observed during the compression of the pulses as depicted in the three phase noise curves (Laser, DDF, DILM) in Fig. 7.4.

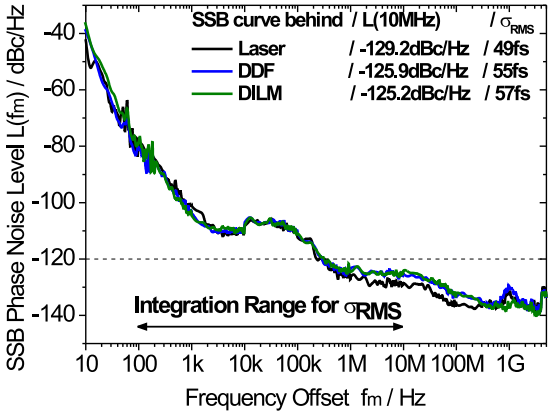

Figure 7.4: Comparison of SSB Phase Noise measurements behind pulse generation (Laser), pulse compression (DDF) and pedestal reduction (DILM)

For a DILM input power of 25.5 dBm the pulse width decreased from 370 fs to 350 fs after the pulse amplification in the EDFA and the transmission through the DILM. Due to the nonlinear switching behavior of the DILM it is also possible to reduce the amplitude noise of the signals.

This property follows from the power dependent periodicity of the switching behavior and can be shown for the NOLM configurations [116] as well as for the DILM configurations as investigated here. The input power into the DILM was chosen to be in a region where the transfer function (cf. Fig. 7.2) reaches a local maximum.

Large input fluctuations can be reduced due to the small change in the transmitted power value. This switching characteristic can be used to improve the pulse amplitude noise of the compressed pulses to values as measured before the pulse compressor. Fig. 7.5 (a) shows the RF spectra between 0 Hz and 13 GHz for the transmitted pulses in dependence of the DILM input power. For

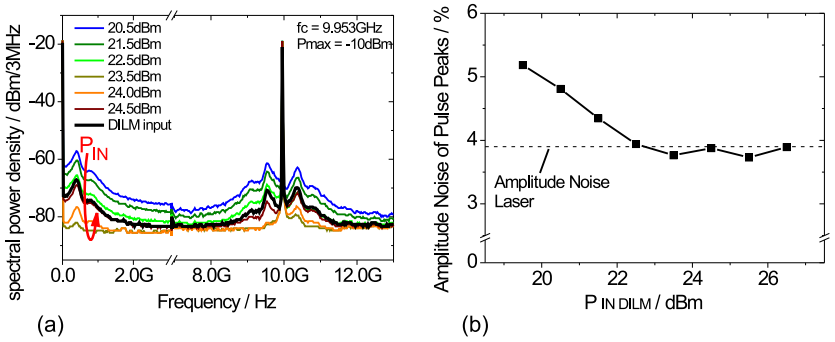

Figure 7.5: (a) Improvement of the RF spectrum with the DILM pulse input power and (b) the reduction of the amplitude noise, measured with a sampling oscilloscope.

the measurement of the spectra the power detected by the electrical spectrum analyzer is kept constant while the DILM input power is varied. For an increase of the DILM input power to 23.5 dBm, the RF spectrum shows a decrease of frequency components distant from the carrier. A further increase of the input power reverses this improvement. In an other measurement the evaluation of the amplitude noise using a sampling oscilloscope according to chap. 2.3 shows the reduction of amplitude noise down to 4% which coincides with the amplitude noise behind the EC-MLL used in this measurement (Fig. 7.5 (b)). The property of the noise reduction by DILM configurations can also be used for a pulse regeneration and reamplification (2R regenerator) in a fiber transmission link. The optimum power for the 2R operation is slightly beyond the maximum of the transfer curve, as suggested [117]. If the pulse energy fluctuates upwards the loop transmission decreases and vice versa, restoring the original state.

7.3 Pedestal reduction by wavelength conversion

The temporal pulse compression is simultaneously leading to a spectral pulse broadening according to the Fourier limitation of the time-bandwidth product. However, the spectral pulse broadening often exceeds this limitation and non-transform limited pulse spectra are formed, e.g. by the supercontinuum generation. A part of the generated spectra can be filtered without a drastic increase of the temporal pulse width. The resulting pulse shape will be closer to the transform limit. This possibility was used in [118] for all-optical 2R pulse regeneration which involved a wavelength conversion.

This implementation is an alternative to the fiber loop set-ups such as the DILM. The spectral power distribution has to be sufficiently uniform and the system set-up has to tolerate a wavelength shift. Especially for the generation of a broad spectrum, e.g. a supercontinuum for the pulse compression, this method can become an alternative [119]. But also for the soliton compression wide optical spectra can be generated. A possible arrangement for a pedestal

reduction by a wavelength conversion uses a laser wavelength at 1535 nm, the first maximum in the EDFA gain curve (cf. Fig. B.4) and converts the pulses to higher wavelengths at 1545 nm and above, where the EDFA gain curve reaches another maximum. The experimental set-up is equivalent with the configuration shown in Fig. 6.1 and 6.7.

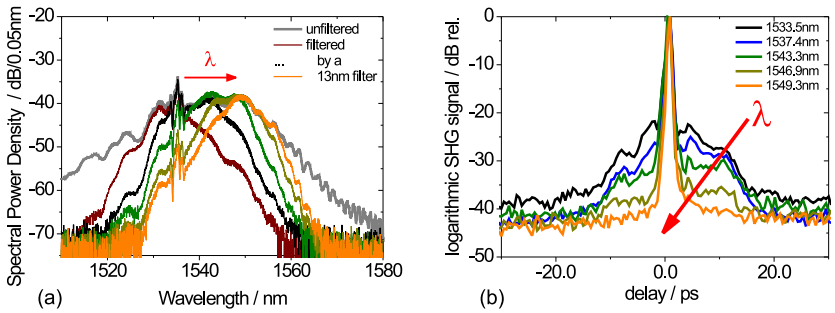

Figure 7.6: (a) A generated broad spectrum behind a DDF fiber compressor and a 13 nm Filter. The input wavelength into the DDF was 1535.2 nm. The wavelength shift by the filter was increased up to a center wavelength of 1550 nm. (b) Autocorrelation of the compressed pulses for different filter wavelength

The optical pulse spectrum shows a wide broadening behind the soliton compression fiber. The shift of the optical filter behind the compression fiber towards longer wavelengths compared to the input wavelength (see Fig. 7.6 (a)) leads to an improvement of the pulse contrast. In this case the pulse to pedestal ratio increased from 21 dB to $\sim$ 40 dB as shown in Fig. 7.6 (b). A wavelength shift to shorter wavelength had the reverse effect. The pulse to pedestal ratio decreased to 17 dB. The pulse width was changed due to the wavelength shift and the resulting dispersion change along the fiber connection between the fiber compressor and the autocorrelator. It was possible to keep the pulse width between 0.37 ps to 0.39 ps for the different wavelength selections if the dispersion was compensated by additional DCF or SSMF.

A pedestal reduction with a wavelength conversion is limited by the spectral power distribution. In Fig. 7.7 (a) the power for the filtered pulse is shown. The power maximum of 19 dBm is measured at a wavelength of 1540 nm. The input pulse had a wavelength of 1535 nm, the input power was 22.5 dBm.

The improvement can be explained by the low peak power of the noise background: The disturbing noise components within the wavelength range of the input pulse can not be removed by an input filter placed before the compression fiber. However, due to the lower peak power the noise components do not experience a broadening by the nonlinear effects such as SPM. A filter behind the compression fiber can be used to remove these components. A prerequisite for the flexible choice of the filter wavelength is a spectral broadening exceeding the transform limit of the desired pulse width. Furthermore an uniform distribution of the pulse power over the wavelength range is favorable for a flexible choice

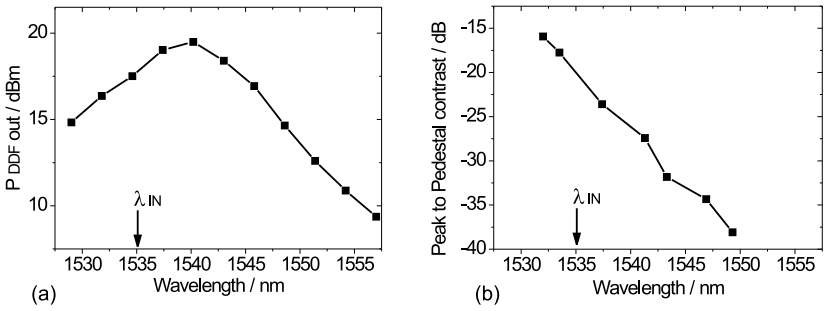

Figure 7.7: Pulse power behind the pulse compressor (a). Pulse width and peak to pedestal contrast for wavelength shifting from 1541 nm to 1551 nm (b).

of the target wavelength. This is not given for each method of compression or available for each input wavelength.

Chapter 8

Application in System Experiments

In this chapter the applicability of the modular pulse source is investigated. The focus is on the prerequisites to generate a 640 Gbit/s data signal.

8.1 Generation of a 640 Gbit/s Data Signal

The pulse sources described in chap. 5 emit a pulse sequence with a repetition frequency of 10 or 40 GHz. The generation of a 640 Gbit/s data signal requires the multiplexing of the laser pulses. A possible method is to use a fiber delay line multiplexer to interleave the original pulse or data sequence to reach multiple repetition frequencies. Detail of the multiplexer layout are discussed in appendix A.3.

Here it is investigated, whether the width of the compressed pulses is sufficiently narrow to generate a 640 Gbit/s data signal. The measurements were performed using the set-up displayed in Fig. 8.1 (a).

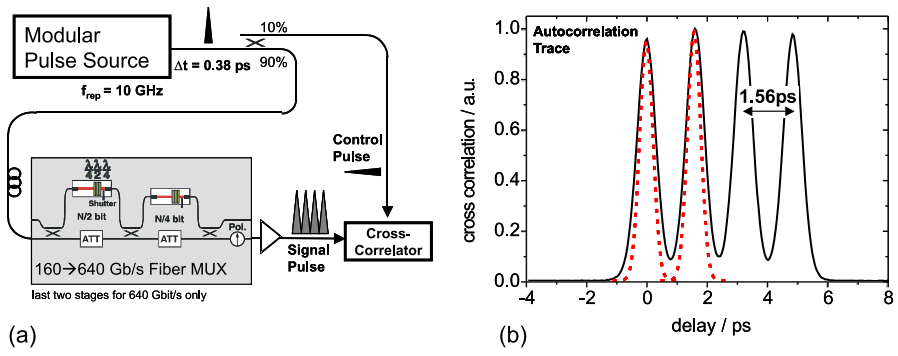

Figure 8.1: (a) Set-up of a cross-correlation measurement and (b) a 640 GHz pulse sequence consisting of 4 pulses with a distance of 1.56 ps.

The 10 GHz pulse train with a pulse width of 0.38 ps was split into two

branches. In one branch the pulse train was multiplexed using the last two stages of a 10 to 640 Gbit/s multiplexer. This generated a single polarization 640 Gbit/s data sequence comprising four "1" followed by sixty "0". This pulse signal was cross-correlated with the 10 GHz pulse train of the second branch.

Fig. 8.1 (b) shows the cross-correlation measurements of the four pulses representing the "1" and having a pulse separation of 1.56 ps. The de-convoluted pulse shapes are also indicated in this figure by dashed red lines. They have a de-convoluted pulse width of 0.43 ps. The separation of the de-convoluted pulses is sufficient for single polarization 640 Gbit/s transmission (cf. [2]).

Fig. 8.2 (a) shows results obtained by the optical sampling system for the pulses generated by the EC-MLL as investigated in sec. 5.1 and (b) the compressed pulses after the DILM. The pulses of the EC-MLL have a pulse width (FWHM) of 3.2 ps, whereas the pulses after compression and pedestal reduction have a width (FWHM) of 0.4 ps. The pulse separation corresponds to a 160 Gbit/s data signal in Fig. 8.2 (a) and to a 320 Gbit/s data signal in (b).

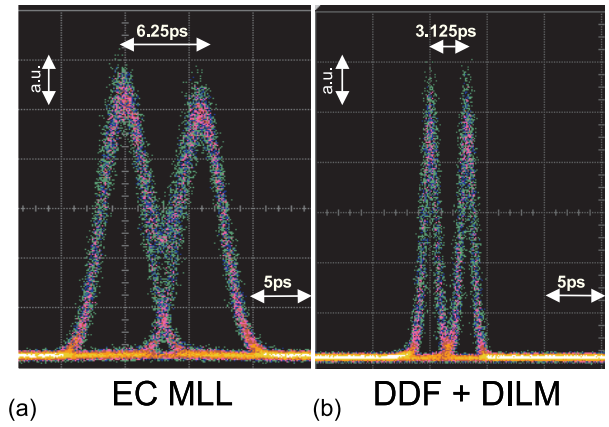

Figure 8.2: Optical sampling traces (a) of a pulse pair of EC-MLL pulses and (b) of compressed pulses after a pedestal reduction in the DILM.

The pulses from the EC-MLL, generated with respect to low phase noise (cf. chap. 5.4.3), show a clear eye opening but also an overlap due to the large pulse width indicating the necessity for pulse compression even for 160 Gbit/s applications. The compressed pulses (b) show a sufficient pulse separation for 320 Gbit/s while the eye opening is maintained. Therefore, these results confirm that the modular set-up for pulse generation provides narrow pulses with an appropriate phase noise performance for 320 Gbit/s transmission. Optical sampling measurements of 640 Gbit/s pulses were not possible due to the limited bandwidth of the sampling set-up and the remaining width of the pulse traces. The precision time base of the measurement oscilloscope had a residual jitter of about 180 fs. An evaluation of the oscilloscope traces revealed σ_{RMS} value of 250 fs and 275 fs for the EC-MLL pulses and the compressed pulses, respectively. Both values include the residual jitter of the precision time base. In comparison a timing jitter value of 230 fs is measured for a fiber ring

laser. Fiber ring laser were successfully used in 640 Gbit/s and 1.24 Tbit/s experiments [2, 3].

8.2 Transmission of 400 fs pulses over 160 km fiber link

In order to verify the quality of the generated short pulses for communication systems, a transmission over a 160 km fibre link was performed. Fig. 8.3 shows the set-up comprising the modular pulse source, two spans of a SLA-IDF fibre, each with a length of 80 km, additional 200 m SSMF for exact dispersion compensation and an autocorrelator (AK) for the evaluation of the transmitted pulses.

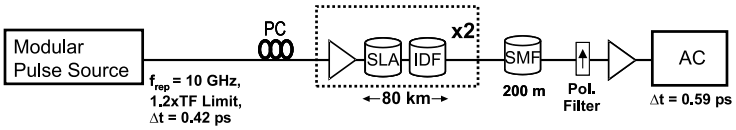

Figure 8.3: Short pulse transmission experiment.

At the output of the modular pulse source an additional optical filter with a filter bandwidth of 16 nm was inserted in order to cut off the spectral components outside the pulse profile, which disturbed the transmission due to higher order dispersion effects.

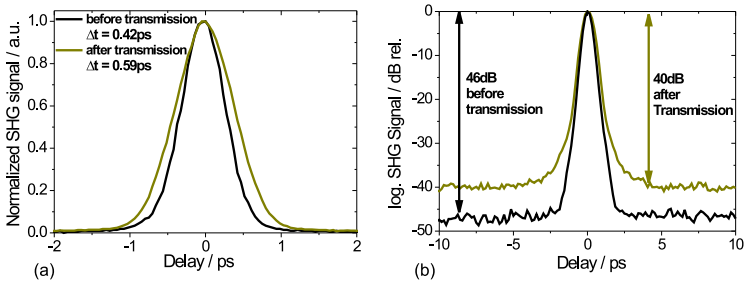

Figure 8.4: (a) pulse width and (b) signal to noise ratio before and after transmission over the 160 km fibre link.

As Fig. 8.4 (a) shows, the pulse width of the transmitted pulses increased from 0.42 ps at the output of the optical filter to 0.59 ps at the end of the transmission link (input of autocorrelator in Fig.8.4). It should be emphasized that a careful polarization alignment for the pulses launched into the transmission link was necessary to obtain a short pulse width at the output of the transmission link. The increase of the pulse width is in agreement with measurements re-

ported in other publications [2, 120]. This pulse broadening is attributed to the PMD and the higher order dispersion β_4 of the transmission set-up including the SSMF and all EDFAs. The signal to noise ratio (SNR) of the autocorrelation trace decreased from 46 dB to 40 dB due to the re-amplification after each fibre span (Fig. 8.4 (b)).

8.3 Demonstration of a DPSK back-to-back measurement up to 640 Gbit/s

The semiconductor mode-locked lasers were operated in several DPSK transmission experiments at data rates of 160 Gbit/s, where a pulse compression is not required. The generated pulses had a widths of 1.3 ps and 1.4 ps in [121, 122] and [123] (cf. sec. A.4) respectively. These experiments show, that the semiconductor mode-locked lasers generate pulse sequences with a stable phase relation between adjacent pulses suitable for an application in transmission experiments using a phase modulation format.

For a transmission experiments at 320 Gbit/s or higher the pulse generation by a semiconductor mode-locked laser needs an additional pulse width reduction and a pedestal removal. As shown in the preceding chapters a modular pulse generator can provide these functions to improve the pulse quality for an application in transmission systems.

In order to confirm the functionality, the modular pulse generator has to be tested for data rates higher than 160 Gbit/s for transmission experiments with e.g. differential phase shift keying modulation format.

For the investigation a test-bed with a transmitter (Tx) and a receiver unit (Rx) was used as shown in Fig. 8.5. The pulse source of the transmitter, a semiconductor EC-MLL with ion implantation is operated at a wavelength 1556 nm and emitted a 10 GHz pulse train with a pulse width of 3.45 ps. The pulses are compressed in HNL-DDF (sec. 6.1.3) and shaped in a DILM (sec. 7.2) to a pulse width of 0.42 ps with sech^2 shape. The output wavelength of the laser is slightly shifted to 1555 nm, determined by a filter behind the pedestal reduction. In order to reduce the influence of spectral bandwidth limiting elements, such as EDFAs and of the residual dispersion of the set-up, the generated pulse train is filtered by a 8.0 nm filter. In consequence the pulse width is broadened to 490 fs at the transmitter output.

A phase modulator is used to generate a DPSK data train with a base rate of 10 Gbit/s. It is driven by a Bit Pattern Generator (BPG), which provides a 2^7-1 PRBS data signal. The fiber length between pulse source and modulator is exceeding 1000 m. Therefore a clock signal had to be extracted to drive the BPG and modulator. The modulated 10 Gbit/s DPSK bit sequence is multiplexed in an optical delay line multiplexer to a data rate of up to 640 Gbit/s in single polarization, single wavelength channel signal at the transmitter exit.

The multiplexed data signal of the transmitter is inserted into a receiver. The receiver set-up comprises a NOLM-based demultiplexer with dispersion flattened HNLF of 300 m length. The control pulses for switching are provided by a 40 GHz control pulse laser operating at the wavelength 1532 nm and having

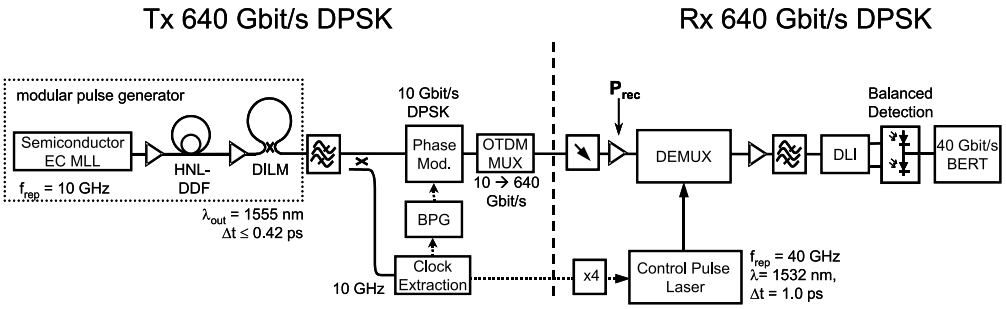

Figure 8.5: Setup for the BER measurement in back-to-back configuration for data rates of up to 640 Gbit/s in single polarization, single wavelength channel DPSK format. The pulse source is a semiconductor EC-MLL, either comprising a one section laser diode with implantation or a two section laser diode, both described in sec. 5.1 and sec. 5.2. The pulse width is reduced in the modular pulse generator to $\Delta t \leq 0.42$ ps.

a pulse width of 1.0 ps. The demultiplexed signals are inserted into a delay line interferometer (DLI) to convert the phase information of the pulse train into an amplitude modulation. A balanced photo detector is used for the measurement of both logical states of the demultiplexed DPSK data train.

Fig. 8.6 shows the BER curves for a received DPSK bit sequence of 40 Gbit/s without demultiplexer, for a DPSK bit sequence of 40 Gbit/s, which passed the demultiplexer without active switching[1] and BER curves for the demultiplexing of 320 Gbit/s and 640 Gbit/s to 40 Gbit/s. The BER curves show the possibility of an error free detection of bit rates up to 320 Gbit/s. For 640 Gbit/s a noise floor limited the BER to 10^{-7}. This is well below the maximum tolerable limit for the application of a forward error correction of 10^{-3}, which has to be applied in this case. The 320 Gbit/s demultiplexing experiment was also performed with a different pulse source in the transmitter. Instead of the EC MLL with ion implantation (5.1) also the EC MLL with a two section laser diode (5.2) was used. With the latter pulse source a back-to-back BER measurement with BER $< 10^{-3}$ was not possible.

The remaining phase noise and additional amplitude noise, partially converted into further phase deviations in the process of pulse compression, is suspected to lead to the observed slight occurrence of a curvature in the BER measurement, which finally lead to the formation of an error floor for 640 Gbit/s. Note also, that the pulse width is as high as 650 fs (cf. requirement $\Delta\, t \leq 0.3/\mathrm{B} = 470$ fs sec. 1.2) at the demultiplexer due to the spectral filtering in the transmitter and the inevitable pulse broadening in the complete set-up including the demultiplexer (NOLM).

A confirmation, that the set-up of the pulse compression and pedestal reduction itself do not disturb the phase coherence was made with an error free

[1]The passage of the demultiplexer at 40 Gbit/s provides a reference measurement of the complete set-up including the switch (NOLM) rather then separating pulses in the literally sense.

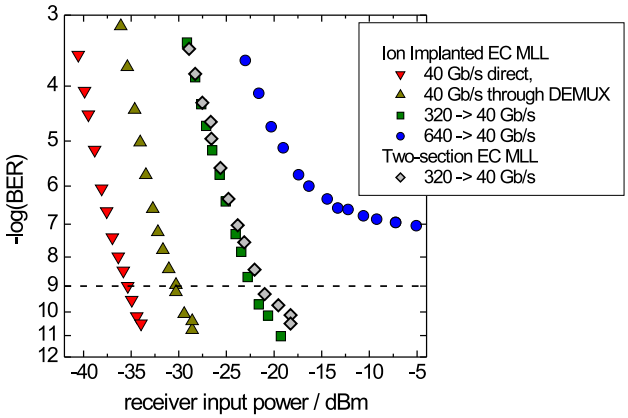

Figure 8.6: Back-to-back BER measurement for the DPSK data trains demultiplexed from bit rates of 320 and 640 Gbit/s to 40 Gbit/s. The BER curves are shown for pulse trains generated by the modular pulse generator comprising a the semiconductor mode-locked laser with ion implantation and, in case of 320 Gbit/s, also of the two-section mode-locked laser.
The BER curves are shown for the demultiplexing from 320 to 40 Gbit/s and 640 to 40 Gbit/s. For the demultiplexed 320 Gbit/s data train the receiver sensitivity was -22.4 dBm and 21.3 dBm for the both laser, respectively. Further BER curves show the performance for the direct detection of the data signal without DEMUX and for the unswitched transmission through the demultiplexer, both at 40 Gbit/s.

1.28 Tbit/s transmission experiment using a solid state laser pulse source [124]. Hereby the solid state mode-locked laser was operated at the wavelength of 1550 nm and the generated 10 GHz pulse train had a phase noise of 40 fs, about as low as the RF reference provided by a synthesizer. The pulse width of 2.1 ps pulse was similarly reduced to 420 fs in the pulse compressor and allowed an error free transmission at a data rate of 640 Gbit/s in single channel single polarization transmission with the DPSK modulation format. The transmitter and receiver set-up for the transmission experiment was identical to the one shown in Fig. 8.5.

These results confirm the possibility to use semiconductor MLL as a pulse source in a modular pulse generator for DPSK transmission experiments at 320 Gbit/s. The phase coherence of a pulse train is conserved in the pulse compressor and the pulse shaper. Both components are suitable modules for a pulse generator for transmission systems with data rates of up to 640 Gbit/s.

Chapter 9

Summary and Conclusion

The objective of this work was to assemble an optical pulse generator, suitable for pulse generation in OTDM transmission systems operated at data rates between 160 to 640 Gbit/s. High data rate OTDM systems require temporal short pulses with a low timing jitter and a sufficient pulse to pedestal contrast. The evaluation of the pulse properties often reaches the accuracy limits of the measurement devices. Therefore, the pulse evaluation has to be made by various measurement techniques such as single side band phase noise measurement, autocorrelation measurement, optical spectrum analysis and optical sampling to provide a reliable information about the pulse quality.

Different optical pulse sources, such as fiber ring laser, solid state laser, semiconductor laser and EAM modulated cw-signals are suitable for an application in OTDM systems. An emphasis of this work was the investigation of the pulse generation based on semiconductor mode-locked laser in different configurations. Two possibilities were identified: 1. a configuration in an external cavity set-up, which offers a high flexibility in wavelength and repetition frequency; 2. the monolithic integrated mode-locked laser with a limited but sufficient tunability for an application in a commercial transmission system. A further difference is the type of the saturable absorber used for the passive mode-locking. The saturable absorption can be reached by introduction of additional recombination centers with ion implantation or by the carrier removal in a separate, short, reverse biased absorber section. The ion implantation of the laser diodes requires great efforts and the access to an implantation facility. It leads to a fixed definition of the absorber strength. The reversed biased absorber sections requires a longer diode length in order to compensate for the longer absorber recovery times. All configurations have proofed to be suitable to generate optical pulses with a width of the order of 1 - 3 ps and a timing jitter below 100 fs (integration range 100 Hz - 10 MHz).

The main reason for the phase noise is the spontaneous emission included in the lasing process in the pulse generation. A reduction of the phase noise can be reached by a smaller spectral filter bandwidth of the grating used in the laser cavity to select the operation wavelength. Under these conditions the width of the generated pulses increased to a pulse width of up to 3 ps. Thus the phase noise can be reduced on expense of the pulse width of the generated pulses. The

minimum phase noise obtained was about 60 fs and achieved the limit required for 640 Gbit/s transmission. A similar situation concerns the amplitude noise. The increase of the amplitude noise with higher absorber voltages is indicating the slight transition to a pulsating laser operation. Distinct pulsating laser operation was observed for the monolithic laser diodes. In order to avoid the influence of these effects the laser devices with separate saturable absorber were operated at an absorber voltage between 1 and 2 V. This is below the maximum possible value, typically exceeding 3 V. It reduced the amplitude and phase noise in the generated pulse train. However, both improvements are reached on expense of the pulse width of the generated pulses.

A pulse generation for OTDM applications requires short pulse widths in the order of 400 fs for 640 Gbit/s and 800 fs for 320 Gbit/s applications and a phase noise of about 65 fs for 640 Gbit/s and 130 fs for 320 Gbit/s. Consequently, the pulse generation with a semiconductor mode-locked laser inherits a trade-off between a low noise pulse generation on the one hand side and a short pulse generation on the other hand side. Phase noise reduction outside the laser resonator is difficult to achieve. Especially the higher frequency components above 1 MHz, characteristic for the semiconductor devices, are difficult to remove. Feed back loops can be used to stabilize the pulse generation but fail to show an improvement for high frequency components. For the application of the generated low noise pulse trains in a 640 Gbit/s OTDM system an external pulse compression becomes inevitable. Pulse compression is often accompanied by the formation of a pulse pedestal which has to be removed. This leads to the modular concept of a pulse generator based on the separate blocks of the pulse source, the pulse compression and the pulse shaping.

Fiber based pulse compression avoids the necessity of an elaborate free space set-up and relaxes the requirements on stability against mechanical vibrations. Fiber based pulse compression exploits the nonlinear effects resulting from the Kerr effect for high optical pulse powers. In the frame of this work the soliton pulse compression and the supercontinuum generation were investigated. For the soliton compression different linear dispersion decreasing fibers (DDF) were used. In order to relax the power requirements, a DDF with an increased nonlinearity was successfully used to compress a 3 ps 37.5 GHz pulse train with an input power as low as 23 dBm to reach a final pulse width of 0.38 ps. Alternatively pulse compression using the generation of a spectral broadened chirped pulse, the so-called supercontinuum generation, was implemented. The maintenance of high pulse quality requires a supercontinuum generation with a highly nonlinear fiber in the normal dispersion region. A dispersion flattened HNL fiber avoids higher order dispersion limitations and can be applied over the complete C-Band. The final pulse width of the compressed and filtered pulses was 0.40 ps. Both methods showed their suitability with respect to the pulse requirements for OTDM systems.

The compressed pulses are often impaired by the formation of a pulse pedestal reducing the pulse to pedestal contrast to less than 30 dB and have to be removed. Therefore imbalanced loop switches are an effective choice. A dispersion imbalanced loop setup, consisting of dispersion shifted fiber and standard single mode fiber was used to remove the pulse pedestals adjacent

to the pulse peak. The pulse to pedestal contrast was improved to more than 40 dB. The switching characteristic of a dispersion imbalanced loop mirror provides a reflection of low power components such as noise and pulse pedestals independent from the input power. Another possibility to improve the pulse contrast is a wavelength conversion between the generated pulses and the compressed pulses. Pulse compression leads to temporal short pulses with a broad wavelength spectrum. Often the spectral broadening was higher than necessary for a transformation limited pulse. The filtering of a part of the optical spectrum can remove disturbing spectral components and improves the pulse shape, provided a suitable choice for the filtered wavelength is possible.

The functionality of the modular pulse generator and its subcomponents was demonstrated in several experiments. Due to the modular nature of the pulse generation concept the components of the low noise short pulse generator can be used separately. The mode-locked laser can be used for a pulse generation suitable for data rates up to 160 Gbit/s OTDM with long term stability and without need of further pulse shaping using either OOK or DPSK modulation format. The pulse compressor works in combination with every low noise pulse source, or just as a stand alone pulse compression unit for an incoming pulse train. The loop mirror for the pedestal reduction can be applied at any place of a transmission system to remove disturbing pulse pedestals after a pulse compression but also after a pulse transmission over a fiber link. Both can be used for data signals with OOK or DPSK modulation format. An back-to-back measurement was demonstrated for the combination of a semiconductor external cavity mode-locked laser, soliton compressor and dispersion imbalanced loop mirror at 320 Gbit/s and 640 Gbit/s. The bit error rates BER reached values below 10^{-9} and $< 10^{-3}$, respectively. The soliton compressor and the pedestal reduction where used in combination with an solid-state laser for an error free (BER $< 10^{-9}$) transmission experiment over 160 km with a single channel single wavelength and single polarization pulse repetition frequency of 640 GHz.

Bibliography

[1] A. Suzuki, X. Wang, Y. Ogawa, and S. Nakamura. 10x320Gb/s (3.2Tb/s) DWDM/OTDM transmission in C-band by semiconductor-based devices. In *Proc. Europ. Conf. Opt. Commun. (ECOC)*, pages 14–5, Stockholm, Sweden, 2004. PD paper 4.1.7.

[2] T. Yamamoto, E. Yoshida, K.R. Tamura, K. Yonenaga, and M. Nakazawa. 640-Gbit/s Optical TDM Transmission Over 92 km Through a Dispersion-Managed Fiber Consisting of Single-Mode Fiber and "Reverse Dispersion Fiber". *IEEE Phot. Techn. Lett.*, 12(3):353–5, Mar. 2000.

[3] M. Nakazawa, T. Yamamoto, and K.R. Tamura. 1.28Tbit/s-70km OTDM transmission using third- and fourth-order simultaneous dispersion compensation with a phase modulator. *El. Lett.*, 36(24):2027–9, Nov. 2000.

[4] D. Breuer and K. Petermann. Comparison of NRZ- and RZ-Modulation Format for 40-Gb/s TDM Standard-Fiber Systems. *IEEE Phot. Techn. Lett.*, 9(3):398–400, 1997.

[5] R. Ludwig, U. Feiste, E. Dietrich, Hans-Georg Weber, D. Breuer, M. Martin, and F. Küppers. Experimental Comparison of 40 Gbit/s RZ and NRZ Transmission over Standard Singlemode Fibre. *El. Lett.*, 35(25):2216–8, 1999.

[6] R. Ludwig, W. Pieper, Hans-Georg Weber, D. Breuer, K. Petermann, F. Küppers, and A. Mattheus. Unrepeatered 40 Gbit/s RZ Single Channel Transmission over 150 km of Standard Fiber at 1.55 μm. *El. Lett.*, 36(16):1405–6, 2000.

[7] A. T. Clausen, H. N. Poulsen, L.K. Oxenløwe, A.I. Siahlo, J. Seoane, and P. Jeppesen. Pulse Source Requirements For OTDM Systems. In *IEEE LEOS Annual Meeting Conference Proceedings, Tucson, AZ, USA*, 2003.

[8] N. Klussmann. *Lexikon der Kommunikations- und Informationstechnik.* Hüthig Verlag Heidelberg, 1997.

[9] F. Oberhettinger. *Tables of Fourier Transforms and Fourier Transforms of Distributions.* Springer Verlag Berlin, Heidelberg, 1990. Chapt. Sec. Hyperbolic Functions.

[10] Y. Takushima, H. Sotobayashi, M.E. Grein, E.P. Ippen, and H.A. Haus. Linewidth of mode combs of passively and actively mode-locked semiconductor laser diodes. *Proc. of SPIE*, 5595:213–27, 2004.

[11] M. Kroh, C.M. Weinert, C. Schmidt-Langhorst, C. Schubert, J. Berger, C. Boerner, R. Ludwig, and H.G. Weber. Semiconductor Mode-Locked Laser Pulse Source for 320 and 640 Gb/s RZ Data Transmitter. In *Proc. Europ. Conf. Opt. Commun. (ECOC)*, pages 442–3, Stockholm, Sweden, 2004. paper We 3.5.7.

[12] *Manual by APE GmbH: APE Autocorrelator PulseCheck*, July 2001.

[13] New Zealand Southern Photonics, Auckland. SHG FROG - HR 150. URL: http://www.southernphotonics.com, 2005.

[14] Advantest Corporation. *Optical Spectrum Analyzer Q 8384*. Tokyo, Japan, 2003.

[15] Rohde und Schwarz. *Electrical Spectrum Analyzer FSEK30 Manual*. München, Germany, 2002.

[16] U2t Photonics. URL http://www.u2t.de/. Technical report, 2005.

[17] C. Schmidt-Langhorst. *Optical-Sampling of High Bit Rate Optical Data Signals*. PhD thesis, Technische Universität Berlin, Berlin, 2004.

[18] S. Watanabe, R. Okabe, F. Futami, R. Hainberger, C. Schmidt-Langhorst, C. Schubert, and H.G. Weber. Novel Fiber Kerr-Switch with Parametric Gain: Demonstration of Optical Demultiplexing and Sampling up to 640 Gb/s. In *Proc. Europ. Conf. Opt. Commun. (ECOC)*, pages 12–3, Stockholm, Sweden, 2004. PDL 4.1.6.

[19] Carsten Schmidt-Langhorst, Colja Schubert, Christof Boerner, Sebastian Ferber, Reinhold Ludwig, Joern Berger, Enno Hilliger, Vincent Marembert, Marcel Kroh, Hans-Juergen Ehrke, and Hans-Georg Weber. Ultrafast technologies in 160 Gbit/s transmission systems. In *SPIE International Symposium "IT COM", Pennsylvania, USA*, 2004.

[20] J. Eichler and H.J. Eichler. *Laser. Bauformen, Strahlführung, Anwendungen.* Springer Verlag Berlin, Heidelberg, New York, 1998.

[21] K. L. Sala, Wallace A. Kenny, and G. E. Hall. CW autocorrelation measurements of picosecond laser pulses. *IEEE J. Quantum Electron.*, QE-16(9):990–6, 1980.

[22] R. Trebino. *Frequency-Resolved Optical Gating: The Measurement of Ultrashort Laser Pulses*. Kluwer Academic Publishers Group, AH Dordrecht, The Netherlands, 2002.

[23] D. J. Kane. Real-Time Measurement of Ultrashort Laser Pulses Using Principal Component Generalized Projections. *IEEE J. of Selected Topics in Q. Electr.*, 4(2):278–85, Mar/Apr 1998.

[24] APEX Technologies. URL http://www.dmoptics.com/Downloads/Apex/OGAModule.pdf. Technical report, 2005.

[25] Christoph Rauscher. *Grundlagen der Spektrumanalyse*. Rohde Schwarz GmbH Co. KG, München, 2000.

[26] J. P. Gordon and H. A. Haus. Random walk of coherently amplified solitons in optical fiber transmission. *Opt. Lett.*, 11(10):665–7, Oct. 1986.

[27] D. Von der Linde. Characterization of the Noise in Continuously Operating Mode-Locked Lasers. *Appl. Phys. B*, 39:201–17, 1986.

[28] Leaf Alden Jiang. *Ultralow-Noise Modelocked Lasers*. PhD thesis, Massachusetts Institute of Technology, May 2002.

[29] Ryan P. Scott, Carsten Langrock, and Brian H. Kolner. High-dynamic-range laser amplitude and phase noise measurement techniques. *IEEE J. of Selected Topics in Q. Electr.*, 7(4):641–55, Jul./Aug. 2001.

[30] T. Yilmaz, C.M. DePriest, and Jr. P.J. Delfyett. Complete noise characterisation of external cavity semiconductor laser hybridly modelocked at 10 Ghz. *El. Lett.*, 37(22):1338–9, Oct. 2001.

[31] Wavecrest. Jitter fundamentals seminar. Technical report, 2001. URL: http://www.wavecrest.com/technical/jitterfund.htm and -/Briefs.htm.

[32] Data sheets: Spectrum analyzers FSEx. URL: http://www.rohde-schwarz.com/, Jun 24, 1999.

[33] D.J. Derickson, P.A. Morton, J.E. Bowers, and R.L. Thornton. Comparison of Timing Jitter in External and Monolithic Cavity Mode-Locked Semiconductor Lasers. *Appl. Phys. Lett.*, 59(26):3372–4, 1991.

[34] Jitter and Wander Measuring Equipment for Digital Systems Which are Based on the Synchronous Digital Hierarchy (SDH). Recommendation O.172, ITU-T, 2001.

[35] The Control of Jitter and Wander Within the Optical Transport Network (OTN). Recommendation G.8251, ITU-T, 2001.

[36] L.A. Jiang, M.E. Grein, H.A. Haus, and E.P. Ippen. Noise of Mode-Locked Semiconductor Lasers. *IEEE J. of Selected Topics in Q. Electr.*, 7(2):159–67, Mar./Apr. 2001.

[37] F. K. Kneubühl and M. W. Sigrist. *Laser*. Studienbücher : Physik. B. G. Teubner, Stuttgart, 1988.

[38] Claude Rullière. *Femtosecond Laser Pulses*. Springer-Verlag Berlin Heidelberg New York, 1998.

[39] A. Weber. *Erzeugung Von Ps-Lichtpulsen Durch Modenkopplung in Halbleiterlasern*. PhD thesis, Technische Universität Berlin, 1992.

[40] M. Schell. *Erzeugung Ultrakkurzer Lichtpulse mit Halbleiterlasern: Theorie und Experiment*. PhD thesis, Technische Universität Berlin, 1993.

[41] E.A. Avrutin, J.H.Marsh, and E.L. Portnoi. Monolithic and multi-GigaHertz mode-locked semiconductor lasers: Constructions, experiments, models and applications. *IEE Proc. Optoelectronics*, 147(4):pp.251–78, Aug. 2000.

[42] S.C. Zeller, L. Krainer, G.J. Spühler, R. Pascotta, M. Golling, D. Ebling, K.J. Weingarten, and U. Keller. Passive mode-locked 50-GHz Er:Yb:glass laser. In *Proc. Europ. Conf. Opt. Commun. (ECOC)*, pages 918–9, Vol. IV, Stockholm, Sweden, 2004. paper Th 3.4.3.

[43] K.J. Ebeling. *Integrierte Optoelektronik*. Springer Verlag, 2. Aufl., 1992.

[44] *Product Information by Calmar Optcom Inc.: Actively Mode-Locked Fiber Lasers, URL: http://www.calmaropt.com/frame.html?technology.html*.

[45] G.T. Harvey and L.F. Mollenauer. Harmonically mode-locked fiber ring laser with an internal Fabry-Perot stabilizer for soliton transmission. *Opt. Lett.*, 18(2):107–9, Jan. 1993.

[46] E. Yoshida and M. Nakazawa. Wavelength tunable 1.0ps pulse generation in 1.530-1.555μm region from PLL, regeneratively modelockeed fibre laser. *El. Lett.*, 34(18):1753–4, Sep. 1998.

[47] Z. Hu, F. Li, Z. Pan, and W. Tan. Wavelength-Tunable Narrow-Linewidth Semiconductor Fiber-Ring Laser. *IEEE Phot. Techn. Lett.*, 12(8):977–9, Aug. 2000.

[48] X. Shan and D.M. Spirit. Novel Method To Suppress Noise In Harmonically Modelocked Erbium Fibre Lasers. *El. Lett.*, 29(11):pp.979–981, May 1993.

[49] M. Nakazawa *et al.* 1.28tbis/s - 70km otdm transmission using third- and fourth-order simultaneous dispersion compensation with a phase modulator. In *Proc. Europ. Conf. Opt. Commun. (ECOC)*, Munich, Germany, 2000. PD paper 2.6.

[50] E. Hilliger. *Optisches Schalten mit Elektroabsorptionsmodulatoren*. PhD thesis, Technische Universität Berlin, 2003.

[51] M.D. Pelusi, Y. Matsui, and A. Suzuki. Femtosecond Optical Pulse Generation From An Electro-Absorption Modulator With Repetition Rate And Wavelength Tuning. In *Proc. Europ. Conf. Opt. Commun. (ECOC)*, pages 26–7, Vol II, Nice, France, 1999.

[52] G. Raybon, B. Mikkelsen, R.-J. Essiambre, J.E. Johnson, K. Dreyer, and L.E. Nelson. 100 Gbit/s Single-Channel Transmission Over 200 km TrueWave® And 160 km Conventional Fiber With EAM Source And Demultiplexer. In *Proc. Europ. Conf. Opt. Commun. (ECOC)*, volume II, pages 92, Vol. II, Nice, France, 1999. paper WeC 2.5.

[53] B. Mikkelson, G. Raybon, and R.-J. Essiambre. 160Gb/s TDM Transmission Systems. In *Proc. Europ. Conf. Opt. Commun. (ECOC)*, volume II, pages 125–8, 2000. paper 6.1.1.

[54] K. Sato, A. Hirano, and H. Ishii. Chirp-Compensated 40-GHz Mode-Locked Lasers Integrated with Electroabsorption Modulators and Chirped Gratings. *IEEE J. of Selected Topics in Q. Electr.*, 5(3):590–5, May/June 1999.

[55] R. Ludwig and A. Ehrhardt. Turn-key-ready wavelength-, repetition rate- and pulsewidth-tunable femtosecond hybrid modelocked semiconductor laser. *El. Lett.*, 31(14):1165–7, July 1995.

[56] R. Kaiser, B. Hüttl, H. Heidrich, S. Fidorra, W. Rehbein, H. Stolpe, R. Stenzel, W. Ebert, and G. Sahin. Tunable Monolithic Mode-Locked Lasers on InP with Low Timing Jitter. *IEEE Phot. Techn. Lett.*, 15(5):634–6, May 2003.

[57] B. Huettl, R. Kaiser, W. Rehbein, H. Stolpe, Ch. Kindel, S. Fidorra, A. Steffan, A. Umbach, and H. Heidrich. Low Noise Monolithic 40 GHz Mode-Locked DBR Lasers Based On GaInAsP/InP. In *Indium Phosphide and Related Materials Conference, Glasgow, Optoelectronics 5, Edge Emitting Lasers*, 2005.

[58] Marcus Dülk, Max Döbeli, and Hans Melchior. Fabrication of Saturable Absorbers in InGaAsP-InP Bulk Semiconductor Laser Diodes by Heavy Ion Implantation. *IEEE J. of Selected Topics in Q. Electr.*, 7(2):124–34, 2001.

[59] E. L. Portnoi, N.M. Stel'makh, and A.V. Chelnokov. Characteristics of heterostructure lasers with a saturable absorber fabricated by deep ion implantation. *Sov. Tech. Phys. Lett.*, 15(6):432–3, Jun. 1989.

[60] H.H. Tan, C. Jagadish, M.J. Lederer, B. Luther-Davies, J. Zou, D.J.H. Cochayne, M. Haiml, U. Siegner, and U. Keller. Role of implantation-induced defects on the response time of semiconductor saturable absorbers. *Appl. Phys. Lett.*, 75(10):1437–9, Sept. 1999.

[61] C. Carmody, H.H. Tan, C. Jagadish, A. Gaarder, and S. Marcinkevicius. Ultrafast carrier trapping and recombination in highly resistive ion implanted InP. *Journal of Applied Physics*, 94(2):1074–8, 2003.

[62] S. Marcinkevicius, C. Carmody, A. Gaarder, H.H. Tan, and C. Jagadish. Ultrafast carrier dynamics in highly resistive InP and InGaAs produced by ion implantation. In *Proceedings of the SPIE, Vol 5352 (2004), No 1; Conference on Ultrafast Phenomena in Semiconductors and Nanostructure Materials*, pages 299–309, San Jose, CA, USA, 2003.

[63] G. N. Maracas, K. Shiralagi, R. Ramamurti, and R. W. Carpenter. A comparison of As and P-based semiconductors grown at low temperatures by MBE and GSMBE. *J. of Electronics Materials*, 22(12):1375–81, 1993.

[64] T. Ikegami. Reflectivity of Mode at Facet and Oscillation Mode in Double-Heterostructure Injection Lasers. *IEEE J. Quantum Electron.*, 8(6):470–6, Jun. 1972.

[65] R. Ludwig. *Experimentelle Untersuchungen an Halbleiterlaserverstärkern Für Die Optische Nachrichtentechnik*. PhD thesis, Technische Universität Berlin, 1993.

[66] K. Yvind. *Semiconductor Mode-Locked Lasers for Optical Communication Systems*. PhD thesis, Technical University of Denmark, 2003. $URL : http://www.Yvind.dk/kresten/Yvind_PhD_dp.pdf$.

[67] Y. Suzaki, K. Magari, Y. Kondo, Y. Kawaguchi, Y. Kadota, and K. Yoshino. High-Gain Array of Semiconductor Optical Amplifier Integrated With Bent Spot-Size Converter (BEND SS-SOA). *IEEE J. Lightwave Technol.*, 19(11):1745–50, Nov. 2001.

[68] S. Arahira, N. Mineo, K. Tachibana, and Y. Ogawa. 40 GHz hybrid modelocked laser diode module operated at ultra-low RF power with impedance-matching circuit. *El. Lett.*, 39(3):287–9, 2003.

[69] K. Sato, A. Hirano, and H. Ishii. Chirp-Compensated 40-GHz Mode-Locked Lasers Integrated with Electroabsorption Modulators and Chirped Gratings. *IEEE J. of Selected Topics in Q. Electr.*, 5(3):590–5, May/Jun. 1999.

[70] M. Schell, M. Tsuchiya, and T. Kamiya. Chirp and Stability of Mode-Locked Semiconductor Laser. *IEEE J. Quantum Electron.*, 32(7):1180–90, Jul. 1996.

[71] M. Kroh, B. Hüttl, S. Ferber, and H. G. Weber. Low noise 400 fs pulse generation by monolithic semiconductor mode-locked laser and soliton pulse compression. In *CLEO Europe*, Munich, Germany, 2005. paper CB8-2-THU.

[72] U. Keller, K.J. Weingarten an F.X. Kartner, D. Kopf, B. Braun, I.D. Jung-I-D, R. Fluck, C. Honninger, N. Matuschek, and J. Aus der Au. Semiconductor Saturable Absorber Mirrors (SESAM's) for Femtosecond to Nanosecond Pulse Generation in Solid-State Lasers. *IEEE J. of Selected Topics in Q. Electr.*, 2(3):435–53, Sep. 1996.

[73] H.-F. Liu, S. Arahira, T. Kunii, and Y. Ogawa. Tuning Characteristics of Monolithic Passively Mode-Locked Distributed Bragg Reflector Semiconductor Lasers. *IEEE J. Quantum Electron.*, 32(11):1965–75, Nov. 1996.

[74] S. Murata, I. Mito, and K. Kobayashi. Over 720 GHz (5.8nm) frequency tuning by a 1.5 μm DBR laser with phase and bragg wavlength control regions. *El. Lett.*, 23(8):403–5, Apr. 1987.

[75] Ye Cunyun. *Tunable External Cavity Diode Lasers*. World Scientific Publishing Co Inc, Singapore, 2004. ISBN 9812560882.

[76] K. Yvind, D. Larsson, L. J. Christiansen, C. Angelo, L. K. Oxenløwe, J. Mørk, D. Birkedal, J. M. Hvam, and J. Hanberg. Low-jitter and high-power all-active mode-locked lasers. In *ECOC*, Rimini, Italy, 2003. Tu 4.5.4.

[77] M. Kroh, C. Schmidt, R. Ludwig, C. Schubert, and Hans-Georg Weber. Investigations on Phase Noise in a Semiconductor Mode-Locked Laser. In *Proc. Optical Fiber Commun. (OFC)*, pages 673–4, Washington, DC, March 2003. paper FF 5.

[78] O. Brox. *DFB-Laser mit Integriert Optischer Rückkopplung Für Die Optische Signalverarbeitung.* PhD thesis, Technische Universität Berlin, 2005.

[79] L.A. Jiang, M.E. Grein, and E.P. Ippen. Quantum-limited noise performance of a mode-locked laser diode. *Opt. Lett.*, 27(1):49–51, 2001.

[80] S.V. Chernikov, D.J. Richardson, E.M. Dianov, and D.N. Payne. Picosecond Soliton Pulse Compressor Based On Dispersion Decreasing Fibre. *El. Lett.*, 28(19):1842–4, Sept. 1992.

[81] W.J. Tomlinson, R.H. Stolen, and C.V. Shank. Compression of optical pulses chirped by self-phase modulation in fibers. *J. Opt. Soc. Am. B*, 1(2):139–49, Apr. 1984.

[82] K.R. Tamura, H. Kubota, and M. Nakazawa. Fundamentals of Stable Continuum Generation at High Repetition Rates. *IEEE J. Quantum Electron.*, 36(7):773–9, July 2000.

[83] G.P. Agrawal. *Nonlinear Fiber Optics.* Academic Press, 2000.

[84] Vladimir A. Bogatyrev, Mikhail M. Bubnov, E. M. Dianov, A. S. Kurkov, Pavel V. Mamyshev, A. M. Prokhorov, Sergey D. Rumyantsev, V. A. Semenov, Sergey L. Semenov, Alexej A. Sysoliatin, Stanislav V. Chernikov, A. N. Gur'yanov, G. G. Devyatykh, and S. I. Miroshnichenko. A Single-Mode Fiber with Chromatic Dispersion Varying Along the Length. *IEEE J. Lightwave Technol.*, 9(5):561–6, May 1991.

[85] A. Mostofi, H.Hatami-Hanza, and P.L. Chu. Optimum Dispersion Profile for Compression of Fundamental Solitons in Dispersion Decreasing Fibers. *IEEE J. Quantum Electron.*, 33(4):620–8, Apr. 1997.

[86] Mark D. Pelusi and Hai-Feng Liu. Higher Order Soliton Pulse Compression in Dispersion-Decreasing Optical Fibers. *IEEE J. Quantum Electron.*, 33(8):1430–9, Aug. 1997.

[87] D. Huhse. *Neuartige Wellenlängenabstimmbare Halbleitersysteme mit Externen Glasfaserkavitäten.* PhD thesis, Technische Universität Berlin, 1999.

[88] Alexej Sysoliatin. Personal Communication, Fiber Optic Research Institute, Moscow, 2002.

[89] F.M. Mitschke and L.F. Mollenauer. Discovery of the soliton self-frequency shift. *Opt. Lett.*, 11(10):659–61, Oct. 1986.

[90] M. Nakazawa, K. Tamura, H. Kubota, and E. Yoshida. Coherence Degradation in the Process of Supercontinuum Generation in an Optical Fiber. *Optical Fiber Technology*, 4:215–23, 1998.

[91] K. R. Tamura and M. Nakazawa. Femtosecond Soliton Generation over a 32-nm Wavelength Range Using a Dispersion-Flattened Dispersion-Decreasing Fiber. *IEEE Phot. Techn. Lett.*, 11(3):319–21, 1999.

[92] Toshiaki Okuno, Masashi Onishi, Tomonori Kashiwada, Shinji Ishikawa, and Masayuki Nishimura. Silica-Based Functional Fibers with Enhanced Nonlinearity and Their Applications. *IEEE J. of Selected Topics in Q. Electr.*, 5(5):1385–91, 1999.

[93] Ayhan Demicran and Uwe Bandelow. Supercontinuum generation by modulation instability. *Optics Communications*, 244(1-6):181–5, Jan. 2004.

[94] F. Futami, Y. Takushima, and K. Kikuchi. Generation of 10 GHz, 200 fs fourier-transform-limited optical pulse train from modelocked semiconductor laser at 1.55 μm by pulse compression using dispersion-flattened fibre with normal group-velocity dispersion. *El. Lett.*, 34(22):2129–30, Oct. 1998.

[95] A. Demicran. Personal communication. WIAS Berlin, 2005.

[96] K. Tamura and M. Nakazawa. Timing Jitter of Solitons Compressed in Dispersion-Decreasing Fibers. *Opt. Lett.*, 23(17):1360–2, 1998.

[97] K. R. Tamura and M. Nakazawa. 54-fs, 10-GHz Soliton Generation from a Polarization-Maintaining Dispersion-Flattened Dispersion Decreasing Fiber Pulse Compressor. *Opt. Lett.*, 26(11):762–4, June 2001.

[98] K.-I. Hagiuda, T. Hirooka, S. Ono, M. Yoshida, M. Nakazawa, S. Arahira, and Y. Ogawa. Generation of a 40-GHz, 100-fs pulse train from a modelocked laser diode using DDF soliton compression. In *Proc. Europ. Conf. Opt. Commun. (ECOC)*, pages 180–1, Stockholm, Sweden, 2004. paper Tu3.3.2.

[99] Duckey Lee, Na Young Kim, Kyoung Min Kim, Namkyoo Park, Seong Joon Ahn, and Hee-Gon Woo. Design Parameters of Dispersion Decreasing Fiber based OTDM source: Quasi-adiabatic Higher-order Soliton Compression from Sinusoidal Input Signal. In *Proc. Optical Fiber Commun. (OFC)*, pages 227–9, Vol II,, Baltimore, MD, USA, 2000. talk WM 6.

[100] Antonella Bogoni, Paolo Ghelfi, Mirco Scaffardi, Claudio Porzi, Filippo Ponzini, and Luca Potì. Full 160 Gbit/s Single-Channel OTDM System Experiment Including All-Optical Transmitter, 3R, and Receiver. In *Proc.*

Europ. Conf. Opt. Commun. (ECOC), Stockholm, Sweden, 2004. paper We 1.5.1.

[101] S. V. Chernikov, J. R. Taylor, and R. Kashyap. Experimental Demonstration of Step-Like Dispersion Profiling in Optical Fibre for Soliton Pulse Generation and Compression. *El. Lett.*, 30(5):433–5, 1994.

[102] Masahiro Tsuchiya, Koji Igarashi, Satoshi Saito, and Masato Kishi. Sub-100 fs Higher Order Soliton Compression in Dispersion-Flattened Fibers. *IEICE Trans. Electron.*, E85-C(1):141–9, 2002.

[103] A. Siahlo, A. T. Clausen, J. Seoane, L. K. Oxenlowe, K. S. Berg, P. Jeppesen, O. Brox, S. Bauer, J. Kreissl, and B. Sartorius. Pulse Compression of a 40 GHz DFB Based Optical Clock Recovery. In *Proc. Europ. Conf. Opt. Commun. (ECOC)*, pages 382–3, Stockholm, Sweden, 2004. paper We 2.5.4.

[104] H. Quast, D. Huhse, O. Reimann, D. Zimmermann, and D. Bimberg. Femtosecond Pulsecompression Using A Comb-Like Dispersion Profiled Fiber (CDPF). In *Proc. Europ. Conf. Opt. Commun. (ECOC)*, Rimini, Italy, 2003. paper Th 3.2.5.

[105] M. Tadakuma, O. Aso, and S. Namiki. A 104GHz 328fs soliton pulse train generation through a comb-like dispersion profiled fiber using short high nonlinearity dispersion fibers. In *Proc. Optical Fiber Commun. (OFC)*, pages 178–80, 2000. paper ThL3-1.

[106] N. J. Doran and D. Wood. Nonlinear-Optical Loop Mirror. *Opt. Lett.*, 13(1):56–8, Jan. 1988.

[107] Nan Chi, Lin Xu, Leif Oxenløwe, Torger Tokle, and Palle Jeppesen. 2r regenerator based on high non-linear dispersion-imbalanced loop mirror. *Optics Communications*, 206:295–300, 2002.

[108] Jian Wu, Yuhua Li, Caiyun Lou, and Yizhi Gao. Optimization of pulse compression with an unbalanced nonlinear loop mirror. *Optics Communications*, 180:43–7, 2000.

[109] M. D. Pelusi, Y. Matsui, and A. Suzuki. Pedestal Suppression from Compressed Femtosecond Pulses Using a Nonlinear Fiber Loop Mirror. *IEEE J. Quantum Electron.*, 35(6):867–74, June 1999.

[110] N. J. Doran, D. S. Forrester, and B. K. Nayar. Experimental Investigation Of All-Optical Switching In Fiber Loop Mirror Device. *El. Lett.*, 25(4):267–9, Febr. 1989.

[111] W.S. Wong, S. Namiki, M. Margalit, H.A. Haus, and E.P. Ippen. Self-switching of optical pulses in dispersions-imbalanced nonlinear loop mirrors. *Opt. Lett.*, 22(15):1150–1152, Aug 1997.

[112] I. Y. Krushchev, I. D. Phillips, A. D. Ellis, R.J. Manning, D. Nesset, D. G. Moodie, R. V. Penty, and I. H. White. OTDM applications of dispersion imbalanced fibre loop mirror. *El. Lett.*, 35(14):1183–5, July 1999.

[113] H.G. Weber in E. Voges and K. Petermann. *Optische Kommunikationstechnik*, chapter 16. Springer Verlag, Berlin, 2002.

[114] G. P. Agrawal. *Nonlinear Fiber Optics*. Academic Press, San Diego, USA, 3rd edition, 2000.

[115] K. R. Tamura and M. Nakazawa. Spectral-Smoothing and Pedestal Reduction of Wavelength Tunable Quasi-Adiabatically Compressed Femtosecond Solitons Using a Dispersion-Flattened Dispersion Imbalanced Loop Mirror. *IEEE Phot. Techn. Lett.*, 11(2):230–2, Febr. 1999.

[116] R. Ludwig, A. Sizmann, U. Feiste, C. Schubert, M. Kroh, C. M. Weinert, and Hans-Georg Weber. Experimental verification of noise squeezing by an optical intensity filter in high-speed transmission. In *Proc. Europ. Conf. Opt. Commun. (ECOC)*, Amsterdam, Netherlands, 2001.

[117] N. J. Smith and N. J. Doran. Picosecond soliton propagation using nonlinear optical loop mirrors as intensity filters. *El. Lett.*, 30(13):1084–5, June 1994.

[118] P. V. Mamyshev. All-Optical Data Regeneration Based On Self-Phase Modulation Effect. In *Proc. Europ. Conf. Opt. Commun. (ECOC)*, pages 475–6, Madrid, Spain, 1998.

[119] K. Taira and K. Kikuchi. Picosecond Pulse Generation with High Extinction Ration Employing Electroabsorption Modulator, Fibre Compressor, and Self-Phase-Modulation-Based Pulse Reshaper. *El. Lett.*, 40(1):15–6, 2004.

[120] S. Kawanishi, H. Takara, T. Morioka, O. Kamatani, K. Takiguchi, T. Kitoh, and M. Saruwatari. Single Channel 400Gbit/s Time-Division-Multiplexed Transmission of 0.98psPulses over 40km Employing Dispersion Slope Compensation. *El. Lett.*, 32(10):916–8, May 1996.

[121] Sebastian Ferber, Carsten Schmidt-Langhorst, Reinhold Ludwig, Cristof Boerner, Colja Schubert, Vincent Marembert, Marcel Kroh, and Hans-Georg Weber. 160 Gbit/s OTDM Lomg-Haul Transmission with Long-Term Stability Using RZ-DPSK Modulation Format. *IEICE Trans. Electron.*, E88-B(5):1947–53, May 2005.

[122] S. Ferber, R. Ludwig, C. Boerner, C. Schubert, C. Schmidt-Langhorst, M. Kroh, V. Marembert, and H.G. Weber. 160 Gbit/s DPSK Transmission over 320 km Fibre Link with High Long-Term Stability. *El. Lett.*, 41(4):200–2, 2005.

[123] C. Schubert, S. Ferber, M. Kroh, C. Schmidt-Langhorst, R. Ludwig, B. Hüttl, R. Kaiser, and H.G. Weber. 40 GHz Semiconductor Mode-Locked Laser Pulse Source for 160 Gbit/s RZ-DPSK Data Transmission. In *ECOC, Glasgow, U.K., Tu1.5.3*, Sept. 2005.

[124] H.G. Weber, S. Ferber, M. Kroh, C. Schmidt-Langhorst, R. Ludwig, V. Marembert, C. Boerner, F. Futami, S. Watanabe, and C. Schubert. Single Channel 1.28 Tbit/s and 2.56 Tbit/s DQPSK transmission. In *Proc. Europ. Conf. Opt. Commun. (ECOC)*, 2005. PD paper Th4.1.2.

[125] E. Hilliger, V. Marembert, S. Ferber, M. Kroh, J. Berger, H. G. Weber, and B. Schmauss. EAM with Improved Switching Performance by Self Cascading. In *OFC*, pages 268–9, Atlanta, USA, 2003. OSA. paper TuP2.

[126] T. Kato, Y. Suetsugu, M. Takagi, E. Sasaoka, and M. Nishimura. Measurement of the nonlinear refractive index in optical fiber by the cross-phase-modulation method with depolarized pump light. *Opt. Lett.*, 20(9):988–90, May 1995.

[127] A. Boskovic, S.V. Chernikov, J.R. Taylor, L. Gruner-Nielson, and O.A. Levring. Direct continous-wave measurement of n_2 in various types of telecommunication fiber at 1.55μm. *Opt. Lett.*, 21(24):1966–8, Dec. 1996.

[128] Harry J. R. Dutton. *Understanding Optical Commnications*. Prentice-Hall PTR, Inc., USA, 1998.

Appendix A

Additional Measurements

A.1 Timing jitter tolerance of a 160 Gbit/s OTDM transmission system

A critical issue for an OTDM transmission system is the sensitivity of the error free performance to the timing jitter of the incoming data signals. Requirements on the pulse sources have to be derived from the allowable tolerances. Therefore the impact of timing jitter on the demultiplexer and receiver performance was investigated. The experimental set-up is depicted in Fig. A.1.

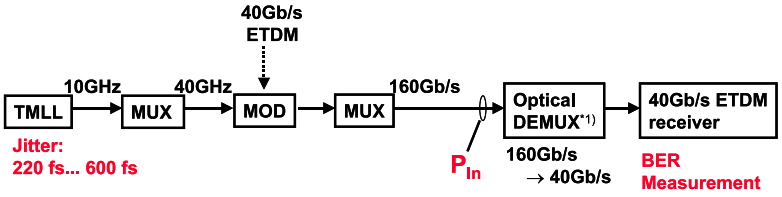

Figure A.1: Set-up of a 160 Gbit/s transmission system for measurement of the timing jitter tolerance.

The mode-locked laser was operated at 1555 nm. The timing jitter of the emitted 10 GHz pulse train was varied by changing the RF modulation power applied to the hybrid mode-locked laser and the adaptation of the gain current between 60.8 mA and 64.2 mA.

The influence of variations of other parameters was minimized due to a constant pulse width of 1.4 ps and a spectral width of 1.3 nm, which had been maintained for the different modulation powers. The amplitude noise was measured using a sampling oscilloscope and had a value between 1.5 % and 2 %. It did not change with the timing jitter. Note that the timing jitter measured with an oscilloscope were some 40 % to 20 % higher mainly due to the noise of the precision time base unit of 180 fs but to a minor extent also due to the limited frequency integration range of the SSB phase noise measurement.

In Fig. A.2 (a) the maximal tolerable value for the timing jitter can be

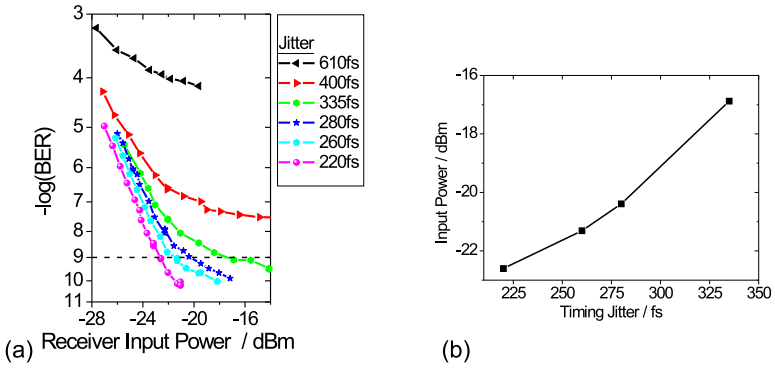

Figure A.2: (a): shows the BER curves for different timing jitter values. The jitter was calculated with the SSB phase noise measurement in the integration range between 100 Hz to 10 MHz. (b): the required receiver input power for error free detection ($BER < 10^{-9}$) versus the timing jitter of the 160 Gbit/s pulse train is shown.

determined to around 330 fs where the BER curve reached an error floor near a BER of $1 \cdot 10^{-9}$. The required receiver input power for error free reception of the data signal is shown in dependence of the timing jitter in Fig. A.2 (b). The main influence on the jitter sensitivity of this set-up is caused by the width of switching window of the demux. The exact limit for a data transmission system will strongly depend on the particular demultiplexer set-up being used. Here a demultiplexer with a self-cascaded EAM was used (cf. Ref. [125]) which provides a switching window of about 2.5 ps. However, as conclusion there is a requirement for the maximum tolerable jitter of a pulse source of about 260 fs for an error free operation of 160 Gbit/s systems. In approximation a timing jitter less than 65 fs is considered necessary for the operation of a 640 Gbit/s system.

A.2 Phase noise reduction

The main possibilities to reach a EC-MLL pulse generation with a low phase noise was already discussed in Sec. 5.4. Apart from a suitable choice of the parameters of the semiconductor laser material and the laser cavity set-up, the choice of optimum laser operation conditions also the 3^{rd} approach, the noise reduction by subsequent phase stabilization was investigated.

In the following the stabilization of the pulse generation is investigated by the set-up of a feed back circuit.

A.2.1 Feed back loops for the phase noise reduction

The deviation of the exact pulse positions can be corrected by a feed back signal which is evaluated to adjust the laser cavity length. The cavity length can be

changed by the alteration of the resonator mirror position as used for solid state MLL shown in Sec. 3.2. Alternatively the optical path length can be altered by a refractive index change. This is especially attractive for semiconductor devices due to the high dependence of the refractive index from the carrier density. It offers the possibility to avoid mechanical changes with their long time constants.

In the frame of this work a feed back loop as shown in the set-up in Fig. A.3 (a) was used for the reduction of phase noise during pulse generation. The pulse source comprised an ion implanted bulk-laser diode as described in Chap. 4 and 5. The EC-MLL generated a 10 GHz pulse train. A lower share of the pulse power was used to provide a feed back signal onto the gain current. A photodiode converted the generated pulse train into a RF feed back signal. A 1/8 frequency divider was needed to enable the phase comparison with a reference signal of an RF synthesizer in a phase comparator (PDF) element. The product signal was filtered by a low pass filter and added to the DC supply current for the gain section.
Due to the influence of the carrier density on the refractive index but also due to thermal heating the pulse round trip time and therefore the pulse spacing of the generated pulse train can be changed. The feedback ratio of the PLL signal had to be optimized.

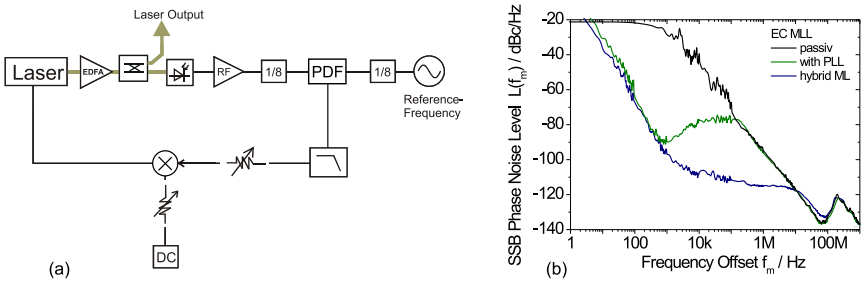

Figure A.3: PLL for an EC-MLL stabilization and its impact on the SSB noise performance

Fig. A.3 (b) shows the SSB Phase Noise curve of the passive mode-locked laser with the typical high phase noise levels (black curve) for the semiconductor laser. The improvements by insertion of the feed back loop is shown with the green curve. In comparison the phase noise curve for the hybrid mode-locked laser without feed back loop is shown with the blue curve. The circuit for phase stabilization did not reach an improvement in comparison with the solely hybrid mode-locked noise performance. A change of the gain current, e.g. an increase of the gain current, has an influence on the thermal heating of the laser diode and on the carrier density. A fundamental problem is the opposite influence of the thermal heating and the carrier density on the refractive index of the laser material. The thermal effects can be used to control rather slow frequency variations. The variation of the refractive index by electric effects

can control higher frequency variations. However, the contrary effects of a gain current change onto the refractive index remain a problem for an adjustment. An alternative is therefore the manipulation of other laser cavity length parameter like the mirror position or, if multi sectional laser diodes are used, the change of passive sections for phase tuning or wavelength tuning.
A more fundamental limitation of all phase locked loops is the loop length, a critical parameter for the maximum possible operation frequency. Limitations are imposed by the device capacities and the maximum frequency of the band-pass/feed back electronic. In this measurement a maximum bandwidth in the order of 100 kHz was available (Fig. A.3 (b)). However for an improvement of the noise performance of the semiconductor mode-locked laser the reduction of the phase noise in the frequency regions above 1 MHz is more important, since low frequency changes can be tracked by clock recovery set-ups. The latter are obligatory in network applications anyway.
N.B.: There is an obvious amplitude noise peak in the range of 200 MHz. The measured phase noise curves in Fig. A.3 (b) are taken for the upper side band. Measurements of the lower side band phase noise curve delivered identical values with exception of such a peak.

A.3 Multiplexing of short pulses

Pulse sources and modulator typically are operated at repetition frequencies of 10 or 40 GHz. Therefore the generation of a 640 Gbit/s data signal requires a multiplexing of the generated data sequences.

In multiplexing of pulses it has to be distinguished between multipexing of PRBS data signals and multiplexing of an unmodulated pulse train. The appropriate multiplexer devices differ in their fiber delay length and are called PRBS-multiplexer and pulse multiplier, respectively.

In laboratory experiments the generation of high data rates would require one transmitter per channel. In order to reduce the equipment needed, the data rate of one channel is increased in a subsequent multiplexer. A fiber based PRBS-multiplexer is depicted in Fig. A.4. In the example it comprises two stages for multiplexing, e.g. from 10 Gbit/s to 40 Gbit/s.

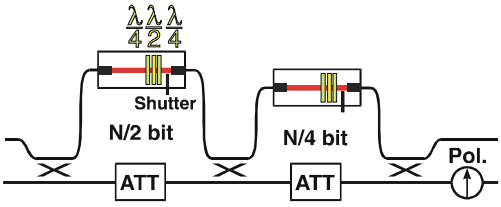

Figure A.4: Set-up of a fibre based multiplier with two stages containing a free space delay line including quarter- and half- wave plates.

The incoming 10 Gbit/s pulse train is split in the first multiplexer stage by a 3 dB coupler into two branches. Both branches of the multiplexer stage have

different lengths in order to obtain a delay between both pulse trains before they are recombined by the next 3 dB coupler. A free space optical delay line with quarter- and half-wave plates is introduced in one branch for the adjustment of the delay and of the polarization. To compensate for the higher loss of the optical delay line a variable attenuator is introduced in the other fiber branch to equalize the pulse power of the merged pulse trains. For doubling the bit rate of a PRBS word of the length of N Bit in a single stage the delay between both pulse trains has to be N/2 times the bit period of the incoming data signal in order to maintain the PRBS structure of the data word at the multiplied data rate. The data rate can be increased by further multiplexer stages.

For short pulses with a broad spectral width the tolerances of the multiplexer are more stringent. A disturbing influence of the dispersion of the first multiplexer stages is recognized on the pulse width when multiplexing with a 2^7-1 PRBS multiplexer from 10 Gbit/s to 40 Gbit/s and above. The first stages have a relatively long SSMF fibre delay exceeding 1 m and cause a broadening of the delayed pulses as shown in tab. A.1 for a 0.4 ps pulse with a gaussian shape. The multiplexing to higher bit rates is less critical due to shorter delay lengths needed. The maximum delay difference for the multiplexing is 2.56 m (limit of the arithmetic progression) and would lead to a pulse broadening of gaussian pulses from 0.40 ps to 0.58 ps. In case of multiplexing from 20 to 40 Gbit/s is has to be distinguished between pulses which have already experienced a delay in the 10 to 20 Gbit/s stage or not. As every pulse experienced a different dispersion, the resulting pulse train consists of pulses of different width which is not suitable for an application.

To avoid these problems, it is sufficient to operate with a base rate of 40 Gbit/s. For pulse multiplying from 10 GHz to 40 GHz a multiplexer, also called pulse multiplier, with just 1/2 bit delay can be used in order to circumvent these problems. Alternatively PRBS multiplexer with DSF fiber delays could be used.

MUX stage / GHz	delay /bit	delay /m	delay /ps	width
10-20 Gbit/s	$(2^7-1)/2$	1.28	3189.90	0.45
20-40 Gbit/s	$(2^7-1)/4$	0.64	1594.95	0.41
		1.92	4784.85	0.51

Table A.1: 2^7-1 PRBS multiplexer delay line fiber lengths, delay time and the broadening of a 0.4 ps gauss pulse due to the dispersion of SSMF.

Fig. A.5 shows the autocorrelation trace of a 160 Gbit/s signal consisting of short pulses. The 10 GHz pulse train was multiplied to 40 GHz, modulated with a 40 Gbit/s data signal and multiplexed to 160 Gbit/s. Note that an ideal autocorrelation trace of a data sequence with equal number of marks and spaces in the average has a central pulse and side pulses of half hight. Side pulses are result of a crosscorrelation. Deviations from the exact delay, power splitting and the remaining dispersion contribute to a pulse trace with different hight of each pulse. Due to the cross-correlation in combination with the timing jitter the measured side-pulses show an additional broadening and thus a minor increase

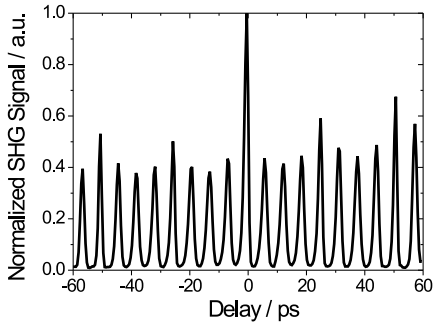

Figure A.5: Autocorrelation trace of a 0.4 ps 160 Gbit/s pulse train multiplexed with a 1/2 bit delay multiplexer from 10 to 40 GHz, subsequently modulated with a $2^7 - 1$ PRBS word and multiplexed to 160 Gbit/s maintaining the PRBS sequence. Slight deviations from the optimum multiplexer lead to the observed sub-structure of the measured pulse train.

in pulse width is inevitable in the cross correlation of pulses (cf. Section 2.3.2).

A.4 DPSK Transmission Experiment at 160 Gbit/s

The EC-MLL and the M-MLL pulse sources were tested in 160 Gbit/s DPSK transmission experiments [122, 123]. The setup for a measurement with the M-MLL is shown in Fig. A.6 and differs from the experiment in sec. 8.3. For data rates of 160 Gbit/s it is still possible to use uncompressed pulses and the demuliplexer can be implemented using the switching window of an EAM.

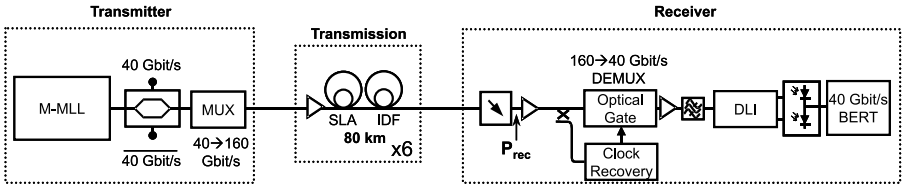

Figure A.6: Set-up for the 160 Gbit/s DPSK transmission experiment using the 40 GHz M-MLL pulse source in a 160 Gbit/s RZ-DPSK Transmitter. The transmission link was built by 6 spans of SLA-IDF.

In this example the 160 Gbit/s DPSK transmitter comprised the 40 GHz M-MLL pulse source. It was operated with a gain current of 102 mA and an absorber voltage of 1.7 V. The generated pulses had a sech^2 pulse shape and a pulse width of 1.4 ps. An 40 GHz RF signal was applied onto the absorber voltage for hybrid mode-locking. The generated 40 GHz pulse train had a timing jitter of $\sigma_{rms} = 85\ fs$ (evaluation range $f_m \in$ [100 Hz,10 MHz]). The

pulse sequence was modulated in a $LiNbO_3$ Mach-Zehnder phase modulator and followed by a passive fiber delay-line multiplexer to generate a single polarization 160 Gbit/s data signal. The transmission link had a length of 480 km (6 spans of SLA-IDF). The 160 Gbit/s DPSK receiver consisted of a 160 Gbit/s to 40 Gbit/s optical demultiplexer (DEMUX), an clock recovery and a 40 Gbit/s DPSK receiver. In the 40 Gbit/s DPSK receiver an optical pre-amplification was necessary and is followed by an optical bandpass filter. A fibre based delay-line interferometer (DLI) was used to convert the DPSK modulation into OOK modulation which is then detected by a balanced photoreceiver and a 40 Gbit/s BER detector (BERT).

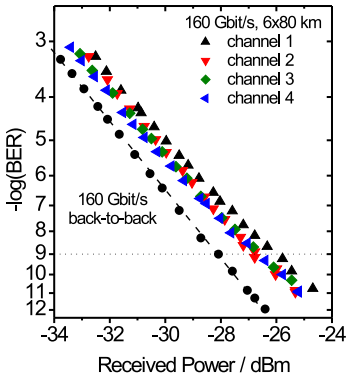

Figure A.7: BER measurement for the transmission of the 160 Gbit/s DPSK pulse train over 480 km SLA-IDF

The bit-error rate of the 160 Gbit/s RZ-DPSK data signal was measured after transmission over the 480 km fiber link and are shown in Fig. A.7. A 160 Gbit/s back-to-back measurement is included for comparison. Error-free performance was shown for all four 40 Gbit/s OTDM channels in the back-to-back measurement and after the 480 km transmission. The power penalties for the transmission varied between 1.2 and 2.1 dB compared to back-to-back BER curve.

Appendix B

Fiber Properties, Conversion of Parameter

B.1 Overview over fiber properties

Fiber Dispersion

Parallel to the dispersion D [ps/nm/km] often the second order dispersion coefficient β_2 [ps^2/km] is considered:

$$\beta_2 = -\frac{\lambda^2}{2\pi c} \cdot D \tag{B.1}$$

The dispersion slope S [ps/nm^2/km] can simultaneously be expressed by the third order dispersion coefficient β_3 [ps^3/km]

$$\beta_3 = (\frac{\lambda^2}{2\pi c})^2 \cdot (S - \frac{4\pi c}{\lambda^3}\beta_2) \tag{B.2}$$

Only for transmission of sub-picosecond pulses higher order dispersion such as β_4 has to be included in compensation schemes.

Fiber Nonlinearity

A high nonlinearity is attractive for an efficient pulse broadening. The measurement of the nonlinear coefficient is based on SPM, XPM and FWM processes in the investigated fibers. In the literature details of the measurement methods can be found [126, 127]. The accuracy (heights) of the measured coefficient varies depending on the measurement method being used. For the HNLF the reported values vary between 11 and 21 km^{-1} W^{-1}. For applications a γ value of about 10 W^{-1} km^{-1} is proposed as an optimum balance between a high nonlinear coefficient and the increasing fiber loss of bulk fiber.

B.1.1 Properties of the dispersion decreasing fiber

Table B.1 gives an overview over the DDF fiber parameter used in the frame of this work.

Fiber	DDF	DF-DDF	HNL-DDF
length / m	1000	1000	920
Attenuation / dB	1.8	1.6	3.2
Dispersion begin / ps/nm/km	10.0	10.0	12.0
Dispersion end / ps/nm/km	0.5	-1.0	0.5
Nonlinearity γ / W^{-1} km^{-1}	3	3	9

Table B.1: Overview over DDF fiber properties.

B.1.2 Properties of the highly nonlinear fiber

Fiber	HNLF 1	HNLF 2	HNLF 3/ 4/ 5/ 6
length / m	510	789	125/ 250/ 500/ 750
Attenuation / dB km^{-1}	0.47	0.84	0.78
λ_0 / nm	1569	1555	non
D at 1550 nm / ps nm^{-1} km^{-1}	N.A.	-0.09	-0.49/ -0.49/ -0.45/ -0.34
S at 1550 nm / ps/nm^2/km	0.03	0.019	0.0061/ 61/ 62/ 64
γ / W^{-1} km^{-1}	21	10.5	10.5
PMD / ps $(\sqrt{km})^{-1}$	N.A.	0.053	0.024

Table B.2: Overview over HNLF fiber properties

The properties of HNL fibers are listed in Table B.2. λ_0 is the zero dispersion wavelength of the HNL fiber. Some fibers (HNLF3-6) have a normal dispersion over the full wavelength range.

B.1.3 Properties of the transmission fiber

For the transmission experiment shown in Sec. 8.2 a SLA-IDF dispersion managed fiber combination was used.

The SLA-IDF fibre (ultra-wave fibre) was provided by OFS-Denmark. Each 80 km fibre span consisted of Super Large Area Fibre SLA ($A_{eff} = 105\ \mu m^2$, D = 20 ps/km/nm) and Inverse Dispersion Fibre IDF ($A_{eff} = 33\ \mu m^2$, D = $-$ 44 ps/km/nm).

B.2 Conversion Charts, Conversion of Parameter

Fourier transformation of Pulse shapes

Gaussian pulse shape:

$$f(x) = Aexp(-a^2x^2) \Leftrightarrow f(y) = \frac{A\sqrt{(\pi)}}{a} exp\frac{-y^2}{4a^2} \tag{B.3}$$

Sech pulse shape:

$$f(x) = sech(ax) \Leftrightarrow f(y) = \frac{1}{2} \cdot \pi a^{-1} sech(\frac{1}{2}\pi\frac{y}{a}) \tag{B.4}$$

Conversion of Parameter

The spectral width can be measured on the frequency or wavelength scale. For comparison often used values are given Tab. B.3.

λ / nm	1310	1530	1550	1565
ν / THz	228.85	195.94	193.41	191.56

$\Delta\lambda$ / nm at 193 THz	1	1.6	8.02	200
$\Delta\nu$ / THz at 1550 nm	0.125	0.2	1	25.06

Table B.3: Conversion THz $\leftrightarrow$ nm

The (absolute) electrical peak to peak voltage at 50 Ω is converted into power in dBm according to

$$U_{PP} = 20 \cdot \sqrt{10^{\frac{P_{dBm}}{10}}/1000} \tag{B.5}$$

With $P_{opt} = \frac{1}{2}|E_{el}|^2$ the conversion between dBm and mW of optical power follows to

$$P_{opt}[dBm] = 10\ log_{10}\frac{P_{mW}}{1mW} \tag{B.6}$$

Conversion Charts

Time-Bandwidth Ratio for Transform Limited Pulses

The spectral width of a transformation limited pulse of a pulse width of 0.4 ps depends on the exact pulse shape (gaussian or sech^2) and varies between 6 nm and 9 nm (Fig. B.1).

The calculation of the spectral width and temporal width of a transformation limited pulse was according to

$$K = \frac{\Delta\tau \cdot \Delta\lambda}{\lambda^2} \cdot c_0 \tag{B.7}$$

with K: Time-Bandwidth-Product (cf. Tab. 2.2).

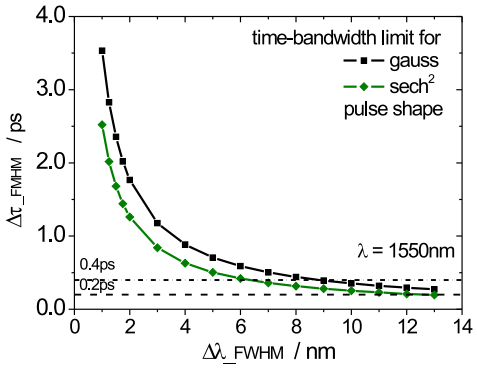

Figure B.1: Time-Bandwidth Ratio for Transform Limited sech^2 and gauss pulses

Pulse Peak Power versus Average Power

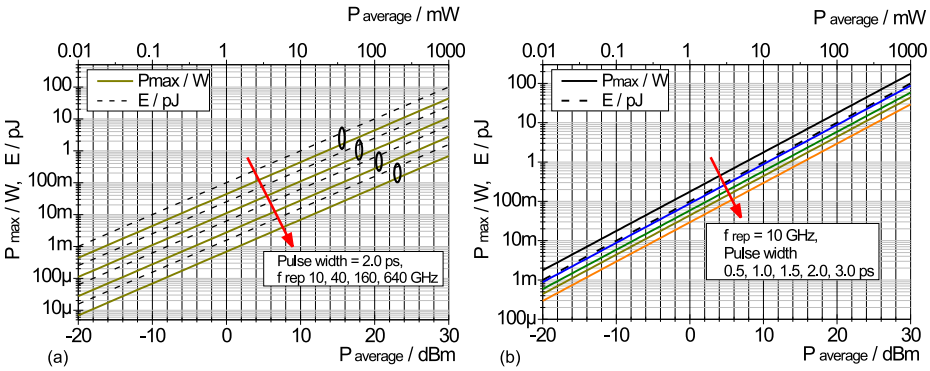

Figure B.2: Conversion chart between P_0/W, E_{pulse}/pJ and P_{avg}. Diagram (a): for 2.0 ps sech^2 pulses at repetition frequencies of 10, 40, 160 and 640 GHz. Diagram (b): for 0.5, 1.5, 2.0 and 3.0 ps sech^2 pulses at a repetition frequency of 10 GHz.

For conversion between pulse peak power, peak energy and average power Fig. B.2 (a) shows the conversion charts for 2.0 ps sech^2 pulse train with repetition frequencies of 10, 40, 160 and 640 GHz and in Fig. B.2 (b) for different pulse width of 0.5, 1.0, 1.5, 2.0 and 3.0 ps for a repetition frequency of 10 GHz.

The conversion is according to

$$P_{max}(mW) = 1.763 \cdot \frac{T_{Bit}}{(2 \cdot T_{FWHM})} \cdot 10^{(P_{avg}(dBm)/10)} \quad \text{(B.8)}$$

$$E_{pulse}(fJ) = T_{Bit} \cdot 10^{(P_{avg}(dBm)/10)} \quad \text{(B.9)}$$

with T_{Bit} the Bit-period in ps and T_{FWHM} the FWHM pulse width in ps.

N=1 Soliton Peak Power and Average Power

In Fig. B.3 for a 10 GHz pulse train is shown in dependence of the soliton pulse width for propagation in SSMF (a) and in dependence of the fiber dispersion for 0.4 ps and 2.0 ps soliton pulse widths (b).

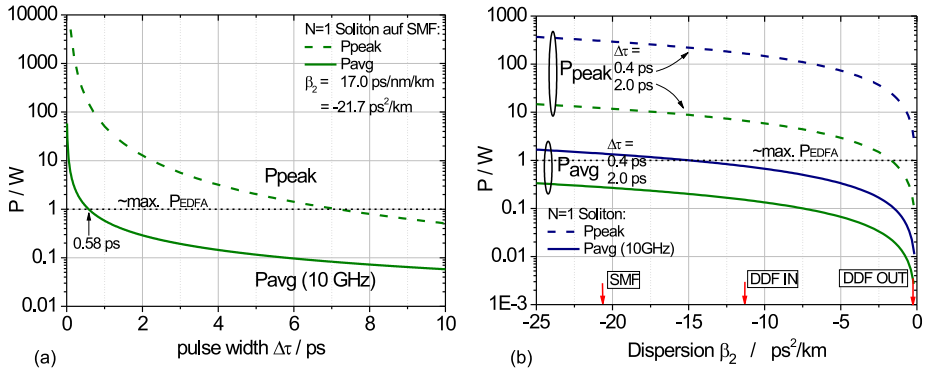

Figure B.3: (a) Pulse peak power P_{peak} and (b) Average power P_{avg} for a 10 GHz pulse train of fundamentals soliton (N=1).

The soliton peak power is inverse proportional to $1/T_{FWHM}^2$ and direct proportional to β_2:

$$P_0 = \frac{|\beta_2|}{\gamma \cdot T_0^2} \tag{B.10}$$

The relation between the pulse peak power P_0 and the average power of a pulse trains is

$$P_{avg} = \frac{2 \cdot T_0 P_0}{T_{Bit}} \tag{B.11}$$

with the bit period T_{Bit} in [ps] and the integration over a soliton pulse

$$\int_{-\infty}^{\infty} sech(\frac{t}{T_0})^2 \, dt \;=\; 2\, T_0 \tag{B.12}$$

cf. factor 2 in eqn. 6.2.

EDFA gain spectrum

A typical EDFA gain spectrum in shown in Fig. B.4. Gain flattened EDFAs use absorption plates to attenuate the gain maxima to an average value.

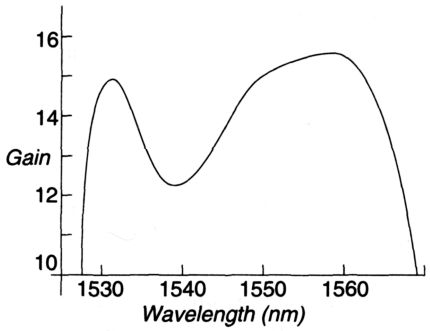

Figure B.4: Gain spectrum of an EDFA [128].

Appendix C

List of Variables and Abbreviations

name	described quantity
$\hat{A}$, $\hat{a}$	Amplitude
A	Absorption [-]
a_n	amplitude of the n^{th} cosine term of a Fourier expansion
B	Bit rate [Hz]
1/B	Bit period [s, typ. ps]
C-Band	Wavelength Band 1530-1565nm
C(τ)	Chirp [GHz]
c_0	light velocity in vacuum [$2.99792458 \cdot 10^8$ m/s]
D	Dispersion [ps/nm/km]
d	height of the active region of a semiconductor diode [nm]
E_0	amplitude of the superposition of optical modes [V/m]
E_{el}, E(t)	electrical field [V/m]
E_n	amplitude of the mode n [V/m]
E_{Pulse}	energy of a single pulse [J]
f_0	reference frequency [Hz]
f_m	frequency offset from center frequency in SSB [Hz]
f_{noise}	frequency of noise components [Hz]
f_{rep}	pulse repetition frequency [Hz]
f_{sync}	synchronization frequency [Hz]
$f_{0passiveML}$	frequency of the free running mode-locked laser [Hz]
Δf	frequency variation [Hz]
G(τ)	convoluted pulse shape [ps]
i	index [-]
I	pulse intensity [W]
I_{SHG}	SHG Intensity [a.u.]
I_{gain}	gain current [mA]
$I_{s\ abs}$, $I_{s\ gain}$	Saturation intensity of absorber and gain section
K	time- bandwidth- product [-]

name	described quantity
$L(f_m)$	Side Band Phase Noise Level L [dBc/Hz]
L_{LDF}	length of LDF [m]
L-I- curve	power- current curve
L_D	Dispersion Length [m]
L-Band	Wavelength Band 1565 - 1625 nm
l	length [m]
N	Number of Bits [-]
n	index variable [-]
n, n_0, n_{sc}	refractive index in general, -of air and -semiconductors [-]
P	power [dBm, W]
P_0, P_{Peak}	pulse peak power [dBm, W]
P_{avg}	average power [dBm, W]
P_{opt}, P_{el}	optical / electrical power [dBm, W]
P_{in}, P_{out}	input-, output power [dBm, W]
P_{trans}	transmitted power [dBm, W]
P_λ	spectral power at λ [dBm, W]
$P_{SSB}(f_m)\|_{Hz}$	SSB Power at offset f_m [dBc/Hz]
R	Reflectivity [-]
S	Dispersion Slope [ps/nm^2/km]
S_{11}	input reflection
T	Transmission [-]
T_{Bit}	Time interval of one bit slot [s, typ. ps]
T_{FWHM}	temporal full width half maximum [ps]
T_0	temporal pulse width, $T_0 = T_{FWHM}/1.763$ [ps]
$T_N(t)$	temporal width transmission window of the EAM [ps]
t	time [s]
t_{group}	group delay [ps]
U_{PP}	peak-to-peak voltage [V]
U_{abs}	voltage biased to the saturable absorber [V]
$V_{amplitude}$	voltage from peak to zero [V]
v_{gr}	group velocity [m/s]
w	width of the waveguide of a semiconductor diode [μm]
z	parameter for length [m]
Δt	temporal pulse width = T_{FWHM} [ps]
Δt_{ac}	temporal width of an autocorrelation function [ps]
$\beta_2, \beta_3, \beta_4$	2nd, 3rd and 4th order of dispersion [ps^2/km, ps^3/km]
γ	nonlinear coefficient [W^{-1}km^{-1}]
λ	wavelength [nm]
λ_0	zero dispersion wavelength [nm]
λ_g	wavelength of the gain maximum [nm]
$\nu_{carrier}$	carrier frequency [Hz]
$\Delta t \cdot \Delta\nu$	time-bandwidth product K [-]
$\Delta\nu$, $\Delta\lambda$	spectral pulse width [Hz, nm]
$\Delta\nu_{n,n+1}$	spectral distance between optical modes n and n+1 [Hz]

name	described quantity
ξ	phase angle [°, rad]
σ_{rms}	standard deviation
σ_{pc}, σ_{pp}	standard deviation peak to clock, -peak to peak [ps, fs]
τ	time [s, ps]; often used for a variable delay time etc.
τ_a, τ_n	recovery time of the absorber and gain medium, respectively [ps]
τ_c	cavity round trip time [ps]
t_{AC}, t_{XC}	pulse width in autocorrelation, - cross-correlation [ps]
$\phi(\tau)$	temporal phase information [°, rad]
$\Delta\phi$	phase shift [°, rad]
ϕ_{cw}, ϕ_{ccw}	phase shift - clock wise, - counter clock wise [°, rad]
$\phi_{SMF}, \phi_{LDF}, \phi_{NL\ LDF}$	phase shift in SSMF, LDF, NL LDF [°, rad]
$\varphi(\lambda)$	spectral phase [°, rad]

Abbreviation	full name
AN	Amplitude Noise
ACF	Auto-Correlation Function
AK	Auto-Correlator
AR	Anti Reflection
BER	Bit Error Ratio
BERT	Bit Error Ratio Test bed
CDPF	Comb like Dispersion Profiled Fiber
CW	Continuous Wave
DBR	Distributed Bragg Reflector
DDF	Dispersion Decreased Fiber
DEMUX	De-Multiplexer
DF-DDF	Dispersion Flattened - DDF
DFF	Dispersion Flattened Fiber
DGD	Differential Group Delay [ps]
DILM	Dispersion Imbalanced Loop Mirror
DPSK	Differential Phase Shift Keying
DSCF	Dispersion Slope Compensated Fiber
DSF	Dispersion Shifted Fiber
EAM	Electro Absorption Modulator
EC-MLL	External Cavity - Mode-Locked Laser
EDFA	Erbium Doped Fiber Amplifier
EDRL	Erbium Doped Fiber Ring Laser
ETDM	Electrical Time Division Multiplexing
FEC	Forward Error Correction
FROG	Frequency Resolved Optical Gating
FWHM	Full Width Half Maximum

Abbreviation	full name
FWM	Four Wave Mixing
GRIN	Gradient Index
HDF	High Dispersion Fiber
HL	Combination of high reflectivity layer and low reflectivity layer
HNL-DDF	High Non-Linear DDF
HNLF	High Non-Linear Fiber
HP-EDFA	High Power EDFA, $P_{out\ avg} > 20$ dBm
HR	High Reflectivity
InGaAsP	Semiconductor comprising the elements Indium Gallium Arsenide Phosphide
IDF	Inverse Dispersion Fiber, also: RDF - reverse dispersion fiber
ITU	International Telecommunication Union
LDF	Low Dispersion Fiber
MBE	Molecular Beam Epitaxy
MOCVD	Metal Organic Chemical Vapor Deposition
MOD	Modulator
M-MLL	Monolithic - Mode-Locked Laser
MQW	Multi Quantum Well
MUX	Multiplexer
NA	Numerical Aperture
NOLM	Nonlinear Optical Loop Mirror
NRZ	Non-Return-to-Zero
OOK	On-Off-Keying
OTDM	Optical Time Division Multiplexing
PM	Polarization Maintaining
PMD	Polarization Mode Dispersion
PN	Phase Noise
PRBS	Pseudo Random Bit Sequence
RDF	Reverse Dispersion Fiber
RF	Radio Frequency
RIN	Relative Intensity Noise
RZ	Return-to-Zero
SA	Saturable Absorber
SBS	Stimulated Brillouin Scattering
SDH	Synchronous Digital Hierarchy
SDPF	Step like Dispersion Profiled Fiber
SESAM	Semiconductor Saturable Absorber Mirror
SHG	Second Harmonic Generation
SLA	Super Large Area
(S)SMF	(Standard) Single Mode Fiber
SNR	Signal to Noise Ratio
SPM	Self Phase Modulation
SSB	Single Side Band
STM	Standard Transmission Module

Abbreviation	full name
TDM	Time Division Multiplexing
TEM_{00}	Transversal Electro Magnetic wave with gaussian intensity distribution
TPS	Trailing Pulse Suppression
VCO	Voltage Controlled Oscillator
(D)WDM	(Dense) Wavelength Division Multiplexing
XPM	Cross Phase Modulation

Appendix D

List of Publications

- M. Kroh, C. Schmidt, R. Ludwig, C. Schubert, and Hans-Georg Weber. Investigations on Phase Noise in a Semiconductor Mode-Locked Laser. In *Proc. Optical Fiber Commun. (OFC)*, pages 673–4, Washington, DC, USA, March 2003, paper FF 5.

- M. Kroh, C.M. Weinert, C. Schmidt-Langhorst, C. Schubert, J. Berger, C. Boerner, R. Ludwig, and H.G. Weber. Semiconductor Mode-Locked Laser Pulse Source for 320 and 640 Gb/s RZ Data Transmitter. In *Proc. Europ. Conf. Opt. Commun. (ECOC)*, pages 442–3, Stockholm, Sweden, 2004, paper We 3.5.7.

- M. Kroh, B. Hüttl, S. Ferber, and H. G. Weber. Low noise 400 fs pulse generation by monolithic semiconductor mode-locked laser and soliton pulse compression. In *CLEO Europe*, Munich, Germany, 2005, paper CB8-2-THU.

- M. Kroh, S. Ferber, C. Schmidt-Langhorst, V. Marembert AndC. Schubert, R. Ludwig, and Hans-Georg Weber. Transmitter enabling ultra-high speed transmission of phase modulated data signals up to 640 Gbit/s. In *Proc. Optical Fiber Commun. (OFC)*, Anaheim, CA (USA), Mar. 2006, Invited Paper OWW1.

- S. Diez, E. Hilliger, M. Kroh, C. Schmidt, C. Schubert, H. G. Weber, L. Occhi, L. Schares, G. Guekos, and L. K. Oxenloewe. Optimization of SOA-Based Sagnac-Interferometer Switches for Demultiplexing to 10 and 40 Gb/s. *Opt. Commun.*, 189:241–249, March 2001.

- R. Ludwig, A. Sizmann, U. Feiste, C. Schubert, M. Kroh, C. M. Weinert, and H. G. Weber. Experimental Verification of Noise Squeezing by an Optical Intensity Filter in High-Speed Transmission. In *Proc. Europ. Conf. Opt. Commun. (ECOC)*, pages 178–9, Amsterdam, Netherlands, 2001.

- C.M. Weinert, J. Berger, U. Feiste, E. Hilliger, B. Konrad, M. Kroh, R. Ludwig, K. Petermann, C. Schmidt, C. Schubert, H.G. Weber, and

T. Yamamoto. High bit rate OTDM-transmission on standard fibre. *Int. J. Electron. Commun. (AEÜ)*, 55(5):349–353, 2001.

- K. Yvind, P.M.W. Skovgaard, J. Moerk, J. Hanberg, and M. Kroh. Performance of External Cavity Mode-Locked Semiconductor Lasers Employing Reverse Biased Saturable Absorbers. *Physica Scripta*, T101:129–32, 2002.

- R. Kaiser, B. Hüttl, H. Heidrich, S. Fidorra, W. Rehbein, H. Stolpe, R. Stenzel, F. Boczainowski, G. Jacumeit, and M. Kroh. Tunable monolithic mode-locked lasers on GaInAsP/InP with 2 ps pulses and low timing jitter. In *Proc. Intern. Semicond. Laser Conference (ISLC)*, Grarmisch-Partenkirchen (D), 2002, PD paper 2.

- C. Schmidt, F. Futami, S. Watanabe, T. Yamamoto, C. Schubert, J. Berger, M. Kroh, H.-J. Ehrke, E. Dietrich, C. Börner, R. Ludwig, and H. G. Weber. Complete optical sampling system with broad gap-free spectral range for 160 gbit/s and 320 gbit/s and its application in a transmission system. In *Proc. Optical Fiber Commun. (OFC)*, Anaheim, USA, 2002, paper ThU1.

- C. Schmidt, C. Schubert, J. Berger, M. Kroh, H.-J. Ehrke, E. Dietrich, C. Börner, R. Luwig, H.G. Weber, F. Futami, S. Watanabe, and T. Yamamoto. Optical q-factor monitoring at 160 gb/s using an optical sampling system in an 80 km transmission experiment. In *OSA Trends in Optics and Photonics (TOPS) Vol. 73, Conference on Lasers and Electro-Optics, OSA Technical Digest, Postconference Edition*, pages 579–580, Washington DC, 2002. Optical Society of America.

- H. G. Weber, R. Ludwig, C. Schmidt, C. Schubert, J. Berger, E. Hilliger, M. Kroh, V. Marembert, C. Boerner, S. Ferber, and H.J. Ehrke. 160 Gbit/s TDM-transmission technology. In *Proc. Europ. Conf. Opt. Commun. (ECOC)*, 2002, invited paper 2.1.1.

- B. Huettl, R. Kaiser, M. Kroh, W. Rehbein, H. Stolpe, S. Fidorra, R. Stenzel, G. Jacumeit, and H. Heidrich. Noise Performance of Mode-locked 40 GHz Pulse Source Modules. In *Proc. Conf. Laser and Electro Optics Society LEOS*, Tucson, USA, 2003, Vol.1, paper ME2.

- E. Hilliger, V. Marembert, S. Ferber, M. Kroh, J. Berger, H. G. Weber, and B. Schmauss. EAM with Improved Switching Performance by Self Cascading. In *Proc. Optical Fiber Commun. (OFC)*, pages 268–9, Atlanta, USA, 2003, OSA, paper TuP2.

- B. Huettl, R. Kaiser, F. Boczainowski, S. Fidorra, H. Heidrich, G. Jacumeit, M. Kroh, W. Rehbein, R. Stenzel, and H. Stolpe. Monolithic mode-locked laser on GaInAsP/InP for 160 Gb/s TDM applications. In *Proc. Optical Fiber Commun. (OFC)*, Atlanta, USA, 2003, paper FF7.

- A. Beling, H.-G. Bach, G. G. Mekonnen, T. Eckhardt, R. Kunkel, G. Jacumeit, M. Kroh, and J. Berger. Fully Packaged InP-Based Photodetector for 80/85 GBit/s RZ Systems. In *Proc. Europ. Conf. Opt. Commun. (ECOC)*, Rimini, Italy, September 21-25 2003, PD-paper Th4.4.4.

- J. Mulet, J. Moerk, and M. Kroh. Identification of amplitude and timing jitter in external cavity mode-locked semiconductor lasers. In *Proc. Conf. Lasers and Electro Optics Society (CLEO)*, San Francisco, USA, 2004, paper CTuY7.

- V. Marembert, C. Schubert, S. Ferber, K. Schulze, C. Schmidt-Langhorst, C. Boerner, M. Kroh, R. Ludwig, S. Watanabe, F. Futami, R. Okabe, and Hans-Georg Weber. Single-channel 640 Gbit/s DPSK transmission over a 160 km fibre link. In *Proc. Europ. Conf. Opt. Commun. (ECOC)*, Stockholm, Sweden, Sept. 2004, PD Paper Th4.4.2.

- R. Ludwig, S. Ferber, C. Boerner, C. Schmidt-Langhorst, E. Hilliger, M. Kroh, V. Marembert, and Hans-Georg Weber. 160 Gbit/s DPSK-transmission - technologies and system impact. In *Proc. Europ. Conf. Opt. Commun. (ECOC)*, Stockholm (Sweden), Sept. 2004, Invited Paper Tu1.1.3.

- R. Ludwig, S. Ferber, C. Boerner, C. Schubert, C: Schmidt, J. Berger, M. Kroh, E. Hilliger, V. Marembert, and Hans-Georg Weber. 160 Gb/s DPSK transmission system with high long-term stability. In *9th Optoelectron. and Commun. Conf. (OECC/COIN 2004), Technical Digest*, pages 472–473, Yokohama, Japan, July 2004, Paper 14C4-2.

- Hans-Georg Weber, Sebastian Ferber, Marcel Kroh, Carsten Schmidt-Langhorst, Reinhold Ludwig, Vincent Marembert, Christof Boerner, Fumio Futami, Shigeki Watanabe, and Colja Schubert. Single channel 1.28 Tbit/s and 2.56 Tbit/s DQPSK transmission. In *Proc. Europ. Conf. Opt. Commun. (ECOC)*, Glasgow, Scotland (U.K.), Sept. 2005, Post-Deadline Paper Th4.1.2.

- C. Schubert, S. Ferber, M. Kroh, C. Schmidt-Langhorst, R. Ludwig, B. Hüttl, R. Kaiser, and H.G. Weber. 40 GHz Semiconductor Mode-Locked Laser Pulse Source for 160 Gbit/s RZ-DPSK Data Transmission. In *Proc. Europ. Conf. Opt. Commun. (ECOC)*, Glasgow, U.K., Sept. 2005, paper Tu1.5.3.

- J. Mulet, M. Kroh, and J. Moerk. Pulsewidth and noise properties of external-cavity mode-locked semiconductor lasers. In *Proc. Conf. Lasers and Electro Optics Society Europe (CLEO Europe)*, Munich, Germany, 2005, paper EA2-1-THU.

- B. Huettl, R. Kaiser, M. Kroh, C. Schubert, G. Jacumeit, and H. Heidrich. Optical 40 GHz pulse source module based on a monolithically integrated mode locked DBR laser. In *SPIE Asia Pacific Optical Communications*

Conf. (APOC), pages Inv. talk 12b, Vol. 6020, Shanghai, China, Nov. 2005.

- S. Ferber, R. Ludwig, C. Boerner, C. Schubert, C. Schmidt-Langhorst, M. Kroh, V. Marembert, and H.G. Weber. 160 Gb/s DPSK transmission over 320 km fibre link with high long-term stability. *El. Lett.*, 41(4):200–2, Feb. 2005.

- S. Ferber, C. Schmidt-Langhorst, R. Ludwig, C. Boerner, C. Schubert, V. Marembert, M. Kroh, and H.G. Weber. 160 Gbit/s OTDM long-haul transmission with long-term stability using RZ-DPSK modulation format. *IEICE Trans. Electron.*, E88-B(5):1947–54, May 2005.

- H.G. Weber, S. Ferber, Marcel Kroh, Carsten Schmidt-Langhorst, Reinhold Ludwig, Vincent Marembert, Christof Boerner, Fumio Futami, Shigeki Watanabe, and Colja Schubert. Single channel 1.28 Tbit/s and 2.56 Tbit/s DQPSK transmission. *El. Lett.*, 42(3):178–9, Feb. 2006.

- Josep Mulet, Marcel Kroh, and Jesper Moerk. Pulse properties of external-cavity mode-locked semiconductor lasers. *Optics Express*, 14(3):1119–24, Feb. 2006.

Appendix E

Acknowledgements

During my dissertation, I was fortunate to become acquainted with many people who contributed to the project of this thesis.

First of all I would like to thank Prof. Dr. Klaus Petermann from the Berlin University of Technology and Prof. Dr. Hans-Georg Weber from the Fraunhofer Institute for Telecommunications, Heinrich-Hertz-Institute, for giving me the opportunity and their support to work on the topic of this dissertation. Prof. Dr. Dr. Boche is acknowledged for his consent to chair the examination committee.

I would like to thank my former colleagues in the OTDM group at the Heinrich-Hertz-Institute Jörn Berger, Christoph Börner, Erik Dietrich, Hans Jürgen Ehrke, Uwe Feiste, Sebastian Ferber, Enno Hilliger, Herbert Knupke, Lothar Küller, Carsten Schmidt-Langhorst, Reinhold Ludwig, Vincent Marembert and Colja Schubert for providing an inspiring, and always friendly cooperation. I enjoyed the work with our students Sanjib-Kumar Brahma, Marcel Bielefeldt, Alex Gual i Coca, Robert Elschner, Dennis Plüschke, Andre Grede and Martin Schubert during my time at HHI.

An essential help for my work on laser devices was the fruitful collaboration with the project group of Helmut Heidrich. I gratefully acknowledge the friendly support by Sybille Fidorra, Helmut Heidrich, Bernd Hüettl, Ronald Kaiser, Wolfgang Rehbein, Ralf Stenzel, Heiko Stolpe and Ute Troppenz.

Carl Weinert is acknowledged for his numerical investigations of the behavior of nonlinear optical loop mirrors, which provided the basis for the layout of the pulse pedestal suppression investigated in the frame of this work.

I also would like to thank Gero Bramann, Margit Ferstl, Christian Fröhlich, Lutz Molle, Ludwig Mörl, Susanne Müller, Wolfgang Passenberg and all colleagues from the Heinrich-Hertz-Institute for their open-minded and friendly cooperation.

I thank Andreas Steffan, Oliver Schulz and Holger Quast for the discussions on pulse sources, laser diodes and on alternative pulse compression schemes.

It was a pleasure to me to share the experience to work and write for a dissertation with my fellow students from the institute of electrical engineering, RF electronics and photonics Christian Bunge, Johannes Fischer, Fabian Kerbstadt, Miroslawa Malach, Alessandro Melo, Torsten Mitze, Juraj Slovak,

Karsten Voigt, and Lars Zimmermann.

I would like to thank Svend Bischoff, Anders Clausen, Jesper Mørk, Josep Mulet, Leif Oxenløwe and Kresten Yvind for the motivating international co-operation between our research groups.

I grateful acknowledge the opportunity to collaborate with the industrial partners of Alcatel, especially with Eugen Lach, Michael Schmidt, Karsten Schuh, Esther Le Rouzic, Benjamin Cuenot and Christophe Kazmierski in the frame of the european project Toprate.

Special thanks are dedicated to the expert of phase noise, Leif Jiang, for the discussions on the timing stability of semiconductor laser.

I would like to thank my colleagues and experts for optical fibers Fumio Futami, Alexej Sysoliatin, Michael Schmidt and Paul Erik Schmidt for their expertise, literature suggestions and the indispensable support by providing optical fibers for the nonlinear pulse reshaping and for a precise dispersion control.

Last but not least I want to thank my parents, my fellow students from the physics department as well as my friends and my neighbors from the Siegmunds Hof residence, who gave me support and motivation during all the time of this work, partly by sharing the experiences from their own academic adventures.

The work and completion of this dissertation was made possible in the frame the projects "psOEIC" from the Federal Ministry of Research of Germany BMBF, "IST Toprate" from the European Union and "Terabit Optics Berlin" from the german federal state Berlin.